Nanostructured bioarchitectures for electrochemical and optical biosensor applications : design of a biocathode for biofuel cells

Meenakshi Singh

UNIVERSITÉ DE GRENOBLE

THÈSE

Pour obtenir le grade de

DOCTEUR DE L'UNIVERSITÉ DE GRENOBLE

Spécialité : **Matériaux, Mécanique, Génie Civil, Électrochimie**

Arrêté ministériel : 7 août 2006

Présentée par

Meenakshi SINGH

Thèse dirigée par **Dr. Serge COSNIER, Dr. Michael HOLZINGER** et codirigée par **Prof. MaryamTabrizian**

préparée au sein du **Laboratoire BiosystémesÉlectrochimiques et Analytiques du Département de Chimie Moléculaire** dans**l'ÉcoleDoctorale I-MEP2**

Nanostructured Bioarchitectures for Electrochemical and Optical Biosensor applications – Design of a Biocathode for Biofuel Cells.

Thèse soutenue publiquement le **30 octobre 2014**, devant le jury composé de :

Mme, Carole CHAIX-BAUVAIS
Directrice de Recherche, CNRS, Lyon, Président
Mr, Philippe POULIN
Directeur de Recherche, CNRS, Bordeaux, Rapporteur
Mr, Hubert PERROT
Directeur de Recherche, CNRS, Paris, Rapporteur
Mme, Maryam TABRIZIAN
Professeur, McGill University, Canada, Co-Directeur de thése
Mr, Serge COSNIER
Directeur de Recherche DCM, Grenoble, Directeur de thése
Mr, Michael HOLZINGER
Chargé deRecherche,DCM, Grenoble, Co-encadrant de thése

Abstract

The advancing field of medicine and environmental analysis demands sensitive and accurate methods for sensing harmful organic molecules. The research work in this thesis presents a novel affinity system for immobilization of bioreceptors, novel signal amplification strategies, and novel nanomaterial based bio-designs with the improved biosensor or bio-fuel cell (bio-cathode) performances.

Firstly, a new affinity system based on supramolecular host-guest interactions between biotin and β-cyclodextrin (β-CD) is studied where an association constant of 3×10^2 $L.mol^{-1}$ could be determined. This allows immobilization of a variety of commercially available biotin labelled bioreceptors on electrogenerated surfaces for biosensing application. β-CD modified gold nanoparticles (Au-NPs) were successfully applied as an "optical antenna" for additional SPRi signal amplification using quantum dot (QD) labels. The beneficial effect of the combination of these nano-objects enables the construction of highly sensitive DNA or immunosensors.

Secondly, various kinds of nanomaterials such as nanodiamonds, magnetic nanoparticles, carbon nanotubes (CNT), and graphene are employed to modify transducer surface followed by non-covalent functionalization with pyrene derivatives. The novel 3D layer-by-layer deposition of nanotubes and different sized nanoparticles with varying porosity presents a flexible approach towards construction of enzymatic or immuno-sensors. Graphene, a material with atomic thickness doubles the SPR sensitivity towards detection of an antibody. Finally, an efficient bioelectrocatalytic reduction of oxygen is reported using pyrene functionalized CNT forest as a bio-cathode for bio-fuel cell applications.

Keywords: Nanostructures, Biosensors, Electrochemistry, Surface plasmon resonance (SPR), Polymers, Bio-fuel Cells

Résumé

Bioarchitectures nanostructurées pour applications aux biocapteurs électrochimiques et optiques – Conception d'une biocathode pour biopiles à combustibles

Les avancées dans le domaine de l'analyse médicale et environnementale exigent des méthodes sensibles et précises pour la détection de molécules organiques nocives. Les travaux de recherche de cette thèse présentent un nouveau système d'affinité pour l'immobilisation de biorécepteurs, de nouvelles stratégies d'amplification du signal et de nouveaux nanomatériaux à base de modèles bio-inspirés afin d'améliorer les performances des biocapteurs ou des biopiles.

Dans une première partie, un nouveau système d'affinité supramoléculaire entre la biotine et la β-cyclodextrine (β-CD) a été étudié et a permis de déterminer une constante d'association de 3 x 10^2 $L.mol^{-1}$. Ce système permet l'immobilisation d'une grande variété de biorécepteurs commerciaux marqués avec une biotine sur des surfaces éléctrogénérées pour l'élaboration de biocapteurs. Des gold nanoparticles (Au-NPs) modifiées par des β-CD ont été utilisées avec succès comme "optical antenna" pour l'amplification additionnelle du signal SPRi utilisant des marqueurs quantum dot (QD). La combinaison de ces nano-objets permettent la construction d'immunocapteurs ou de capteurs à ADN très sensibles.

Dans une deuxième partie, différentes variétés de nanomatériaux tels que les nanodiamants, les nanoparticules magnétiques, les nanotubes de carbone (CNT) et graphène ont été utilisés pour modifier la surface des transducteurs suivie par leur fonctionnalisation non-covalentes par des dérivés pyrène. Le nouveau dépôt de nanotubes "layer-by-layer" et les différentes tailles de nanoparticules avec des porosités variables présentent une approche flexible pour la construction de capteurs enzymatiques et d'immunocapteurs. Le graphène est un matériel d'épaisseur atomique qui double la sensibilité SPR pour la détection d'anticorps et d'antigène. Enfin, une réduction bioélectrocatalytique efficace de l'oxygène est reportée en utilisant des CNT fonctionnalisés par les pyrènes pour une application comme biocathode dans les biopiles.

Mots-clés: Nanostructures, Biocapteurs, Electrochimie, Résonance plasmon de surface (SPR), Polyméres, Biopiles à combustibles

DEDICATED TO MY FAMILY

AND

FRIENDS

Acknowledgements

Alfred North Whitehead once quoted "No one who achieves success does so without the help of others. The wise and confident acknowledge this help with gratitude". So, I would like to acknowledge all the wonderful people who have contributed for the completion of my thesis work and this thesis would be incomplete without thanking them. First and foremost, I would like to thank my supervisors Dr. Serge Cosnier, Dr. Michael Holzinger and Prof. Maryam Tabrizian for providing me with the opportunity to complete my PhD thesis at the Université Joseph Fourier and McGill University.

I especially want to thank my supervisor on the spot, Dr. Michael Holzinger (also, my master thesis supervisor), his assistance throughout the course of this work. The many discussions and patient direction were invaluable to the completion of this thesis. I would like to thank my Co-director Prof. Maryam Tabrizian for providing me an opportunity to visit Canada, and perform a part of my thesis experiments at prestigious McGill University. I would like to thank again all of my three supervisors for careful reading of my thesis and helpful comments.

I have been extremely lucky to collaborate with different laboratories. I would like to thank Olga Bolivian of Laboratory of Biomolecular Electronics of the IMBG NANU, Ukraine to provide nanodiamonds. In my later work of graphene based biosensor and carbon nanotube forest based bio-cathode for bio-fuel cells, I'm especially grateful to Prof. Duesberg Group at CRANN, Trinity College in Dublin, Ireland to provide samples timely. I have appreciated their collaboration and the impressive skills to prepare graphene and nanotube forest.

I gratefully acknowledge the funding source that made my PhD work possible. I was funded by French-Canadian Research Funding (FCRF) for 3 years.

My time at BEA was made enjoyable in large part due to the many friends and groups that became a part of my life. I am grateful for time spent with my group members and friends, Karine, Chantal, Alan, Kamal, Saravanan, Fabien, Bertrand, Fatima, Noemie, Raoudha, and Mariem, for their patience to converse with me in English, and for many other people and memories. I am grateful to our group's technician Mme. Arielle Le Pellec and administrative secretary Mme. Regine Rozand who kept us organized.

Lastly, I would like to thank my amazing family for all their kindness, love, care and encouragement. For my father and mother who always supported me in all my pursuits. For my elder brother and newest member in our family, my sister-in-law to be always there. I would also like to thank my second family in France, my friend Priyanka (read my partner in crime), Dhruv, Virginie and Pierre for their love and support during my entire stay in France. I am thankful to all those who have been a part of this wonderful journey.

Merci à tous !!

Meenakshi Singh
Université Joseph Fourier
September 2014

Table of Contents

Scope

Bioelectronics is a developing area where the world of electronics could be combined with biology and nanotechnology. The major activities in the field of bioelectronics relate to the development of biosensors that transduce biorecognition or biocatalytic processes in the form of electronic signals. Other research efforts are directed at utilizing the biocatalytic electron transfer functions of enzymes to assemble biofuel cells that convert organic fuel substrates into electrical energy.

The work presented in this thesis focus on the development of electrochemical and optical (SPR) biosensors. We first investigated the novel strategies for the efficient immobilization of biological molecules onto the transducer surfaces. This involved testing of new affinity systems based on supramolecular host-guest interactions. Then, these biological macromolecules were immobilized by affinity interactions with electrogenerated polymers on the transducer surface. Monomers bearing bio-functionalities were synthesized and electropolymerized to generate thin films. These biological recognition systems were then applied to electrochemical and optical detection of various analytes. Finally, nanomaterials and nano-objects were incorporated for the amplification of sensitivity and detection limit of biosensors.

In **section I**, brief introduction of biosensor along with the detailed literature work presenting current state of the art of biosensor are presented. Furthermore, principles and examples of bio-fuel cell designs completes the state of the art section.

In **section II**, we report on a new affinity system without intermediate connectors such as avidin and metal ions based on the host–guest interactions between biotin and β-Cyclodextrin (**Chapter 2**). Glucose and PPO amperometric biosensors were constructed thereafter to evaluate the appropriateness of this newly developed affinity system (**Chapter 3**). Pyrrole biotin and pyrene β-CD were electropolymerised onto the transducer surface for the immobilization of GOx and PPO enzymes. An optical DNA sensor reflecting synergic effect of quantum dots and gold nanoparticles for SPR signal amplification using biotinylated surfaces has been addressed in **Chapter 4**.

Finally, **Section III** describes the nanostructuring of the electrodes using nanomaterials such as carbon nanotubes, nanodiamonds, magnetic nanoparticles, graphene and carbon nanotube forest for the application in biosensors and bio-fuel cells.

Chapter 5 and **6** are devoted to the construction of high performance amperometric glucose sensor and immunosensor based on 3D scaffolds made of nanotubes and nanodiamonds or magnetic nanoparticles. Within these chapters, the optimal conditions have been determined that these scaffolds allow unhindered permeation of substrates or analytes by assuring sufficient stability of the construction. With the size of the nanoparticles, the pore size of the scaffold could be controlled for the respective need.

Chapter 7 shows a graphene based SPR immunosensor, where graphene monolayer on gold surface was used to enhance the sensitivity of immunosensor.

An attempt utilizing carbon nanotube forest as a biocathode for direct electron reduction of oxygen has been made in **Chapter 8**.

Introduction

Section I

State of the art

Chapter 1

1.1 Biosensors

A biosensor contains an immobilized biological sensing element as a receptor unit, which can bind with target analytes and a transducer, which is responsible for the conversion of the said binding event into a processable signal (**Figure 1**). The selectivity of the biosensor for the target analyte is mainly determined by the bio-recognition element, whilst the sensitivity of the biosensor is greatly influenced by the transducer. Biosensors are usually categorized according to the transducer type (e.g., electrochemical, optical, piezoelectrical or thermal), or the biorecognition principle (e.g., enzymatic, immunoaffinity recognition, whole-cell sensor, or DNA) [1,2]. Thus, biosensors are devices that recognize and quantify specific molecules. The major areas of applications are in environmental monitoring, medical and health diagnosis, industrial safety, security for military applications, surveillance, and the automotive industry.

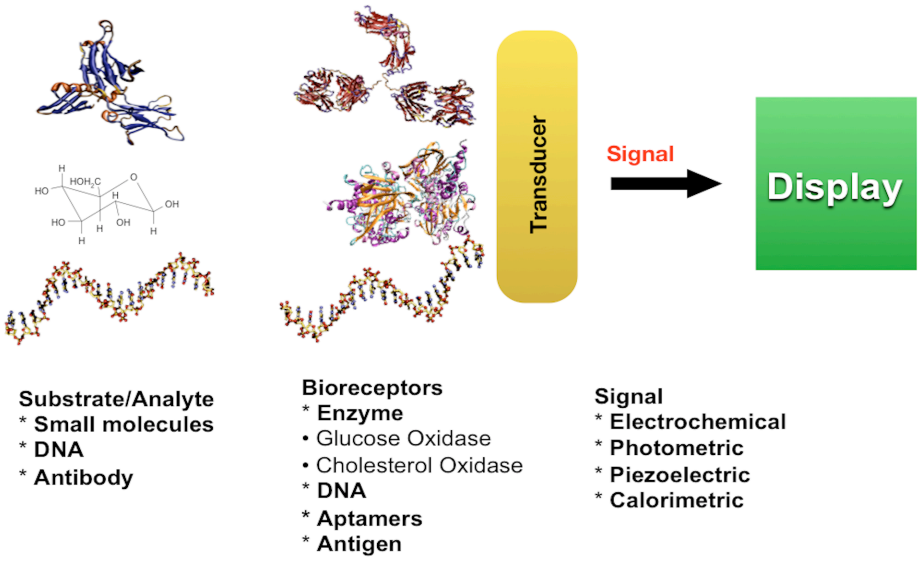

Figure 1. *Schematic representation of a biosensor.*

1.1.1. Bioreceptors or biological molecules

The specificity of biosensors is based on the bioreceptors used. A bioreceptor is a biological molecular species (*e.g.* an enzyme, an antibody, a protein, or a nucleic acid) or a living biological system (*e.g.* cells or whole organisms) that utilizes a biochemical mechanism for recognition. Bioreceptors allow binding the specific analyte of interest to the sensor for the measurement with minimum interference from other components in complex mixtures. The sampling component of a biosensor contains a bio-sensitive layer. The layer can either contain bioreceptors or be made of bioreceptors covalently attached to the transducer. The most common forms of bioreceptors used in biosensing are based on (a) enzymatic interactions, (b) nucleic acid interactions, (c) antibody–antigen interactions, (d) cellular interactions (*i.e.,* microorganisms, proteins), and (e) interactions using biomimetic materials (*i.e.,* synthetic bioreceptors) [3,4]. This section mainly discusses the class of biosensors that uses enzymes, DNA and antibody probes.

(a) Enzymes

Enzymes are catalytic proteins that have an exquisite specificity for certain molecular structures, referred to as their substrates. Enzyme catalyzes the transformation of the analyte or an auxiliary substrate into a product that contributes to the signal capturing (*e.g.* electrochemical or optical signal) [5]. They are used for the detection of inhibitors (heavy metals, CN^- etc.) via enzymatic reactions. For example, the poison cyanide is an irreversible enzyme inhibitor that combines with the copper and iron in the active site of the enzyme cytochrome c oxidase and blocks cellular respiration [6].

(i) Kinetics of enzymes

In relation to the usual parameters for Michaelis-Menten kinetics, *i.e.* K_M and V_{max}, enzyme-based biosensors are often characterized by their apparent K_M and V_{max}. The first parameter K_M represents the substrate concentration [S] yielding a response equal to half of its maximum value, V_{max} for maximum substrate concentration (**Figure 2A**). When the apparent K_M is much larger than its value for soluble enzyme, it means either that a significant substrate diffusion barrier is present between the sample and the reaction layer, or that the rate of reaction to the co-substrate, with the enzyme is increased. As for enzyme solution kinetics,

the apparent K_M is usually determined by Lineweaver-Burk reciprocal plots, *i.e.* 1/(V) versus 1 /[S], (**Figure 2B**) [7,8].

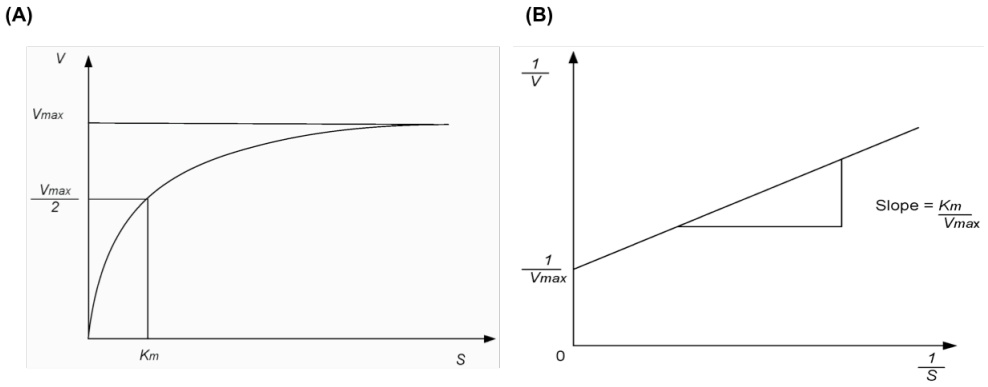

Figure 2. *Typical (A) Michaelis-Menten saturation curve and (B) Lineweaver-Burk reciprocal plot of an enzyme reaction.*

(ii) Glucose Oxidase (GOx)

GOx (EC 1.1.3.4.) is the standard enzyme for biosensors and has a relative high molecular weight (~ 130-180 kDa) [9]. GOx is easy to obtain, cheap, and can withstand wider pH ranges, ionic strengths, and temperatures than many other enzymes, thus allowing less stringent conditions during the manufacturing process [10,11]. The enzyme is comprised of two identical protein subunits containing one flavin adenine dinucleotide (FAD) coenzyme molecule, which is found in the active site. The FAD coenzyme molecule is tightly bound, yet not covalently attached to the enzyme [12]**.** During the enzymatic reaction between GOx and glucose, the FAD is reduced by the glucose producing $FADH_2$ and glucose is oxidized to gluconolactone [13,14]. The $FADH_2$ can then be oxidized by dissolved O_2 producing H_2O_2, regenerating the enzyme to its initial state [15] (**Scheme I**). H_2O_2 is then oxidized at the Pt-electrode at 0.6 V *vs* SCE or Ag/AgCl, leading to current increase, which is directly related to the glucose concentration.

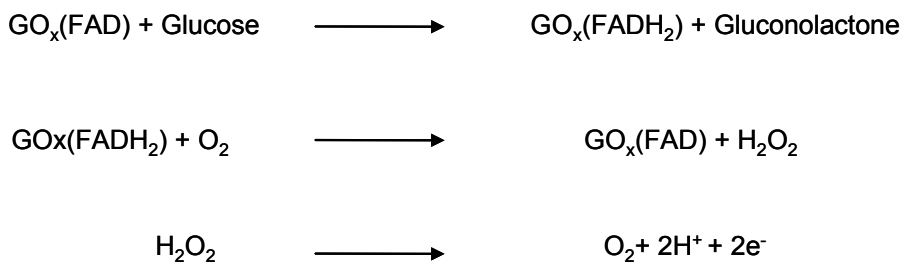

Scheme I. *Enzymatic activity of GOx and H_2O_2 oxidation equation of the electrochemical transduction.*

Glucose biosensors are some of the most successful biosensors on the market today. People living with diabetes require convenient methods for monitoring glucose levels. Implanted sensors and non-invasive sensors are under development, but currently, the most accessible approach is a handheld biosensor that analyzes a drop of blood. In the 1960s, Leland C. Clark [16] had an idea to hold the enzyme very close to a platinum electrode with a membrane, so that the chemical changes could be followed by watching changes in the current at the electrode. This reliable concept led to the development of a series of laboratory-sized instruments based on the sensing of peroxide. To make a portable and consistent glucose biosensor for home use, however, a change in methodology was needed. The oxygen-to-peroxide change is hard to standardize, because of the need for constant oxygen levels and interference by other molecules in the blood. Instead, a slightly different method was developed. Instead of oxygen, a mediator molecule is used to deliver the signal to the electrode. Ferrocene, a small molecule with an iron ion trapped between two cyclopentadienyl rings, was found to be an effective mediator. Handheld sensors that use disposable electrodes with enzyme and mediator are available commercially. Now, in a matter of seconds, glucose levels may be measured in a small drop of blood.

(iii) Polyphenyl Oxidase (PPO)

Polyphenol oxidase (EC 1.14.18.1.) is an enzyme of high molecular weight (~ 130 kDa) and present in many vegetables (mushrooms, potatoes, *etc.*). Its active site contains two Cu^{2+} ions each coordinated to three histidine amino acids. This enzyme catalyzes the oxidation of phenols such as catechol to benzoquinones (**Scheme II**). Since PPO catalyzes the oxidation of phenols and o-diphenols into o-quinone [17], the amperometric biosensor was potentiostated at the o-quinone reduction at –0.2 V *vs* SCE or Ag/AgCl.

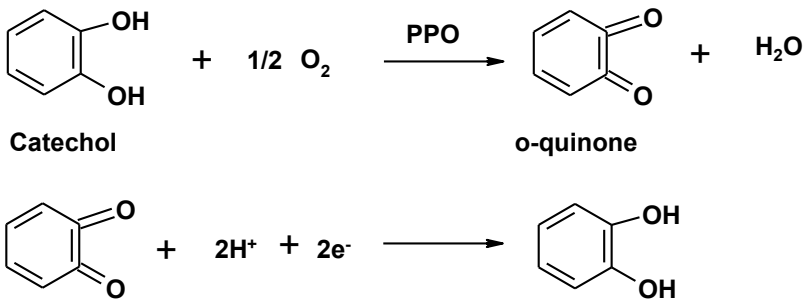

Scheme II. *Enzymatic activity of PPO and o-quinone reduction equation of the electrochemical transduction.*

Most of phenolic compounds show harmful effects on human health, animals and plants, which results in an acute environmental problem. So it is very important to develop quick and effective methods for the quantitative detection and control of the phenolic compounds. In recent years, amperometric polyphenol oxidase (PPO) biosensors have been extensively reported in the literature for the detection of various phenolic compounds due to its high sensitivity, fast response, simplicity, and easy miniaturization [18].

(iv) Horseradish Peroxidase (HRP)

Horseradish peroxidase (EC 1.11.1.7.) with a molecular weight of 44 kDa found in the roots of the horseradish plant. It is a glycoprotein with six lysine residues, which can be conjugated to a labelled molecule. In the presence of H_2O_2, immobilized peroxidase ($HRPFe^{3+}$) is oxidized to compound 1 (oxyferryl iron and porphyrincation radical). The latter is directly electroreduced (via an intermediate redox state; compound 2) to its native resting state (Fe^{3+}) at the electrode surface [19]. The oxidation products formed during the peroxidase reaction depend on the nature of the substrate. HRP catalyses the reduction of H_2O_2 and oxidation of hydroquinone to quinone species (**Scheme III**). The enzymatically generated quinone can then be reduced at the electrode at -0.1 V *vs* SCE or Ag/AgCl.

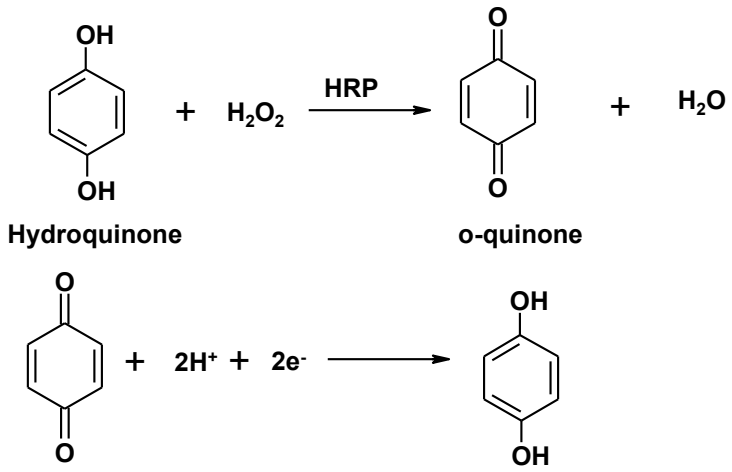

Scheme III. *Enzymatic activity of HRP and quinone reduction equation of the electrochemical transduction.*

HRP is often used in conjugates (molecules that have been joined genetically or chemically) to determine the presence of a molecular target. HRP is also commonly used in techniques such as enzyme-linked immunosorbent assay (ELISA) and immunohistochemistry due to its monomeric nature and the ease with which it produces coloured products.

(b) Nucleic Acids

Nucleic acids (NAs) are modular, linear chains of nucleotides, ranging up to hundreds of millions of nucleotides in length [20]. DNA was first identified and isolated by Friedrich Miescher and the double helix structure of DNA was first discovered by James Watson and Francis Crick, using experimental data collected by Rosalind Franklin and Maurice Wilkins [21,22]. The secondary structure of DNA is actually very similar to the secondary structure of proteins. The protein single alpha helix structure held together by hydrogen bonds was discovered with the aid of X-ray diffraction studies. The X-ray diffraction patterns for DNA show somewhat similar patterns. In addition, chemical studies by E. Chargaff indicate that in the DNA of all organisms the concentration of adenine (A) equals that of thymine (T) and the concentration of guanine (G) equals that of cytosine (C).

The structure of DNA (**Figure 3**) of all species comprises two helical chains each coiled round the same axis, and each with a pitch of 3.4 nm and a radius of 1 nm [22]. According to another study, when measured in a dilute aqueous solution, the DNA chain measured wide 2.2 to 2.6 nm wide, and one nucleotide unit measured 0.33 nm long [23].

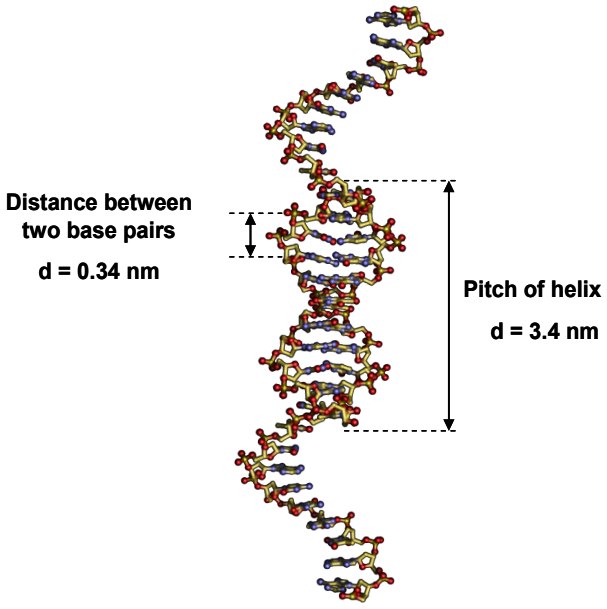

Figure 3. *Double – helix structure for DNA.*

The biorecognition process consists of non-covalent interactions between bases of complementary nucleic acid strands by Watson-Crick base pairing rules, and is manifested by hybridization of two single strands having such complementary base sequences. Exquisite specificity can be obtained due to the cumulative specific interaction of many bases to their complementary units on the opposite polynucleotide chain.

For the known sequence of bases in DNA molecule the complementary sequence, called a probe, will hybridize to its complementary sequence on the target molecule The formation of the duplex may be considered as evidence that the target has the expected nucleotide sequence (**Figure 4**). In nucleic acid biosensors, the probe is typically a oligodeoxyribonucleotide (ODN) or oligoribonucleotide with specific sequence of nucleotides (9–50 bases), which is able to hybridize with the specific target. The design of the probe is a crucial step of nucleic acid biosensor development, because the sequence specificity and yield of the hybridization are essentially dependent on the biorecognition properties of the probe [24].

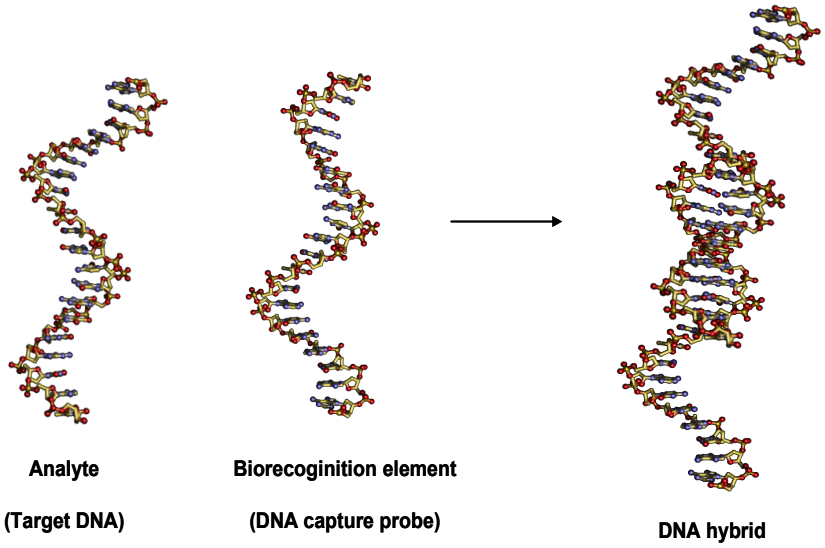

Figure 4. *Schematic represenstation of a DNA hybridisation involving capture of target DNA at the recognition DNA layer.*

Nucleic acid sensors are frequently coupled to schemes that utilize amplification of diagnostic nucleic acid sequences (for example, PCR, nucleic acid sequence-based amplification, rolling circle amplification, and so forth) with the potential for extreme sensitivity [25].

(c) Antibodies

An antibody is a complex biomolecule, made up of hundreds of individual amino acids arranged in a highly ordered sequence. Antibodies are produced by immune system cells (B cells) when such cells are exposed to substances or molecules, which are called antigens. The antibodies have recognition or binding sites for specific molecular structures (or substructures) of the antigen (**Figure 5**).

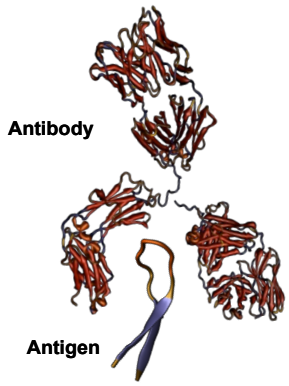

Figure 5. *Schematic representation of an immunosensor involving antibody-antigen interactins.*

An antibody fits its unique antigen in a highly specific way. This unique property of antibodies are crucial for their usefulness in immunosensors where only the specific analyte of interest, the antigen, fits into the antibody binding site [26]. The three-dimensional structures of antigen and antibody molecules are complementary. Due to this 3-D shape fitting, and the diversity inherent in the individual antibody make-up, it is possible to find an antibody that can recognize and bind to any one of a large variety of molecular shapes. This ability to recognize molecular structures allows one to develop antibodies that bind specifically to chemicals, biomolecules, microorganism components, etc. One can then use such antibodies as specific probes to recognize and bind to an analyte of interest that is present, even in extremely small amounts, within a large number of other chemical substances.

1.1.2 Transducers for bimolecular recognition

The biological sensing element responds to the analyte being measured and the transducer converts this observed change into a measurable signal that is proportional to the concentration of the analyte. The designed devices contain the appropriate offset and the amplification circuits that enable the small electrochemical or optical signal change due to the enzymatic reaction to be measured. A variety of traditional transducers are used, two basic

transduction types – electrochemical and optical are discussed in this section, with emphasis on the advantages and disadvantages of each method.

(a) Electrochemical transduction

Electrochemical transduction is one of the most popular transduction formats employed in biosensing applications. One of the main advantages of biosensors that employ electrochemical transduction is the ability to operate in turbid media and often in complex matrices. Another distinct advantage of electrochemical transduction is that the detection components are inexpensive and can be readily miniaturized into portable, low-cost devices.

In general, electrochemical-based sensing can be divided into four main categories: potentiometric, amperometric, cyclic voltammetric, and impedance. Potentiometric sensors typically rely on a change in potential caused by the production of an electroactive species that is measured by an ion selective electrode. For a biosensor system, this change in electroactive species concentration is usually brought about by an enzyme. In an amperometric sensor system, a change in current is directly measured. In cyclic voltammetry, information about an analyte is obtained by varying a potential and then measuring the resulting current. Electrochemical sensors based on impedance most commonly utilize impedance spectroscopy since controlled AC electrical stimulus over a range of frequencies is used to detect variations in the sensor surface properties (that is, charge transfer and capacitance at the interface layer). Some of the many variations of potentiometric, amperometric, and impedance biosensors that provide for improved biosensor performance include field effect transistors (FET) and electrochemiluminescence (ECL). This thesis mainly concerns with amperometric transducer, hence amperometric principle is described further in the following paragraph.

Amperometric transducer

Amperometric transduction is really easy and inexpensive compared to potentiometric and impedance transduction. Amperometry is based on the measurement of the current resulting from the electrochemical oxidation or reduction of an electroactive species. It is usually performed by maintaining a constant potential at a Platinum (Pt), Gold (Au) or Carbon (C) - based working electrode or an array of electrodes with respect to a reference electrode. The resulting current is directly correlated to the bulk concentration of the electroactive species or its production or consumption rate within the adjacent biocatalytic layer. Most of the amperometric biosensors described use enzymes as the biorecognition

element. Typically, oxidase and dehydrogenase enzymes have been the most frequently exploited catalysts used for these biosensor formats.

(b) Optical transduction

Optical biosensors are designed to translate changes in the propagation speed of light through a medium that contains biological material into a quantifiable signal proportional to the amount of biological material present on the sensor surface. In the design of optical biosensors, the detected biological material is often modeled as a thin film with a finite refractive index, although this is a simplification. Several studies have been performed to characterize the dielectric properties of representative molecular monolayer films [27,28]. Therefore, the design goal for all optical biosensors is to provide a transducer with some externally measurable characteristic that is modified by changes in dielectric permittivity on its surface.

Due to a number of advantages, optical transduction is one of the most widely used biosensor transduction formats. For example, optical transduction can be very rapid where the limiting factor for the speed of detection is often a diffusion-limited process of the biomolecular recognition event. Another advantage of optical transduction is that the interferences that can hinder electrochemical transduction measurements (such as voltage surges, harmonic induction, corrosion of electrode elements, and radio frequency interferences) are not present [29].

Some of the disadvantages of using optical transduction formats include detection challenges when analyzing turbid samples and the cost associated with detection system components. Due to the difficulty in detecting biological analytes directly through their intrinsic physical properties (such as mass, size, electrical impedance, or dielectric permittivity), biological research has historically relied upon attachment of some sort of "label" to one or more of the molecules/viruses/cells being studied. The label is designed to be easily, measured by its color or its ability to generate photons at a particular wavelength and acts as a surrogate to indirectly indicate the presence of the analyte to which it has been attached [29].

A wide variety of optical transduction formats have been employed, where changes of the interaction of light with the biomolecular system are used to produce a measurable signal. These changes can be based on differences in refractive index, production of chemiluminescent reaction products, fluorescence emission, fluorescence quenching, radiative and non-radiative energy transfer. These effects can be monitored using a variety of optical platforms including total internal reflectance and evanescent wave technologies, interferometric, resonant cavities, and biochip devices. The following paragraph addresses the popular emerging label-free optical transduction format, surface plasmon resonance.

Surface plasmon resonance (SPR)

SPR techniques are widely popular in contemporary biosensor development because it is a surface-sensitive technique that can measure real-time interactions between unlabeled species. SPR is a phenomenon that can exist at the interface between a metal and a dielectric material such as air or water. A surface plasmon (commonly excited by optical radiation) of the electrons at the surface of the metal results in an associated surface bond and evanescent electromagnetic wave of optical frequency. This evanescent wave has a maximal intensity at the interface and decays exponentially with distance from the interface. In SPR-based biosensing, changes at the interface (that is, biological recognition element and analyte binding) cause changes in the local refractive index, which in turn causes changes in the resonance excitation of the surface plasmon [30,31]. The optical excitation of plasmons occurs only under proper resonance conditions, that is, under conditions of attenuated total reflection (ATR) when the energy of the photons of light exactly equals the quantum energy level of the plasmons.

In 1968, Otto invented the attenuated total reflection (ATR) method to excite a surface plasmon [32]. Between the prism and metal layer is a layer with air. In 1971, the method was improved by Kretschmann by applying a thin metal film directly onto an ATR prism, denoted the Kretschmann configuration [33]. The Kretschmann configuration is the most used configuration. The SPR chip consists of a prism with a thin gold film upon which the bioreceptors are immobilized. Light is totally internally reflected from the metal-coated prism face, and the changes in reflectivity are measured. Surface plasmons are excited at a specific incident angle and result in a massive reduction in reflectivity at that angle. Changes in the refractive index at the interface result in a change of the optimal angle required for excitation.

Classic SPR spectroscopy is based on the monitoring of coupling angle, wavelength, intensity, and phase [34], whereas SPR imaging (SPRi) is based on the measurement of reflectivity of monochromatic incident light at a fixed angle by means of a charge couple device (CCD) camera. Compared with traditional SPR, SPRi offers main breakthroughs such as multiplexed detection and real-time visualization of the whole biochip surface. It monitors simultaneously multiple bioreceptor/analyte bindings with the parallel support of a digital image, representing the intensity of binding in a color scale [35]. On the other hand, SPRi suffers from order of magnitude worse resolution than classical SPR [36].

1.1.3 Characteristics of biosensors

This section will briefly list main performance criteria and discuss their relation to properties of the receptor and transducer parts of the electrochemical biosensors. In the following, the most common and most important characteristics of biosensors are discussed.

(a) Sensitivity

Sensitivity (S) is a vital parameter of the performance of a biosensor. For an amperometric biosensor, sensitivity is defined by the slope of change in current with change in concentration:

$$S = \frac{\mathrm{d(current)}}{\mathrm{d(concentration)}} \qquad (1)$$

This is, however, only straightforward if the sensor response is linear.

For optical biosensors, sensitivity is fundamentally determined by how efficiently the electromagnetic field associated with the optical transducer couples to biomolecules in contact with the sensor surface [37].

(b) Linear concentration range

The linear range of a sensor is defined as the range in which the sensor signal is proportional to a change in concentration. In most cases the (operational) range of a sensor corresponds to the linear range.

(c) Detection limit

The limit of detection (*LOD*) of a biosensor is one of the most important parameters to be determined. It is an especially critical performance criteria for detection of analytes present at low concentration or detection of adsorbed molecules with low molecular weight. The LOD is typically defined as

$$LOD = k \text{ x } std_{background} \quad (2)$$

Where k is the signal-to-noise ratio and $std_{background}$ is the standard deviation of the background signal. The value of k can be chosen deliberately depending on the desired accuracy of the *LOD* but is typically 3.

The sensitivity and the detection limit are related but are entirely different figures of merit. Sensitivity is used to define the lowest value determined above zero concentration while the detection limit describes the minimum resolvable difference between two measurements at any concentration [37].

(d) Response time

Response time is easily determined for each analyte addition. It is the time necessary for the output signal (current, reflectivity) to reach its maximum value following the analyte addition. Response time depend upon the analyte, co-substrate and product transport rates through different layers or membranes. Therefore, the thickness and permeability of these layers are essential parameters.

(e) Reproducibility, stability and lifetime

Sensor measurements are reproducible if the same results are obtained with different sensors in different laboratories with the same sensor architecture. If the sensor yields the same value of, for example, concentration in several measurements it's reproducible. Repeatability means several measures with the same biosensor.

Another measure for sensor performance that is a potential source of confusion is the stability of a sensor. Sensor stability can mean different things including but not limited to working stability, storage stability, and long-term stability.

1.2 Immobilization methods

Most of the biological molecules such as enzymes, antibodies, cells *etc.* have very short lifetime in solution phase. Thus, they have to be fixed in a suitable matrix. The immobilization of the biological component against the environmental conditions results in decreased enzyme activity [38,39]. The activity of immobilized molecules depends upon surface area, porosity, hydrophillic character of immobilizing matrix, reaction conditions and the methodology chosen for immobilization. The next section covers the main strategies employed for biomolecule immobilization.

1.2.1 Physical Adsorption

The physical adsorption utilizes a combination of electrostactic and hydrophobic forces, hydrogen bonds, and ionic forces to attach the biomaterial to the surface of the sensor (**Figure 6**). Many substrates such as cellulose, silica gel, glass, hydroxyapatite and collagen are well known to adsorb biocomponents. This method is very simple, however, employed forces are not very strong and biomolecules attached by this method may be released or not persist [40].

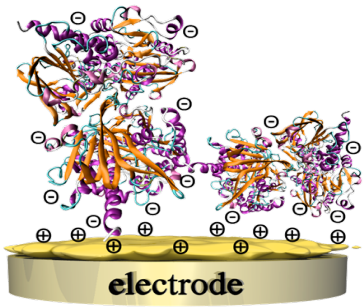

Figure 6. *Schematic representation of physical adsorption of biomolecules onto polymer films represented by electrostatic interactions.*

1.2.2 Matrix Entrapment

This strategy involves the immobilization of the biomolecules into a polymer composite material. A polymer composite, as the name implies, results if at least one of the phases is a polymer—either conducting or non-conducting. Non-conducting polymers are polymeric binders, such as starch, gels, epoxy, methacrylate, or silicone, which are used to impart a certain physical, chemical, or biological stability to the matrix [41]. Conducting polymers are basically organic conjugated polymers, offering many useful electrochemical characteristics such as low ionization potentials, high electric conductivity, and high electronic affinity.

Matrix entrapment by conducting polymer entails the application of an appropriate potential to a transducer soaked in aqueous solution containing both, biomolecules and monomers. The biological macromolecules in the immediate vicinity of the electrode surface are thus incorporated into the growing polymer (**Figure 7**). Because this entrapment process does not allow chemical reactions between the "*in situ*" formed polymers, the biomolecules thus preserve their biological activity. The advantage of electrochemical entrapment lies in the simplicity and speed of the one-step procedure [41]. It also allows the electrogeneration of polymers with precise spatial resolution over conductive surfaces, whatever their size and geometry.

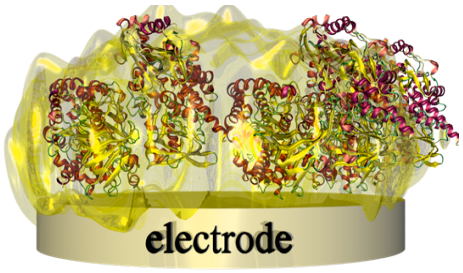

Figure 7. *Schematic representation of entrapment within a polymer matrix during its electrochemical growth.*

1.2.3 Direct electropolymerization of biomolecules

An alternative to the entrapment of biomolecules in polymers and the post-biofunctionalization of affinity films was to give electropolymerizable properties to the biomolecule itself (**Figure 8**). In 1992, Lowe *et al.* described the electropolymerization of glucose oxidase that was chemically modified with 30 pyrrole groups [42]. The covalent modification of GOx was carried out by coupling its amine-terminated protein shell with carboxyethyl pyrrole in the presence of carbodiimide. However, this concept of polypyrrole formation, also developed by Schuhmann *et al.,* was required to undergo a copolymerization process with regular pyrrole [43]. As a consequence, the enzyme immobilization resulted in a combination of entrapment and electrochemical polymerization rendering the enzyme less accessible. Recently, Papper *et.al.* has shown the direct electropolymerization of a protein concanavalin A-pyrrole on to a multi-walled carbon nanotube deposit [44].

The advantages of this approach are the simplicity and rapidity of the one-step procedure and the theoretically high biomolecule density of the resulting polymer film. Such

immobilization concepts are more applicable to small biomolecules such as peptides, short oligonucleotides, oligosaccharides, vitamins, and coenzymes [45,46].

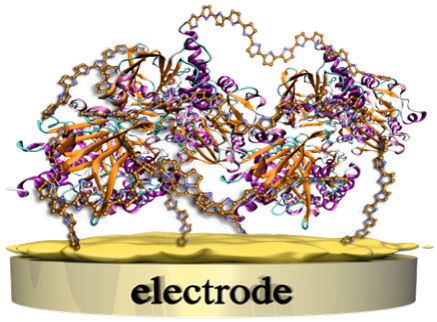

Figure 8. *Schematic representation of direct electropolymerization of biomolecules.*

1.2.4 Covalent binding between biomolecules and functionalized polymers.

With the aim of reducing the disadvantage related to the weak accessibility of entrapped biomolecules, investigators attempted to immobilize biomolecules by covalent linkage between biomolecules and polymers (**Figure 9**). The main advantage of this sequential procedure of electropolymerization and covalent binding is the possibility of satisfying optimal conditions for each step. This procedure is currently applied to the development of enzyme, immuno-, and DNA sensors [47].

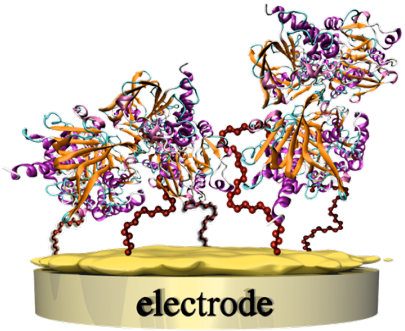

Figure 9. *Schematic representation of covalent binding between biomolecules and functionalized polymers.*

1.2.5 Attachment by affinity interactions between biomolecules and polymers

The chemical grafting of biomolecules onto electrogenerated films involves the irreversible formation of several covalent linkages per biomolecule that imply a potential loss

of catalytic activity or molecular recognition properties. Also, the biomolecule is linked to the surface in random orientations. However, the concept of biomolecule immobilization by affinity interactions should preserve the biological activity by formation of a single attachment point enabling a specific orientation. Generally, the films present molecular groups that can selectively interact with tags on the biomolecules *via* supramplecular interactions (**Figure 10**). In contrast to conventional chemical grafting, this step-by-step approach can also be applied to the preparation of multi-layered biotinylated biological assemblies. Another advantage of this approach is the ability to regenerate the transducer surface through denaturation of avidin by surfactants, high pH or protease attack [48].

Supramolecular interactions are based on weak and mostly reversible non-covalent assemblies between molecules like coordination with metal ions, hydrophobic forces, or π-π stacking interactions [49]. The aim of this thesis is to develop efficient immobilization methods for bioreceptors on transducer surfaces based on affinity interactions.

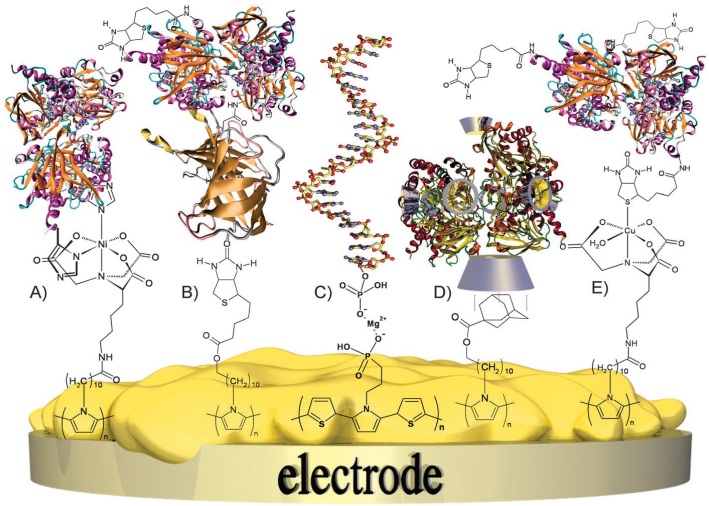

Figure 10. *Common affinity systems for biomolecules immobilization utilizing supramolecular interactions (A) Nitrilotriacetic acid/Ni^{2+}/histidine; (B) Biotin/avidin/biotin; (C) Phosphonate /Mg^{2+}/phosphate; (D) Adamantane/β-cyclodextrin; (E) Nitrilotriacetic acid/Cu^{2+}/biotin* [48].

The field of biosensor research is still probably in the stage where it is not clear which biorecognition elements/transducers/detection/immobilization schemes will be most productive. In general, robustness of the biorecognition element continues to be a concern for many applications. The use of transducers/detection mechanisms that involve sophisticated/ expensive instrumentation also will preclude such devices from many routine applications.

Unfortunately, a number of obstacles such as further development of sample preparation modules, sensitive detection modules, and robust assay methodologies still need to be overcome with regard to these systems. Another area receiving much recent interest is the area of nanotechnology, more specifically the use of nanomaterials in biosensor development. Nanostructured materials provide new approaches for developing new materials with dimensions on the nanoscale based upon molecular self-assembly. These nanomaterials have exceptional optical and electrical properties due to the electron and phonon confinement effects. Nanomaterials are receiving a great deal of attention as alternative matrices for biomolecule immobilization to improve stability and sensitivity of biosensors. Nanostructured materials provide high surface area for higher biomolecule loading and a biocompatible microenvironment, thus helping the biomolecule to retain its bioactivity.

1.3 Nanomaterials based biosensors

Materials exhibit new properties when scaled down from bulk material to nanometric dimensions. These properties can be precisely fine-tuned, thus allowing for the fabrication of defined structures and materials optimized for a certain purpose. Consequently, nanomaterials and concepts from nanotechnology have been much employed in biosensor development [50 – 53]. In the area of biosensor research, some features of nanostructures become important in addition to pure material properties. For instance, in nanometric structures diffusion lengths become very short and hence mass transport is highly efficient. Since mass transport is crucial in many biosensor designs, an increase or at least a change in sensor performance can be expected from using nanometric structures [54].

There are basically three broad categories of approaches towards nanobiosensors and, in particular, in electrochemical nanobiosensor development. The modification of a (macroscopic) transducer with nanomaterials is the first of these approaches. The second approach is the miniaturization of the transducer, namely the use of nanoelectrodes [55] or other miniaturized circuitry of nanometric dimensions. The modification of biomolecules with nanomaterials or coupling of biomolecules and nanomaterials is the third category of approach towards nanobiosensors. This thesis mainly deals with the first category *i.e.* modification of transducer with nanomaterials. The following section focuses mainly the introduction of different nanomaterials and current state of modes of detection, design considerations and innovative applications on biosensors. Gold nanoparticles (AuNPs), quantum dots (QDs), magnetic nanoparticle (MNPs), nanostructured carbon nanomaterials

such as nanodiamonds (NDs), carbon nanotubes (CNTs), and graphene are discussed in terms of their properties and application in biosensors.

1.3.1 Gold nanoparticles (AuNPs)

Over the past decade, the unique properties of nanoparticles have continued to attract considerable research attention. Nanoparticles, especially gold nanoparticles, offer excellent prospects for chemical and biological sensing because of their unique optical, electrical, and thermal properties as well as catalytic properties [56-58].

Due to their electrochemical properties, Au nanoparticles have been used as signal amplifiers in many electrochemical DNA biosensors. Wang *et al.* [59] demonstrated that Au nanoparticles could amplify the electrochemical impedance and capacitance signals for the model fluorescein/antifluorescein system. Amplification of voltammetric signal was also characterized by many researchers [60-62].

Optical properties of Au nanoparticles were also used for optical DNA biosensor. Yao *et al.* [63] used Oligonucleotide (ODN)-capped Au nanoparticles in a sandwich assay of ODN or polynucleotide by a flow injection surface plasmon resonance. Kuhn *et al.* have demonstrated a controlled enhancement of single-molecule fluorescence due to its near-field coupling with a gold nanoparticle [64].

1.3.2 Quantum dots

Quantum dots (QD) are colloidal nanocrystalline semiconductors, roughly spherical, with particle diameters typically ranging from 1–12 nm [65]. At such small sizes, these nanostructured materials behave differently from bulk solids, because of quantum-confinement effects [66]. In fact, when synthesized at the nanometer size and after adequate surface protection, these compounds develop intense and long-lasting luminescent emission with very narrow emission bandwidths (full width at half-maximum ~15–40 nm).

QDs typically have higher fluorescence quantum yields and better chemical and photoluminescence stability than conventional organic fluorophores. Furthermore, these nanocrystals have size-dependent tunable photoluminescense emission. The frequency of the light emitted by a specific quantum dot is related directly to its size; smaller particles tend to emit higher-energy (shorter wavelength) radiation. QDs also have unique attributes that make them superior to commercially available organic dyes when used for optical sensing. Thus,

quantum dots (QDs) offer unique absorption properties making them highly suitable for the construction of biosensors with optical readout.

Xu *et al.* [67] used a type of CdS QDs covalently binding with the amine groups modified target ssDNA to enhance the electrochemical impedance spectroscopy (EIS) signal. A. Sanz-Medel *et al.* review progress in exploiting the attractive luminescent properties of QDs in designing novel probes for chemical and biochemical optical sensing [68].

1.3.3 Magnetic nanoparticles (MNPs)

Magnetic nanoparticles are a powerful and versatile tool in a variety of analytical and biotechnological applications [69]. The use of non-porous magnetic beads greatly improves the performance of the immunological reaction, due to an increase in the surface area. These magnetic beads can be easy manipulated by using permanent magnets or electromagnets. This enables on the one hand that bioreceptor modified magnetic nanoparticles can be used to concentrate highly diluted analytes in complex media by simply applying an external magnetic field after the recognition event. On the other hand, magnetoresistive transduction can be applied when magnetic nanotags are used as labels [70].

1.3.4 Nanostructured carbon materials

Carbon takes many different forms. It has an excellent range of properties, which results from different electronic configurations, which give different geometrical structures. Carbon nanostructure have gained wide acceptance as powerful nanostructures matrices in biosensor and biofuel cell devices [71]. A significant enhancement in the performance of biosensing devices using three-dimensional architectures made of carbon nanomaterials has been noticed. By assembling different classes of nanocarbons into synergistic structures, it is possible to further expand material properties, resulting in novel applications. These carbon nanomaterials are dominantly used in this thesis as scaffold elements to construct the bioassemblies. This is why, these carbon nanomaterials are more intensively revised in the following section.

(a) Nanodiamonds (NDs)

Nanodiamonds (detonation nanodiamonds, DND) were first synthesized by the detonation method in 1962 [72]. The detonation or explosion method rests essentially on an attractive idea of using a shock wave to achieve the necessary high pressures and use the

carbon of the explosive itself as a starting material to produce crystalline diamond. Nanodiamond cluster size ranges between 2-10 nm with a very narrow peak of size distribution at about 4-5 nm [73]. The higher surface area-to-volume ratio of ND and the delicate balance of sp^2- sp^3 inherent in these composites allow it to act as a highly active electrode material.

Nanodiamonds possess a variety of surface functionalities that can be used to adsorb or graft functional groups or much more complex moieties, for example, proteins or DNA, onto the diamond surface [74]. Nanodiamonds are employed for drug delivery [75], biomedical imaging [76] and biosensors [77], due to their small size (~2-10 nm), surface structure, and inertness. The outstanding properties of nanodiamonds make them very promising candidates to form nanostructured electrode material for bioanalytics.

(b) Carbon nanotubes (CNTs)

CNTs have a tubular structure and consist of hexagonal honeycomb lattices made up of sp^2 carbon units. A schematic presentation of the structure of CNTs is shown in **Figure 11**. The diameters of CNTs are typically several nanometers. The length of CNTs can be up to several micrometers. Two basic forms are distinguished, single – walled carbon nanotubes (SWCNTs) and multiwalled carbon nanotubes (MWCNTs). SWCNTs are approximately 1 to 2 nm in diameter, while MWCNTs can range from 2 to 50 nm with an interlayer distance of 0.34 nm. CNTs can be up to hundreds of microns long. MWCNTs are made of several layers of graphitic cylinders. They are regarded entirely as metallic conductors, which in some regards, makes them better for electrochemical biosensors. However, SWCNTs are more well-defined layouts, allowing their electrochemical properties to be easily understood.

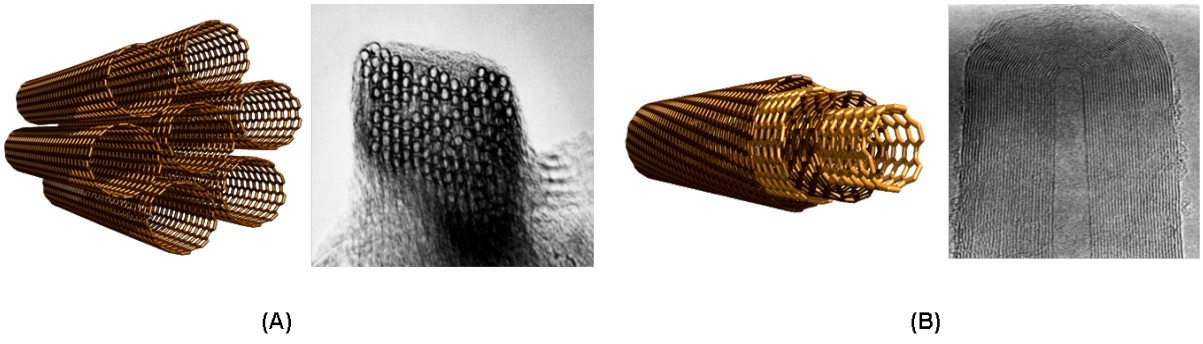

Figure 11. *TEM images of (A) SWCNTs and (B) MWCNTs, along with their schematic representations.*

(i) Production of CNT

CNTs have been fabricated since the early 1990s [78]. The primary research interests include the synthesis or growth of CNTs, because it was a challenging task to prepare enough amounts of CNTs with desired dimension and purity for measurement purpose during the early stage. With the development of processing method like arc discharge and laser ablation of graphite, as well as more productive chemical vapor deposition (CVD) and plasma enhanced CVD method, high purity CNTs with controllable wall-thickness/length and acceptable price are commercially available now [79].

(ii) Fabrication of CNT electrodes

An important technique in the fabrication process of CNT electrodes is the formation of nanocomposite electrodes. The fabrication of electrodes (often glassy carbon or gold electrodes) modified with CNTs typically suffers from the low solubility of CNTs in most commonly used solvents. Hence, CNTs are in many cases dispersed within solvents or polyelectrolytes and drop-coated onto the electrode to be modified. Alternatively, CNTs are incorporated within composite binding materials such as Teflon [80]. Another route to CNT - modified electrodes is the direct growth of CNTs on the electrode material [81].

(iii) Electrochemical functionalization of CNTs

Electrochemical functionalization offers several advantages, in particular *via* the easy control of the parameters of the electropolymerization. Polymers can be electrogenerated on SWCNT electrodes as shown in **Figure 12** or SWCNTs can be attached on the electrode during electropolymerization at the electrode. In the latter case, the fabrication of these composites takes benefits of the electrogeneration of the polymer to attach CNTs at the electrode. This method mainly consists of producing CNTs that are soluble in water and to electropolymerize a monomer in the presence of CNTs. It was demonstrated that negatively charged CNTs can act as polymer anionic dopants during the electrogeneration of conducting polypyrrole [82,83] or polyaniline [84]. A pyrrole monomer functionalized by a cationic triethylammonium group was also proposed and was revealed to act as a polymer precursor and surfactant for SWCNTs [85]. Many examples demonstrate the use of SWCNT/conducting polymer composite

electrodes in the specific electrochemical detection of bio-relevant small molecules such as dopamine [86], nitrite [87]or trifluoperazine [88].

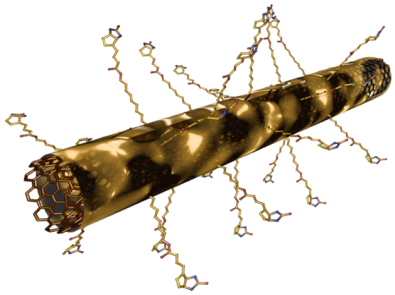

Figure 12. *Schematic representation of electrogenerated polymers on nanotube.*

(iv) Non-covalent functionalizaton of CNTs

One of the most prominent examples for the non-covalent functionalization of carbon nanotubes is the formation of π-π stacking interactions between molecules with highly conjugated π-orbital such as pyrenes, and nanotube sidewalls (**Figure 13**). Such interactions are formed even in non-protic but polar solvents, that allows non-covalent functionalization of nanotubes just by dip coating [89]. Adsorption of 1-pyrenebutanoic acid, succinimidyl ester and SWCNTs was first demonstrated by Chen *et al.*, resulting in the irreversible adsorption onto the side-wall of a SWCNT *via* π-stacking. Amine groups on a protein react with the anchored succinimidyl ester to form amide bonds for protein immobilization [90].

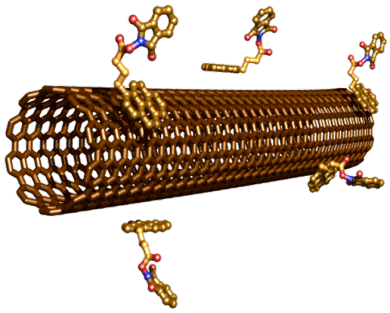

Figure 13. *Schematic representation of π-π interaction between nanotube and pyrene derivative.*

Non-covalent functionalization using pyrene derivatives is a particular powerful tool to functionalize carbon nanotubes and to attach affinity partners onto the nanotube sidewalls. Such functionalized nanotubes permits clear increases in biosensor performances. For example, Holzinger *et al.* has recently developed coatings on CNTs relying on the

electropolymerization of affinity binding polymers using avidin/biotin or adamantane/β-cyclodextrin interactions [91,92]. They used biotin functionalized pyrene and pyrrole derivatives to attach GOx as a biomolecule model to SWCNT electrodes. Compared to covalent functionalization, electropolymerization and π–stacking of pyrene preserve the pristine walls of SWCNTs and hence their conductivity. Furthermore, non-covalent functionalization of SWCNTs *via* π -stacking interactions localizes the affinity systems solely on the SWCNTs whereas electropolymerization leads to the modification of SWCNTs and the underlying electrode surface. As a consequence, the former approach provides higher accessibility for H_2O_2 to the electrode surface, thus increasing the sensitivity of the amperometric glucose biosensor.

Electrochemical biosensors based on CNTs have been used in the determination of a wide variety of analytes including glucose, fructose, cholesterol, lactate, catechols, hydrogen peroxide, alcohols, cholines, and organophosphates, as well as DNA and proteins [93]. The powerful combination of biorecognition and extraordinary electron transfer (ET) properties and material properties of CNTs can be expected to yield even more high - performance electrochemical biosensors in the near future.

(c) Graphene

Graphene, one of the newest nanomaterials used in biosensors, is a two-dimensional one-atom thick sheet made of pure carbon with atoms arranged in a repeating hexagonal pattern similar to graphite. As in graphite, the carbon atoms are sp^2 - hybridized in a densely packed honeycomb crystal lattice (**Figure 14**) [94]. Since graphene possesses the same basic structure as graphite and carbon nanotubes, it has many of the same physical properties. It is biocompatible, has fast electron transport, high thermal conductivity, and high mechanical strength [95]. Graphene is a zero-gap semiconductor material that is transparent, highly elastic, low cost and environmentally friendly [96] making it an attractive alternative for nanomaterial-based biosensors. Graphene has shown to be promising in chemical and biological sensor applications during the past several years [97–100].

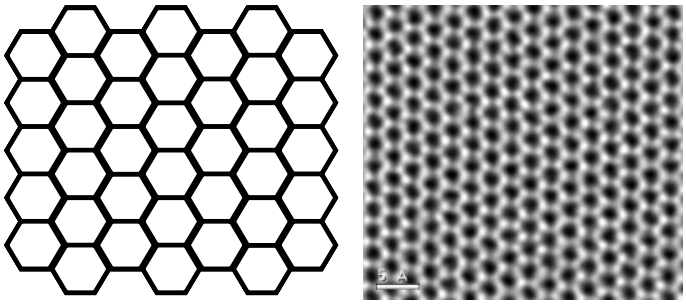

Figure 14. *Schematic representation of graphene along with a TEM image of graphene hexagonal lattice structure.*

Graphene also shows remarkable optical properties. For example, it can be optically visualized, despite being only a single atom thick [101,102]. Its transmittance (T) can be expressed in terms of the fine-structure constant [103]. The transmittance of a free standing single layer graphene can be derived by applying the Fresnel equations in the thin-film limit for a material with a fixed universal optical conductance [104], $G_0 = e^2/(4\hbar) \approx 6.08 \times 10^{-5}\,\Omega^1$, to give:

$$T = (1 + 0.5\,\pi\alpha)-2 \approx 1 - \pi\alpha \approx 97.7\% \qquad (3)$$

Where, $\alpha = e^2/(4\pi\varepsilon_0\hbar c) = G_0/(\pi\varepsilon_0 c) \approx 1/137$ is the fine structure constant. Graphene only reflects < 0.1% of the incident light in the visible region [103], rising to ~2% for ten layers [102]. Thus, we can take number of layers, each absorbing $A \approx 1 - T \approx \pi\alpha \approx 2.3\%$ over the visible spectrum.

The atomic thickness and strong broadband absorption of graphene cause it to exhibit very different reflectivity for transverse electric and transverse magnetic modes in the context of a total internal reflection structure, which is sensitive to the media in contact with the graphene. A graphene refractive index sensor can quickly and sensitively monitor changes in the local refractive index with a fast response time and broad dynamic range [104].

(i) Production of graphene

The term "graphene" used in literature includes a wide range of graphene–like structures which differ in the preparation method and, consequently in the chemical structure, shape and size. Graphene was first produced by micromechanical exfoliation of graphite [105]. This approach still gives the best samples in terms of purity, defects, mobility and opto-electronic properties. However, it is clear that large-scale assembly is needed for the widespread

application of this material. Several approaches have been developed to provide a steady supply of graphene in large areas and quantities, amenable for mass applications.

The first approach is exfoliation of highly oriented pyrolytic graphite (HOPG) using pieces of adhesive tape, which eventually leads to some single layers of graphene [106]. This technique produces the best-quality, least-modified forms of graphene, and is the main approach for scientific research.

Chemical methods have been also tried to upscale the graphene yields. As shown in **Figure 15A**, the first step is to oxidize graphene under strong acid, which creates a large number of oxygen-containing functional groups, such as carboxyl, epoxide and hydroxyl groups on the graphene surface [107]. These groups make graphene oxide (GO) hydrophilic and are thus able to be dissolved into a single sheet in water or polar organic solvents. The graphene oxide is then reduced by some compounds (like hydrazine) or by heating in a reducing atmosphere to regain to a certain extent the structure and property of graphene.

Chemical vapour deposition is the third approach and it can produce large areas of single layer graphene [108] by passing hydrocarbon vapors over metallic substrates, like Ni or Cu, heated to 1,000 °C (**Figure 15B**). One of the main challenges for the CVD method is in achieving a graphene layer with a mono-dispersed or controlled number of layers. A Cu substrate is believed, so far, to be the best substrate to make mono-layers of graphene.

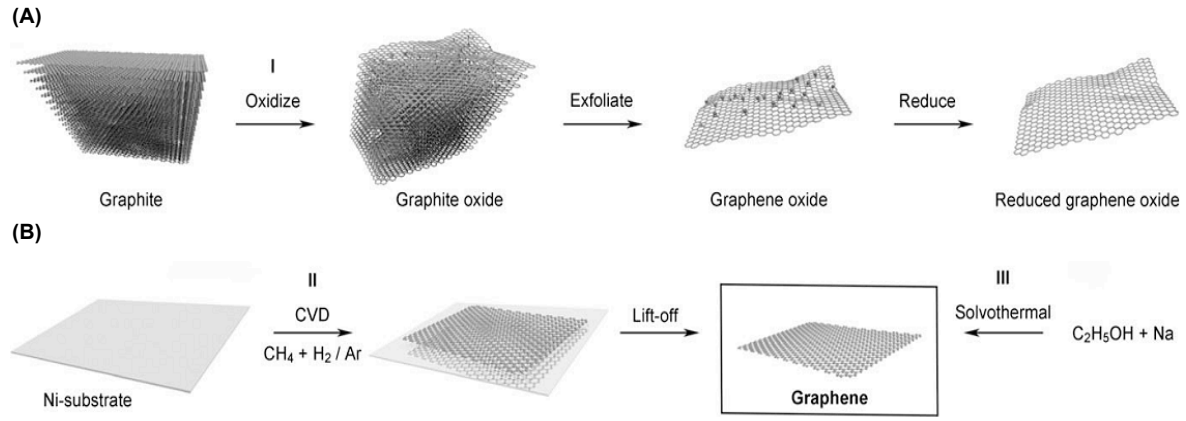

Figure 15. *Schematic representation of the approaches to produce graphene (A) by the oxidation–exfoliation–reduction process to generate individual sheets of reduced graphene oxide from graphite, and (B) by chemical vapour deposition (Method II, left) or by solvothermal reaction (Method III, right) [109].*

(ii) Non-covalent Functionalization of graphene

Graphene has a highly extended π-system. Non-covalent intermolecular interactions involving π-systems are pivotal to the stabilization of proteins, enzyme–drug complexes, DNA–protein complexes, organic supramolecules, and functional nanomaterials [110-114]. The presence of graphene layer also increases the adsorption of organic molecules due to π -π stacking.

Non-covalent functionalization by π-interactions (as in the case of carbon nanotubes) is an attractive synthetic method, because it offers the possibility of attaching functional groups to graphene without disturbing the electronic network [115]. The pyrene moiety has been reported to have a strong affinity toward the basal plane of graphite *via* π–stacking [116]. Xu *et al.* [117] prepared stable aqueous dispersions of graphene nanoplatelets using a water-soluble pyrene derivative, 1-pyrenebutyrate as a stabilizer. GO was functionalized with pyrene butyric acid in the presence of a base, and the resulting product was reduced with hydrazine. Graphene is much more flexible and less expensive than ITO since its precursor is hydrocarbon gas/graphite. To improve the power conversion efficiency of graphene, Wang *et al.* [118] non-covalently modified a graphene film with pyrene butanoic acid succidymidyl ester (PBSA). The π–π interactions between graphene and PBSA have a negligible effect on the optical adsorption of the graphene film in the visible region. This improved the power conversion efficiency to 1.71 % for functionalized graphene compared with pristine graphene (0.21 %). These π–interactions are thus of great importance in device and sensing applications of carbon nanotubes and graphene sheets.

In conclusion, as described for the nanostructures, the functionalization of all nano-objects, in order to immobilize the bioreceptor units for biosensing applications, is a constant challenge. Efficient methods for the bio-functionalization of nanomaterials have been addressed in this thesis work. Almost all nanomaterials can be equipped with appropriate functions via direct functionalization (in some cases already during synthesis), or *via* coating with functional polymers without affecting their specific properties [119]. Such functionalization not only allows the reproducible immobilization of bioreceptor units but can also increase the biocompatibility of these materials.

1.4 Biofuel Cells

A small modification can change a biosensor into a bioanode or a biocathode in a biofuel cell set-up. A fuel cell generally converts chemical energy into electrical energy in a continuous process as long as fuel is supplied. A sub-class of fuel cells are biofuel cells (BFCs) where the involved redox processes are generally catalyzed by enzymes in their purified form or within an organism. Biological fuel cells come in two main varieties: enzymatic and microbial. The goal of using these technologies is to develop environmentally friendly power sources capable of operation on fuels that would be readily available in the environment. These fuels would also be non-toxic and yield harmless emissions. The main difference between enzymatic and microbial fuel cells is which biological system is catalyzing the reaction. This thesis deals with enzymatic bio-fuel cells for the fabrication of bio-cathodes.

Enzymatic Biofuel Cells

In enzymatic biofuel cells, specific enzymes are tethered to two electrodes, performing reactions that supplies electrons from the fuel at one electrode (anode) by reducing oxygen or H_2O_2 at the other electrode (cathode). Enzymatic biofuel cells convert chemical energy by means of an enzymatic process as can be seen in **Figure 16**. The particularity of enzymatic biofuel cells is the high specificity towards the "fuel" (sugars, alcohols or hydrogen at the anode and the reduction of oxidants (O_2, H_2O_2) at the cathode to generate electrical power.

There are numerous and highly appealing advantages of enzymatic fuel cells (EFCs) in comparison with fuel cells (FCs): they are based on "green" catalysers (that can be mass-produced at demand in bioreactors instead of noble metals that requires highly polluting mining operations), the electrodes can be regenerated by the enzyme renewal (in comparison with the more difficult cleaning of the poisoned FCs). Thanks to the energy conversion under mild conditions (20°C - 40°C at neutral pH) and the specificy to the substrates, such electrical power generators can be used in complex media found in living organisms or vegetables with no separation between the bioanode and the biocathode [120-123]. It is therefore not necessary to work with liquefied hydrogen and there is as much energy in one jelly donut as in 77 cell phone batteries- only if we could transform it to usable energy as the living organism can [124]. These advantages made enzymatic biofuel cells promising power supplyers for portable electronic devices, biosensors, medical implants, or other type of biorelated electrical devices.

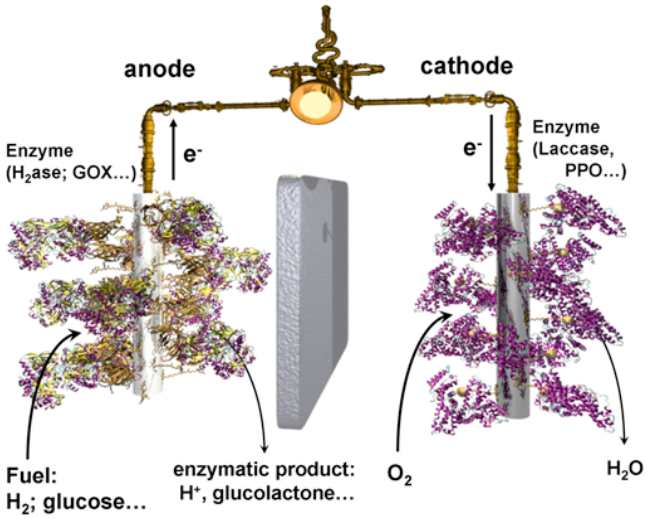

Figure 16. *Schematic representation of an enzyme biofuel cell.*

The typical reaction on the cathode side is the reduction of oxygen. The electron transfer (ET) pathway at the enzyme electrode can be mediated or direct. Enzymes that have been employed in biofuel cells relying on direct ET include laccases [125,126] which, however, suffer from a pH optimum in the acidic range and inhibition by halide ions. Thus, despite their favourable high potential for oxygen reduction they show poor stability in human tissue and fluids. Alternatively, bilirubin oxidase has been used as oxygen reduction biocatalyst in biofuel cell cathodes due to the better pH optimum and the insensitivity towards chloride ions. However, bilirubin oxidase has an about 200 mV lower reduction potential for molecular oxygen [127]. Alternatively, reduction of peroxide can be the cathodic reaction in biofuel cells. Relying on the experience with peroxidase - modified electrodes in biosensor research, electrodes modified with peroxidases have been shown to be highly efficient biocatalysts in biofuel cells [128,129].

The most common reaction at the anodic side of biofuel cells is the oxidation of sugars, which relies on the catalytic properties of oxidases. This class of enzymes has, however, usually poor potential for direct ET. Direct ET on the anodic site was, however, described for a number of hydrogenases [130,131] and cellobiose dehydrogenase [132,133]. Enzymatic catalysis by means of direct ET was also realized on conducting graphite, TiO_2 particles or nanotubes [134,135,136].

In conclusion, biofuel cells have a tremendous potential to be applied in, for example, implantable sensors or similar functional devices. They are a striking example of the continued development and application of the principles of biosensors employing direct ET.

1.5 Conclusion

This chapter presents a detailed overview of biosensor and its components. Various characteristics essential for determining the performance of a biosensor like sensitivity, detection limit are defined. The performance of a sensor mainly depends on the immobilization method of bioreceptors onto the transducer surface. The immobilization of biomolecules *via* affinity interactions, has received acceptance in recent years in binding biological species to surfaces on a solid support at a predetermined site while minimizing cross - contamination. Recent advances in the technological field and the use of new materials with molecular recognition properties, such as carbon nanotubes, graphene, micro and nanoparticles, have led sensor modifications to increase in selectivity, a marked sensitivity and simplification of the bioelectronic devices. Another class of bioelectronics devices i.e. biofuel cell and its current state-of-the-art is also summarized in the last section.

References

1. Bosch-Ojeda, C.; Sánchez-Rojas, F. Sensors. 2006, 6, 1245–1307.
2. Farré, M.; Kantiani, L.; Pérez, S.; Barcelo, D. 2009, 28, 170–185.
3. J. I. Reyes De Corcuera and R. P. Cavalieri, in Encyclopedia of Agricultural, Food, and Biological Engineering, Taylor & Francis, 2007, vol. null, pp. 119-123.
4. A. P. F. Turner, Chem. Soc. Rev., 2013, 42, 3184-3196).
5. D. Grieshaber, R. MacKenzie, J. Vörös and E. Reimhult, Sensors, 2008, 8, 1400
6. Yoshikawa S and Caughey WS. *J Biol Chem.* 1990, **265** (14): 7945–58.
7. Thevenot, D. R.; Toth, K.; Durst, R. A.; Wilson, G. S. Pure Appl. Chem., Vol. 71, No. 12, pp. 2333-2348, 1999.
8. Lineweaver, H and Burk, D. Journal of the American Chemical Society 1934. **56** (3): 658–666.
9. H. Kalisz, J. Hendle, R. Schmid, Appl Microbiol Biotechnol, 47 (1997), pp. 502–507
10. Wilson, R.; Turner, A.P.F. Biosens. Bioelectron. 1992, 7, 165-185.

11. Wohlfahrt, G.; Witt, S.; Hendle, J.; Schomburg, D.; Kalisz, H.; Hecht, H.J. Acta. Crystallog-D. Biol. Crystallogr. 1999, 55, 969-977.

12. Katz, E.; Shipway, A.N.; Willner, I. Wilson, G.S., Ed.; Wiley-VCH: Weinheim, Germany, 2002; Volume 9, pp. 559-626.

13.Harper, A.C.; Anderson, M.R. Electroanalysis 2006, 18, 2397-2404.

14.Heller, A.; Feldman, B. Chem. Rev. 2008, 108, 2482-2505.

15.Harper, A.C.; Anderson, M.R Electroanalysis 2006, 18, 2397-2404.

16.Clark, L.C., Jr; Lyons, C. Ann. N. Y. Acad. Sci. 1962, 102, 29-45.

17.S. Cosnier, I. Innocent, Bioelectrochem.Bioenerg. 31 1993 147–160.

18.Wang, X., Lu, X., Wu, L., & Chen, J. (2014). ChemElectroChem, 1(4), 681-681.

19. Arzum Erdem, Aysun Pabuccuoulc, Burcu Meruc, Kagan Kerman, Mehmet .ZS.Z, Turk J Med Sci, 30 (2000) 349-354

20. Saenger, Wolfram (1984). New York: Springer-Verlag.

21.Wilkins M.H.F., A.R. Stokes A.R. & Wilson, H.R. Nature 171, 738-740 (1953)

22.Watson J.D. and Crick F.H.C. (1953). Nature 171 (4356): 737–738.

23. Mandelkern M, Elias J, Eden D, Crothers D (1981). J MolBiol 152 (1): 153–61.

24. Šípová H, Homola J (2013). Anal Chim Acta 773:9–23

25. Liu, J., Cao, Z., & Lu, Y. (2009). Functional nucleic acid sensors.Chemical reviews, 109(5), 1948-1998.

26. Vo-Dinh T, Cullum B (2000) Fresenius. J. Anal. Chem. 366: 540—551.

27. Cole, T., Kathman, A., Koszelak, S., & McPherson, A. (1995). Analytical biochemistry, 231(1), 92-98.

28. Wen, J., Arakawa, T., & Philo, J. S. (1996). Analytical biochemistry, 240(2), 155-166.

29. Cooper, M. A. (Ed.). (2009). Cambridge University Press.

30. Liedberg, B., Nylander, C., & Lunström, I. (1983). Sensors and actuators, 4, 299-304.

31. Willets, K. A., & Van Duyne, R. P. (2007). Annu. Rev. Phys. Chem., 58, 267-297.

32. Z Naturforsch 23A:2135–2136 Otto A (1968). Z Phys 216:398–410

33. Kretschmann E (1971). Z Phys 241:313–324

34. Homola J (2003) Anal BioanalChem 377:528–539

35. Scarano S, Mascini M, Turner APF, Minunni M (2010) Biosens Bioelectron 25:957–66

36. Homola J (2008) Chem Rev 108:462–493

37. Borgmann, S., Schulte, A., Neugebauer, S., & Schuhmann, W. (2011). Amperometric biosensors. Advances in Electrochemical Science and Engineering.

38. Schuhmann, W., Lehn, C, Schmidt, H.L, Grundig, B., 1992. Sens. andActuat. B 7, 393–398.

39. Evtugyn, G.A, Budnikov, H.C., Nikolskaya, E.B., 1998. Talanta 46, 465–484.

40.Hanefeld, U.; Gardossi, L.; Magner, E. Chem. Soc. Rev. 2009, 38, 453–468.

41. N. C. Foulds and C. R. Lowe, J. Chem. Soc., Faraday Trans. 1, 1986, 82, 1259–1264.

42. S. E. Wolowacz, B. F. Y. Y. Hin and C. R. Lowe, Anal. Chem., 1992, 64, 1541–1545.

43. Schuhmann, W., Lammert, R., Uhe, B., & Schmidt, H. L. (1990). Sensors and Actuators B: Chemical, 1(1), 537-541.

44. Vladislav Papper, Kamal Elouarzaki, Karine Gorgy, Ayrine Sukharaharja, Serge Cosnier, and Robert S. Marks, Chem. Eur. J., 2014,20

45. J. B. Fiche, J. Fuchs, A. Buhot, R. Calemczuk and T. Livache, Anal. Chem., 2008, 80, 1049–1057.

46. E. Mercey, R. Sadir, E. Maillart, A. Roget, F. Baleux, H. Lortat- Jacob and T. Livache, Anal. Chem., 2008, 80, 3476–3482.

47. W. Schuhmann, R. Lammert, B. Uheaand H.-L. Schmidt, Sens. Actuators, B, 1990, 1, 537–541.

48. Serge Cosnier and Michael Holzinger, Chem. Soc. Rev., 2011, 40, 2146–2156

49. M. Holzinger, A. Le Goff and S. Cosnier, New J. Chem., 2014, in press (doi: 10.1039/C1034NJ00755G).

50. Pumera , M. , Sanchez , S. , Ichinose , I. , and Tang , J. (2007) Sensors and Actuators B , 123 (2), 1195 – 1205 .

51. Pandey , P. , Datta , M. , and Malhotra , B.D. (2008) Analytical Letters , 41 (2), 159 – 209 .

52. Zhang , X.Q. , Guo , Q. , and Cui , D.X. (2009 Sensors , 9 (2), 1033 – 1053 .

53. Urban , G.A. (2009) Measurement Science and Technology , 20 (1), 12001 .

54. M. Holzinger, A. Le Goff and S. Cosnier, Frontiers in Chemistry, 2014, 2, 63.

55. Arrigan , D.W.M. (2004) T he Analyst , 129 (12), ,1157 – 1165 .

56. Templeton, A.C.; Wuelfing, M.P.; Murray, R.W Chem. Res. 2000, 33, 27–36.

57. Antoine, O.; Bultel, Y.; Durand, R. J. Electroanal. Chem. 2001, 499, 85–94

58. Srivastava, C.; Balasubramanian, J.; Turner, C.H.; Turner, C.H.; Wiest, J.M. J. Appl. Phys. 2007, 102, 104310:1–104310:8.

59. Baca, A.J.; Zhou, F.M.; Wang, J.; Hu, J.B.; Li, J.H.; Wang, J.X.; Chikneyan, Z.S. Electroanalysis 2004, 16, 73–80.

60. Li, J.H.; Hu, J.B.; Ding, X.Q.; Li, Q.L Chem. J. ChineseUniv. 2005, 26, 1432–1436.

61. Wang, J.; Li, J.H.; Baca, A.J.; Hu, J.B.; Zhou, F.M.; Yan, W.; Pang, D.-W. Anal. Chem. 2003, 75, 3941–3945.

63. Yao, X.; Li, X.; Toledo, F.; Zurita-Lopez, C.; Gutova, M.; Momand, J.; Zhou, F.M. Anal. Biochem. 2006, 354, 220–228.

64. Sergei Kuhn, Ulf Hakanson, Lavinia Rogobete, and Vahid Sandoghdar, PRL 97, 017402 (2006)

65. Murphy, C.J.; Coffer, J.L. Appl. Spectrosc. 2002, 56, 16–27.

66. Alivisatos, A.P. Science 1996, 271, 933–937.

67. Xu, Y.; Cai, H.; He, P.G.; Fang, Y.Z. Electroanal. 2004, 16, 150–155.

68. Costa-Fernández, J.M.; Pereiro, R.; Sanz-Medel, A. Trends Anal. Chem. 2006, 25, 207–218.

69. Richardson, J.; Hawkins, P.; Luxton, R.Biosens. Bioelectron. 2001, 16, 989–993.

70. J. B. Haun, T.-J. Yoon, H. Lee and R. Weissleder, Wiley Interdisciplinary Reviews: Nanomedicine and Nanobiotechnology, 2010, 2, 291-304

71. Nardecchia, S., Carriazo, D., Ferrer, M. L., Gutiérrez, M. C., & del Monte, F. (2013). Chemical Society Reviews, 42(2), 794-830.

72. Danilenko, V. V. Phys. Solid State 46, 595–599 (2004). .

73. Kuznetsov, V.L.; Chuvilin, A.L.; Butenko, Y.V.; Malkov, I.Y.; Titov, V.M. Chem. Phys. Lett.,v. 222, p. 343, 1994

74. Anke Krueger, Chem. Eur. J. 2008, 14, 1382 – 1390

75.Chow EK, Zhang X-Q, Chen M, Lam R, Robinson E, Huang H. SciTranslMed 2011;3(73):73ra21.

76. 19. Chang Y-R, Lee H-Y, Chen K, Chang C-C, Tsai D-S, Fu C-C, et al Nat Nanotechnol 2008;3(5):284–8.

77. Villalba P, Ram MK, Gomez H, Kumar A, Bhethanabotla V, Kumar A. MaterSciEng C 2011;31(5):1115–20.

78. S. Iijima, Nature (1991). 354 , 56.

79. M. Meyyapan (2005)., CRC Press, LLC

80. Wang , J. and Musameh , M. (2003) Analytical Chemistry , 75 (9), 2075 – 2079 .

81. Nguyen , C.V. , Delzeit , L. , Cassell , A.M. , Li , J. , Han , J. , and Meyyappan , M.(2002) Nano Letters , 2 (10), 1079 – 1081 .

82. U. Lange, N. V. Roznyatovskaya and V. M. Mirsky, Anal. Chim. Acta, 2008, 614, 1.

83. M. Hughes, G. Z. Chen, M. S. P. Shaffer, D. J. Fray and A. H. Windle, Chem. Mater., 2002, 14, 1610.

84. E. Granot, B. Basnar, Z. Cheglakov, E. Katz and I. Willner, Electroanalysis, 2006, 18, 26.

85. S. R. Ali, Y. Ma, R. R. Parajuli, Y. Balogun, W. Y.-C. Lai and H. He,Anal. Chem., 2007, 79, 2583.

86. Y. Li, P. Wang, L. Wang and X. Lin, Biosens. Bioelectron., 2007, 22, 3120.

87. G. Jin, F. Huang, W. Li, S. Yu, S. Zhang and J. Kong, Talanta, 2008, 74, 815.

88. M. Holzinger, J. Baur, R. Haddad, X. Wang and S. Cosnier, Chem. Commun., 2011, 47, 2450–2452.

89. Chen, R. J. ; Zhang, Y. ; Wang, D. ; Dai, H. J. Am. Chem. Soc. 2001, 123, 3838-3839.

90. M. Holzinger, R. Haddad, A. Maaref and S. Cosnier, J. Nanosci.Nanotechnol., 2009, 9, 6042.

91. R. Haddad, S. Cosnier, A. Maaref and M. Holzinger, Analyst, 2009, 134, 2412.

92. Ahammad , A.J. , Lee , J.J. , and Rahman ,M.A. (2009) Sensors , 9(4), 2289 – 2319 .

93. Novoselov, K.S.; Geim, A.K.; Morozov, S.V.; Jiang, D.; Zhang, Y.; Dubonos, S.V.; Grigorieva, I.V.; Firsov, A.A. Science 2004, 306, 666–669.

94. Kuila, T.; Bose, S.; Khanra, P.; Mishra, A.K.; Kim, N.H.; Lee, J.H. Biosens. Bioelectron. 2011, 26, 4637–4648.

95. Pumera, M. Graphene in biosensing. Mater. Today 2011, 14, 308–315.

96. Ratinac, K.R.; Yang, W.; Gooding, J.J.; Thordarson, P.; Braet, F. Electroanalysis 2011, 23, 803–826.

97. Jiang, H. Small 2011, 7, 2413–2427.

98. Shao, Y.; Wang, J.; Wu, H.; Liu, J.; Aksay, I.A.; Lin, Y. Electroanalysis 2010, 22, 1027–1036.

99. Lu, Q.; Dong, X.; Li, L.J.; Hu, X. Talanta 2010, 82, 1344–1348.

100. Casiraghi, C. et al. Nano Lett. 7, 2711–2717 (2007).

101. Blake, P. et al. Appl. Phys. Lett. 91, 063124 (2007).

102. Nair, R. R. et al.Science. 320, 1308–1308 (2008).

103. Novoselov, K. S. et al..Proc. Natl Acad. Sci.USA102, 10451–10453 (2005).

104. Xing, F., Liu, Z. B., Deng, Z. C., Kong, X. T., Yan, X. Q., Chen, X. D, & Tian, J. G. (2012). Scientific reports, 2.

105. Kuzmenko, A. B., van Heumen, E., Carbone, F. & van der Marel, D. Universal optical conductance of graphite. Phys. Rev. Lett. 100, 117401 (2008).

106. Novoselov, K.S.; Geim, A.K.; Morozov, S.V.; Jiang, D.; Zhang, Y.; Dubonos, S.V.; Grigorieva, I.V.; Firsov, A.A. Science 2004, 306, 666–669.

107. Park, S.; Ruoff, R.S. Nat. Nanotechnol.2009, 4, 217–224.

108. Reina, A.; Jia, X.T.; Ho, J.; Nezich, D.; Son, H.B.; Bulovic, V.; Dresselhaus, M.S.; Kong, J. NanoLett. 2009, 9, 30–35.

109. Yang, W.; Ratinac, K.R.; Ringer, S.P.; Thordarson, P.; Gooding, J.J.; Braet, F. Angew. Chem. Int. Edit.2010, 49, 2114–2138.

110. Meyer, E. A.; Castellano, R. K.; Diederich, F. Angew. Chem., Int.Ed.2003, 42, 1210.

111. Burley, S. K.; Petsko, G. A. Science 1985, 229, 23.

112. Hong, B. H.; Lee, J. Y.; Lee, C. W.; Kim, J. C.; Bae, S. C.; Kim, K.S. J. Am. Chem. Soc. 2001, 123, 10748.

113. Singh, N. J.; Lee, H. M.; Hwang, I.-C.; Kim, K. S. Supramol.Chem. 2007, 19, 321

114. Lee, J. Y.; Hong, B. H.; Kim, W. Y.; Min, S. K.; Kim, Y.; Jouravlev,M. V.; Bose, R.; Kim, K. S.; Hwang, I. C.; Kaufman, L. J.; Wong, C. W.;Kim, P.; Kim, K. S. Nature 2009, 460, 498.

115. Karousis, N.; Tagmatarchis, N. Chem. Rev. 2010, 110, 5365.

116. Jaegfeldt, H.; Kuwana, T.; Johansson, G. J. Am. Chem. Soc. 1983,105, 1805.

117. Xu, Y.; Bai, H.; Lu, G.; Li, C.; Shi, G. Q. J. Am. Chem. Soc. 2008,130, 5856.

118. Wang, Y.; Chen, X.; Zhong, Y.; Zhu, F.; Loh, K. P. Appl. Phys.Lett. 2009, 95, No. 063302.

119. Biju, V., Chem. Soc. Rev.43 (3), 744 (2014).

120. Barton, S. C., Gallaway, J., and Atanassov, P., Chem. Rev.104 (10), 4867 (2004).

121. Atanassov, P., Apblett, C., Banta, S., Brozik, S., Barton, S. C., Cooney, M., Liaw, B. Y., Sanjeev Mukerjee, and Minteer, S. D., The Electrochemical Society Interface16 (2), 28 (2007).

122. Cracknell, J. A., Vincent, K. A., and Armstrong, F. A., Chem. Rev.108 (7), 2439 (2008).

123. Zayats, M., Willner, B., and Willner, I., Electroanalysis20 (6), 583 (2008).

124. Willner, I., Yan, Y.-M., Willner, B., and Tel-Vered, R, Fuel Cells9 (1), 7 (2009).

125. Johnson , D.L. , Thompson , J.L. , Brinkmann , S.M. , Schuller , K.A. , and Martin , L.L. (2003) Biochemistry, 42 (34), 10229 – 10237 .

126. Blanford , C.F. , Foster , C.E. , Heath , R.S. , and Armstrong , F.A. (2008) Faraday Discussions , 140 , 319 – 335 .

127. Kang , C. , Shin , H. , and Heller , A. (2006) Bioelectrochemistry, 68 (1), 22 – 26 .

128. Pizzariello , A. , Stredansky , M. , and Miertus , S. (2002) Bioelectrochemistry, 56 (1 – 2), 99 – 105 .

129. Mondal , M.S. , Goodin , D.B. , and Armstrong , F.A. (1998) Journal of the American Chemical Society , 120 (25), 6270 – 6276 .

130. Vincent , K.A. , Cracknell , J.A. , Parkin , A. , and Armstrong , F.A. (2005) Dalton Transactions , 3397 – 3403 .

131. Coman , V. , Ludwig , R. , Harreither , W. , Haltrich , D. , Gorton , L. , Ruzgas , T. , and Shleev , S. (2010). FuelCells, 10(1), 9 – 16 .

132. Lindgren , A. , Stoica , L. , Ruzgas , T. , Ciucu , A. , and Gorton , L. (1999) The Analyst , 124 (4), 527 – 532 .

133. Stoica , L. , Ludwig , R. , Haltrich , D. , and Gorton , L. (2006) ,Analytical Chemistry , 78 (2), 393 – 398 .

134. Vincent , K.A. , Li , X. , Blanford , C.F. , Belsey , N.A. , Weiner , J.H. , and Armstrong , F.A. (2007) Nature Chemical Biology , 3 (12),760 – 761 .

135. Reisner , E. , Powell , D.J. , Cavazza , C. ,Fontecilla - Camps , J.C. , and Armstrong ,F.A. (2009) Journal of the American Chemical Society , 131 (51), 18457 – 18466 .

136. Holzinger M., Le Goff, A., and Cosnier, S. Electrochimica Acta, 82, 179-190.

Affinity-Based Biosensors

Section II

Biotin – β-cyclodextrin:

A new affinity system

Chapter 2

2.1 Context

In this chapter, a new affinity system based on the supramolecular host guest interactions between biotin and β-cyclodextrin has been studied. Affinity systems are based on supramolecular interactions, including hydrophobic or electrostatic interactions, and coordination chemistry with metal complexes [1]. The immobilization of bioentities *via* affinity interactions is a powerful tool in bioanalytical devices that provides often clear advantages for the design of biosensors and biofuel cells. Affinity systems can be attached to the biomolecules in a reproducible way at an industrial scale without or barely affecting their biological activity.

Affinity binding provides specific and strong attachment of biomolecules modified with corresponding affinity partners. Affinity interaction describes usually the formation of specific supramolecular host-guest complexes between two affinity partners. The first and still most used affinity system for the immobilization of almost all types of bioreceptors (proteins, DNA strands and bacteria) is the biotin–(strept)avidin system. All proteins of the avidin family are composed by four identical subunits, each capable of forming a strong inclusion complex with biotin, known as vitamin B7 or vitamin H5 (**Figure 1**). The association constants can be up to $K_a = 10^{15}$ L.mol^{-1} [2] and are comparable with covalent bonds.

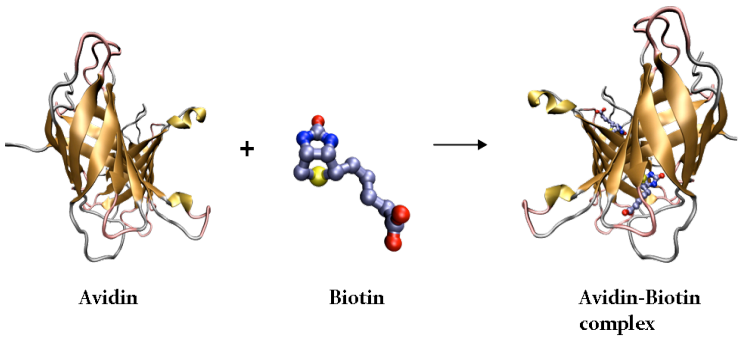

Figure 1. *Avidin- Biotin complex.*

A further advantage of this affinity system is that the carboxylic acid group of the anchor biotin can be easily modified via ester or amide formation. This allows not only efficient biotin coating of surfaces but also biotinylation of proteins or amine modified DNA strands. The success of this approach lies mainly in the vast range of commercially available biotinylated biomolecules produced for the ELISA used in clinical tests. In addition, taking into account that biotinylated proteins exhibit several biotin moieties randomly localized onto the protein shell, this affinity system is unique in enabling the formation of several layers of protein.

However, the weak point of this immobilization strategy is the size of compact avidin bridge layers. The presence of an intermediate layer has a detrimental effect on the biosensor sensitivity for immunoreaction or hybridization detection. An alternative to this approach is the use of polymeric affinity systems, which mimic the biological avidin-biotin interactions in order to replace the protein bridge by smaller metal ions.

In 1999, a second affinity system initially developed for chromatography and involving immobilization on metal ions, was reported for the fabrication of biosensors. This approach involves the formation of specific interactions between a chelated Ni^{2+} ion and histidine tags. The metal ions were immobilized in polymers, enabling the anchoring of histidine tagged proteins [3]. Finally, a novel and simple immobilization strategy for biotinylated biomolecules onto electropolymerized poly(pyrrole-nitrilotriacetic acid) (NTA)-Cu^{2+} films without avidin as a connecting bridge was reported in 2005 [4]. This presents the advantage to estimate the amount of coordinated metal through the reduction of Cu^{2+} into Cu. This electrochemical reduction can also be used to renew the biological layer via its decomplexation.

Thanks to the polymerized chelating NTA group, the polymer enables the conventional coordination of Cu^{2+} and then the coordination of the histidine/biotin [4,5] group onto the chelated Cu^{2+} centers (**Figure 2**). This system combines the advantages of the affinity systems biotin/(strept)avidin and NTA/Ni^{2+}/oligo-histidine by eliminating the detriments of each system.

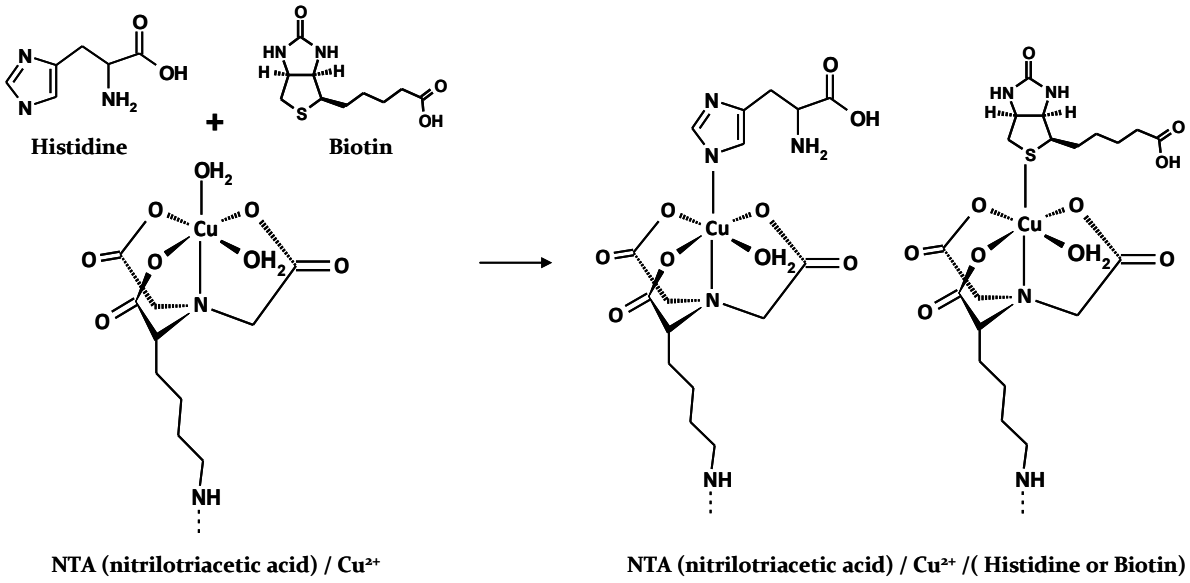

Figure 2. *Nitrilotriacetic acid/Cu^{2+}/ histidine or biotin affinity system.*

Within the cyclodextrin family, β-cyclodextrin (β-CD) is the mostly used version for the immobilization of biomolecules via supramolecular inclusion complexes. Cyclodextrins (CD) are cyclic oligosaccharides composed by usually more than six α-D-glucopyranoside units linked in 1,4 - position. The most prominent examples are α-CD (6 units), β-CD (7 units), and γ-CD (8 units). This particular confirmation leads to a shallow truncated cone structure where the smaller rim is seamed with primary hydroxyl groups and the larger rim bears secondary hydroxyl groups. Against these highly hydrophilic rims, the "wall" of the cone is constituted by the six membered core ring of the glucopyranoside units containing C–H groups and glycosidic oxygen [6] that result in a more hydrophobic character. Due to this particular structural property, cyclodextrins became prominent for their capacity to form stable supramolecular complexes with a large variety of molecules. Cyclodextrins are primarily used for solubilization, masking of compounds, chromatography, and many more. Their biocompatibility and their nontoxicity led furthermore to applications in cosmetics and pharmaceutics [7]. In particular, β-cyclodextrin (β-CD) provides an ideal geometry for acting as host for small hydrophobic molecules such as adamantane or pyrene [8]. These moieties served for the efficient immobilization of β-CD tagged biomolecules for biosensing applications.

Villalonga *et al.* [9] presented for the first time an immobilization strategy for enzymes based on the supramolecular interactions between β-CD and adamantane without intermediate connectors such as avidin and metal ions (**Figure 3**). Adamantane is a pure and

extremely hydrophobic hydrocarbon with an ideal size to form an inclusion complex with β-CD with a relatively high association constant of $K_a = 5.2 \times 10^4$ L.mol^{-1} [10]. This original affinity system was further applied for the construction of an efficient glucose sensor after electropolymerization of an adamantyl–pyrrole derivative on CNT electrodes [11]. This polymer was successfully applied to attach directly, without the need of an intermediate protein layer, β-CD modified GOx.

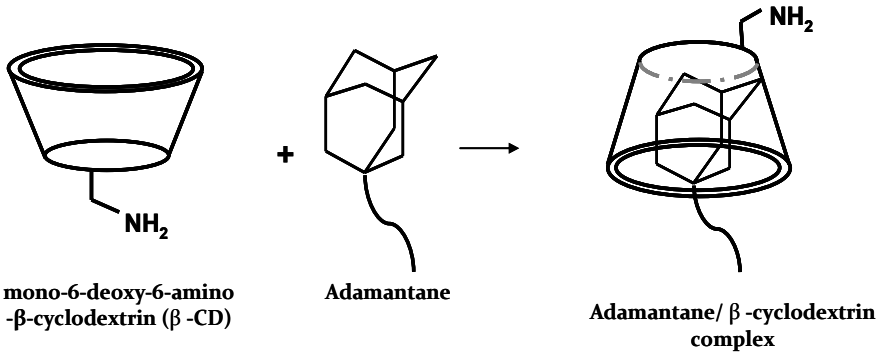

Figure 3. *Adamantane/β-cyclodextrin affinity system.*

2.2 Biotin–β-cyclodextrin: A New Host–Guest System for the Immobilization of Biomolecules

Against hydrocarbons like adamantane and pyrene, biotin is the most used functionality to immobilize biotin tagged bioreceptor units due to its high affinity to form inclusion complexes with the glucoproteins avidin and streptavidin [12]. Even when biotin is considered as a water-soluble vitamin, only concentrations below 220 μg.mL^{-1} were reported [13]. There are several examples where biotin and β-CD were combined in order to form, *e.g.*, pseudo rotaxanes using biotin terminated PEG and fluorophore modified β-CD [14]. Biotinylated β-CDs were synthesized to capture fluorophores inside the cyclodextrin unit immobilized via avidin bridges [15] and were also patented as skin cosmetics [16]. Furthermore, a bis(adamantyl)- biotin compound was used as cross-linker to detect the Fc fragment of a human immunoglobin G *via* streptavidin bridges immobilizing the biotinylated protein A as the receptor unit [17,18]. None of these studies evoked the possibility of an inclusion complex between biotin and β-CD.

Still, such a host–guest system could represent a significant advantage where the sensor construction procedure steps can be reduced, but also could provoke interferences or parasite

reactions. In this chapter, the following described experiments focus on the investigation and evaluation of a new immobilization technique using the formation of an inclusion complex between biotin and β-CD. In particular, immobilization *via* supramolecular interactions using biotin as anchor molecule has the advantage that biotinylated bioreceptors and biotin-modified surfaces are easily available and even, to a certain extent, commercialized. Biotin coordinates with copper-NTA complexes that were allowed to omit the disadvantageous (strept)avidin layer for the biosensor construction [5]. Along this vein, we studied the supramolecular interaction between biotin and β-CD, representing a new affinity system for bioreceptor immobilization (**Figure 4**) [24].

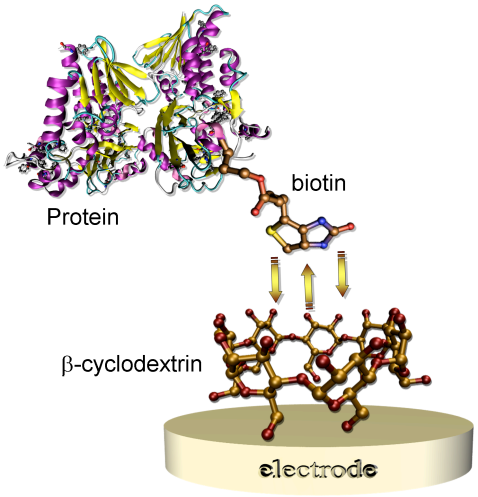

Figure 4. *Schematic representation of supramolecular interaction between biotin and β-CD.*

2.3 Evaluation of biotin–β-cyclodextrin inclusion complex

2.3.1 Characterization by ^{1}H NMR spectrometery

^{1}H NMR spectroscopy is a useful tool to study the kinetics of inclusion complexes with cyclodextrins [19,20]. ^{1}H NMR spectra were recorded at 300 MHz. All shifts for ^{1}H spectra were referenced to the residual solvent peak and are reported in ppm. The ^{1}H-NMR spectra were recorded with D_2O solutions of β-CD, biotin, and its mixtures of 1:0.2, 1:0.4, 1:0.6, 1:0.8, 1:1, and 1:1.2 ratio, respectively.

Due to the cyclic structure of β-CD, the hydrogen atoms of each glucopyranoside unit are orientated either to the exterior (H1, H2, H4) or the interior (H3, H5) of the cyclodextrin torus (**Figure 5A**). After formation of an inclusion complex, the chemical shifts of the protons

inside the torus are therefore mostly affected. **Figure 5B** shows the ^{1}H NMR spectra of pure β-CD (10 mmol.L^{-1}), pure biotin (saturated solution), and a 1:1 mixture of β-CD and biotin (10 mmol.L^{-1}), respectively. A zoom of the range of the protons of interest (H3 and H5) between δ= 4.0 and 3.7 ppm is presented **Figure 5C**. The obtained chemical shift variations of the β-CD protons are summarized in **Table 1**.

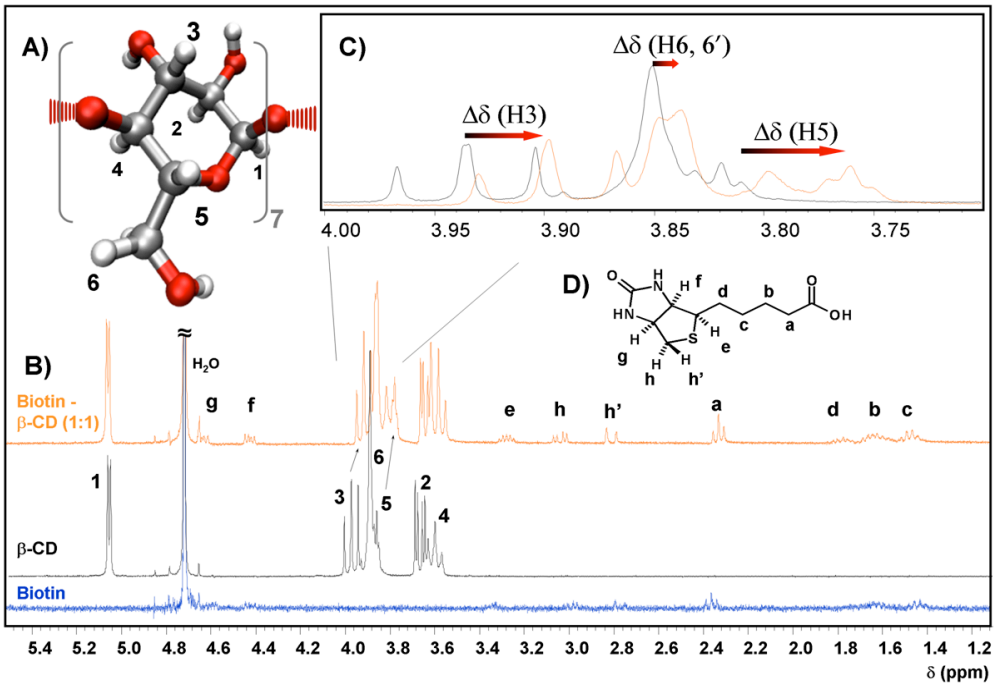

Figure 5. *A) Sketch of one β–cyclodextrin glucopyranoside unit. B) ^{1}H-NMR spectra of (blue curve) biotin in a saturated (~10^{-6} mol.L^{-1}) D$_2$O solution, (grey curve) β-CD (10 mmol.L^{-1}) in D$_2$O solution, and (orange curve) a 1:1 mixture of biotin and β-CD (both 10 mmol.L^{-1}) in D$_2$O solution. C) Zoom of the H3, H6 and H5 signal range between 4.0 ppm and 3.7 ppm. D) Biotin sketch.*

Table 1. *Spectroscopic data of the chemical shift of β -CD protons of "free" β -CD and of the 1:1 β -CD biotin complex.*

Proton	δ (ppm) free	δ (ppm) 1:1 complex	Δδ (ppm)
H1 (7H,d)	5.041	5.041	0.000
H3 (7H,t)	3.934	3.898	−0.036
H6 (14H, 2t overlapped)	3.851	3.837	−0.014
H5 (7H,dt)	3.819	3.777	−0.042
H2 (7H,dd)	3.622	3.616	-0.006
H4 (7H,t)	3.554	3.564	0.010

As expected, the H3 and H5 signals show the most pronounced shift to higher fields in the spectrum of the 1:1 mixture. It has to be noted that only differences of the chemical shifts

and no signal doubling could be observed. This indicates a fast exchange rate (at the NMR time scale) where just the average of the chemical shift of 'free' protons and the protons in the inclusion complex is observed. Only a separation of the individual H6-CH_2 proton signals is observed. This phenomenon can be assigned to the reduced rotation of this methylene group in presence of complexed biotin that leads to two distinguished peaks (H6 and H6', respectively). Due to some overlap of the H5 and H6 signals, the association constant was calculated by plotting the chemical shift changes of the β-CD H3 protons at varying biotin concentrations. The association constant ($K_{1:1}$) can be determined by second order non-linear curve fitting [21] of the experimental data using equation (1):

$$\Delta\delta_{obs} = \left\{ \frac{K_{1:1}(\Delta\delta_c C_{Biotin} - \Delta\delta_{obs} C_{\beta-CD})}{[\Delta\delta_c + K_{1:1}(\Delta\delta_c C_{Biotin} - \Delta\delta_{obs} C_{\beta-CD})]} \right\} \Delta\delta_c \qquad (1)$$

$\Delta\delta_{obs}$ is the measured chemical shift difference of the H3 signal for each β-CD/biotin ratio due to free β-CD, where $\Delta\delta_c$ is the chemical shift difference between β-CD protons in its free and bound state. C_{Biotin} and $C_{\beta\text{-}CD}$ are the concentrations of biotin and β-CD, respectively. The concentration of β-CD was kept constant (10 mmol.L^{-1}) while the biotin concentration increase from 0-12 mmol.L^{-1} by a incremental of 2 mmol.L^{-1} at each steps. **Figure 6** shows the fitted plot of the H3 chemical shift differences as function of the biotin concentration. Simple integration of selected biotin and β-CD proton signals already indicate a formation of a 1:1 complex since the biotin concentration could be increased by a factor of 10,000 in presence of β-CD.

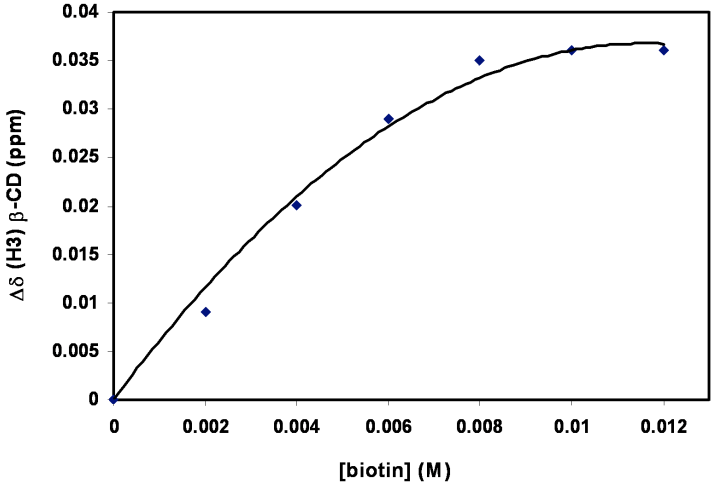

Figure 6. *Non-linear regression fitting of experimental data obtained by the chemical shift displacements of the β-CD-H3 protons at different biotin concentrations.*

To get more insight in the orientation of biotin inside the cyclodextrin cavity, proton-proton NOE spectra were recorded. Due to the high ratio (7:1) of the β-CD to biotin protons, the recorded 2D NOE or ROE spectra were not conclusive. Therefore, the nuclear Overhauser effect was examined by irradiating separately at each biotin proton frequency revealing its coupling with the closest β-CD proton. As expected, the H3 and H5 protons of β-CD showed the strongest ROE's, where the *h'* and *e* protons of biotin (**Figure 5D**) share medium ROE's with the H5 and H6 β-CD protons, *h* shows an effect with H5 and H3 protons, while proton *g* still shows a weak effect with the H3 β-CD protons. This summarized analysis of all obtained 1D spectra led conclude that the bicyclic part of biotin is slightly tilted in the β-CD cavity. The CH_2 groups *a-d* of biotin shows very weak interactions with H3 and H4 of β-CD indicating that the biotin alkyl chain is situated at the plane of the wider rim of β-CD. The urea NH section of biotin and the OH groups of β-CD certainly contribute to the formation and stability of the inclusion complex but cannot be investigated by NMR using water as solvent. Nevertheless, with the obtained data, an estimated structure of the biotin-β-CD complex can be proposed (**Figure 7**).

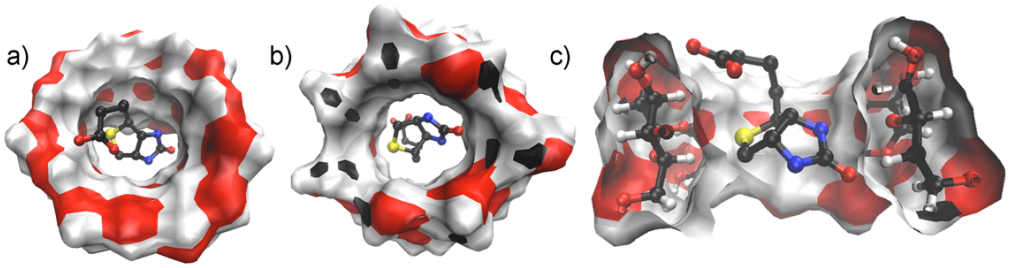

Figure 7. *Proposed structure of the biotin- β-CD complex as CPK (biotin) and CPK-surface representation (β-CD). a) Top view, b) bottom view, and c) side view of the cross section.*

The calculated association constant of 300 ± 12 $L.mol^{-1}$ is clearly below the association constant of the known affinity system β-CD / adamantine (K_a = 5.2 x 10^4 $L.mol^{-1}$) [6]. To evaluate the appropriateness of the biotin- β-CD inclusion complex for the immobilization of biological macromolecules, enzymatic biosensors were constructed using GOx and PPO as model enzymes (see **chapter 3**).

2.3.2 Characterization by Fluorescence microscopy

The biotin–β-CD inclusion complex was finally evaluated by fluorescence microscopy. In 1999, Cosnier *et al.* synthesized pyrrole biotin [22]. They used biotinylated glucose oxidase (GOx) and polyphenyl oxidase (PPO) as model enzymes and immobilize them onto the

electrogenerated biotinylated conducting polypyrrole film for the construction of an amperometric biosensor via avidin bridges. We used the same approach for the creation of biotinylated surface onto which β-CD modified biomolecules can be immobilized.

Gold microelectrodes (10 µm diameter) arrayed on a silicon chip were used for the fluorescence detection. A gold microarray electrode was modified with a polypyrrole biotin film generated by electropolymerization of pyrrole biotin (4 mmol.L^{-1}) in CH_3CN solution at 0.9 V (electrolysis: Q = 0.5 mC) to prevent the overoxidation of the polypyrrole skeleton and hence to preserve its conductivity (see **Chapter-3** for more details). The fluorescent streptavidin probe was immobilized by incubation of the modified electrode in a Streptavidin-R-PhycoErythrin (streptavidin-RPE) (5 µg.mL^{-1}). R-Phycoerythrin (RPE) is an intensely bright phycobiliprotein isolated from red algae with absorption maxima at approximately 496, 546 and 565 nm, and a fluorescence emission maximum of ~578 nm [23].

As expected, **Figure 8B** clearly shows the fluorescence of immobilized streptavidin fluoroprobe on biotin modified electrodes. In order to get an indirect proof of the effective insertion of polymerized biotins into β-CD, the microelectrodes modified by the biotinylated polypyrrole were incubated in a β-CD tagged GOx solution (0.5 mg.mL^{-1}) and then rinsed before incubation in the streptavidin fluoroprobe solution. If biotins are really inserted into the β-CD, these biotins cannot react with the fluorescent streptavidin. Moreover, the formation of a compact immobilized β-CD tagged GOx layer should block the access to the polymerized biotin groups, which are not inserted in β-CD cavities. Since there are no specific interactions between β-CD tagged proteins and avidin, no fluorescence of the microelectrodes is therefore to expect. Indeed, **Figure 8C** confirms the absence of fluorescent streptavidin and therefore, indirectly, the presence of an immobilized β-CD tagged GOx layer.

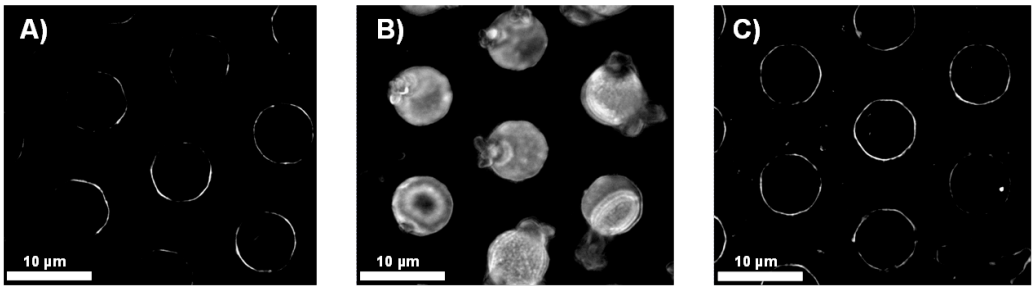

Figure 8. *Fluorescence microscopy images of a poly(pyrrole-biotin) film electrogenerated on microarray electrodes (A) before and (B) after incubation with a fluorescent streptavidin solution; (C) polypyrrole biotin films, electrogenerated on microarray electrodes after successive incubation in a β-CD tagged GOx solution and then a fluorescent streptavidin solution.*

2.4 Conclusion

The formation of stable supramolecular interactions between biotin and β-cyclodextrin was invesitgated. An association constant of 3 x 10^2 $L.mol^{-1}$ was determined by NMR analyses by mapping the high field shift differences of the β-cyclodextrin protons (H3) at different biotin concentrations. The host-guest complex was finally evaluated with fluorescence microscopy revealing biotin–β-CD interactions. This new affinity system presents a high potential for the development of new biosensors and biofuel cells [Results published in Langmuir, see Ref 24].

References

1. B. Prieto-Simon, M. Campas and J. L. Marty, Protein Pept. Lett., 2008, 15, 757–763.

2. P. C. Weber, D. H. Ohlendorf, J. J. Wendoloski and F. R. Salemme, Science, 1989, 243, 85–88.

3. J. Davis, A. Glidle, A. E. G. Cass, J. Zhang and J. M. Cooper, J. Am. Chem. Soc., 1999, 121, 4302–4303.

4. N.Haddour, S. Cosnier and C.Gondran, J. Am. Chem. Soc., **127** (2005) 5752-5753

5. J. Baur, M. Holzinger, C. Gondran and S. Cosnier, Electrochem. Comm., 2010, 12, 1287–1290.

6. Connors, K. A. Chem. Rev. 1997, 97, 1325–1358.

7. E. M. M. Del Valle, Process Biochem., 2004, 39, 1033–1046.

8. Le Goff. A, Gorgy. K, Holzinger. M, Haddad. R, Zimmermann. M, Cosnier. S. Chem. Eur. J. 2011, 17, 10216–10221.

9. R. Villalonga, C. Camacho, R. Cao, J. Hernandez and u. C. Matıas, Chem. Commun., 2007, 942–944.

10. D. Granadero, J. Bordello, M. J. Perez-Alvite, M. Novo and W. Al-Soufi, Int. J. Mol. Sci., 2010, 11, 173–188.

11. M. Holzinger, L. Bouffier, R. Villalonga and S. Cosnier, Biosens. Bioelectron., 2009, 24, 1128–1134.

12. Wilchek, M.; Bayer, E. Anal. Biochem.1988, 171, 1–32.

13. Molteni, R.; Robouch, P. European Union reference Laboratory for Feed Additives 2011, JRC.DG.D.6/CvH/RMO/ag/ARES(2011)341670, FAD-2010–0100-CRL/100012.

14. Ito, A.; Ooya, T.; Yui, N. J. Incl. Phenom. Macrocycl. Chem. 2007, 57, 233–236.

15. Kato, K.; Goto, R.; Katoh, K.; Shibakami, M. Biosci. Biotechnol. Biochem. 2005, 69, 646–648.

16. Ludden, M. J. W.; Li, X.; Greve, J.; Amerongen, A. v.; Escalante, M.; Subramaniam, V.; Reinhoudt, D. N.; Huskens, J. J. Am. Chem. Soc.2008, 130, 6964–6973.

17. Ludden, M. J. W.; Péter, M.; Reinhoudt, D. N.; Huskens, J. Small2006, 2, 1192–1202.

18. Raschke, T.; Max, H. In United States Patent; Publication, U. P., Ed.; Beiersdorf AG, Hamburg (DE): United States, 2002; Vol. US 6436414 B1.

19. Loftsson, T.; Brewster, M. E. J. Pharm. Sci. 1996, 85, 1017– 1025.

20. Schneider, H.-J.; Hacket, F.; Rüdiger, V.; Ikeda, H. Chem. Rev. 1998, 98, 1755–1786.

21. Loukas, Y. L. J. Pharm. Pharmacol. 1997, 49, 944–948.

22. S. Cosnier, M. Stoytcheva, A. Senillou, H. Perrot, R.P.M. Furriel, F.A. Leone, Anal Chem, 71 (17) (1999), pp. 3692–3697.

23. http://www.lifetechnologies.com/order/catalog/product/S866.

24. M. Holzinger, M. Singh, S. Cosnier, Langmuir 2012, 28, 12569.

Affinity-based amperometric biosensors

Chapter 3

3.1 Context

Affinity-based biosensing systems have become an important analytical tool for the detection and study of numerous biomolecules. The immobilization of biomolecules *via* affinity interactions has achieved wide acceptance in recent years in binding biological species to surfaces on a solid support at a predetermined site while minimizing cross-contamination. In particular, the electrogeneration of polymer films, bearing affinity partners, provided an easy control over the properties of the polymeric coating and was compatible with bulk manufacturing procedures. Moreover, the electropolymerization process allows the electrogeneration of polymers with precise spatial resolution over conductive surfaces, whatever their size and geometry. This approach represents an elegant tool for the functionalization of micro-electrochemical systems such as biochips and interdigitated ultra-microelectrodes [1].

Most of the electropolymerized films used for biomolecule immobilization are conducting polymers such as polyacetylene, polythiophene, polyaniline, polyindole and polypyrrole. Such configuration appeared to be very promising for the immobilization of biomolecules with full retention of their activity. Owing to their wide range of potential applications in energy storage, electrochromic devices, organic transistors, and non-linear optics, the use of electrogenerated polymers also offers a great promise for the electrochemical transduction of biological events. In particular, the electrical conductivity of polymers and their chemical functionalization have been exploited to provide an electrochemical signal reflecting a biomolecular recognition phenomenon. Moreover, the considerable flexibility in the available monomeric structures enables elegant modulation of polymer properties in terms of biomolecule retention or electrical wiring. Their low cost associated with their ease of production make electrogenerated polymer films very attractive for the design of electrochemical biosensors and biochips. The immobilization of biomolecules in or on electrogenerated polymer films has been used for development of bioanalytical devices [2-5].

In **chapter 2**, we discussed new biotin - β-CD affinity system and advantages of biotin as an anchor molecule. To evaluate the appropriateness of the biotin - β-CD inclusion complex for the immobilization of biological macromolecules onto the electrogenerated surfaces, in this chapter, we present the fabrication of amperometric enzymatic biosensors using glucose oxidase (GOx) and polyphenyl oxidase (PPO) as model enzymes.

3.2 Electropolymerization of pyrrole biotin

Diaz *et al.* [6] demonstrated that the electro-oxidation of pyrrole in acetonitrile containing an appropriate electrolyte led to the formation of "polypyrrole" an electrically conducting polymer. The electro-oxidation of monomeric pyrrole (**1**) at an electrode surface gives rise to a delocalized radical cation (**2**). They have suggested for the polymerization of pyrrole that monomers dimerize after oxidation at the electrode, and that protons are eliminated from the doubly charged dimer (**3**), forming the neutral species (**Scheme I**). Since the dimer (**4**) has lower oxidation potential (E_{pa} = 0.6 V) than the monomer (E_{pa} = 1.2 V), it is more easily oxidizable and immediately reoxidized to the cation (**5**). Chain growth is accompanied by the addition of new cations of the monomeric pyrrole to the already charged oligomers (dimers). This in turn is followed by another proton elimination and the oxidation of the propagated oligomeric unit to a cation.

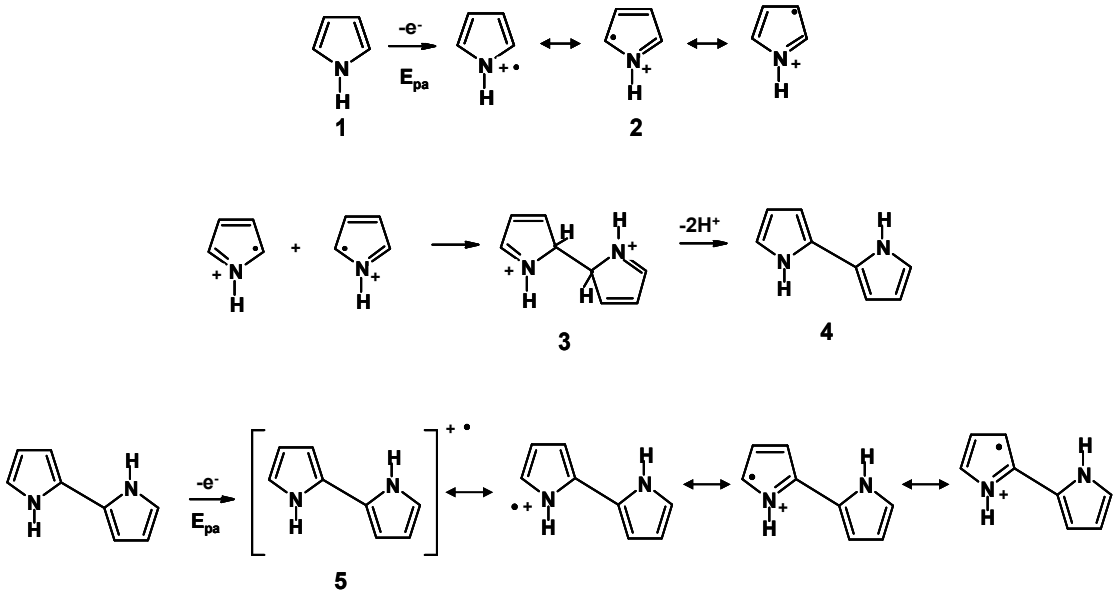

Scheme I. *Proposed mechanism scheme for the eletropolymerization of pyrrole [6].*

Among the various electrogenerated films used for the elaboration of biosensors and immunosensors, polypyrrole films are the most employed polymers because of their biocompatibility (polymerization at physiological conditions) and the ease of immobilization of various biologically active compounds [7,8]. In addition, biosensing materials must be electroactive at physiological pH. Polypyrrole offers the advantages over polyaniline and polythiophene, since it can easily be deposited at neutral pH using aqueous solutions of pyrrole monomers. In terms of biotin modification of transducer surfaces, the electropolymerization of biotin labelled monomers like thiophenes [9], phenols [10], or pyrroles [11] represents a fast and controllable way to modify conductive transducers with thin biotin coatings. Pyrrole biotin, as discussed in the last chapter, can be used to immobilize a wide range of biomolecules to develop sensitive biosensors (**Figure 1**).

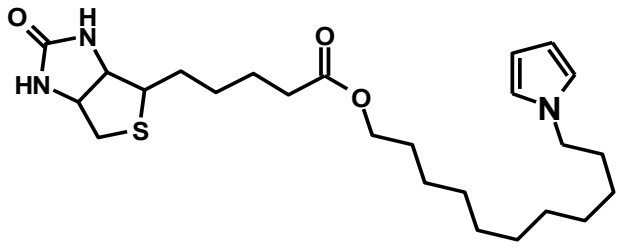

Figure 1. *Chemical structure of pyrrole-biotin.*

For the amperometric transduction, a Pt electrode (Φ = 5 mm) was used for the electrogeneration of polypyrrole biotin film. A poly(pyrrole-biotin) film was generated by electropolymerization of pyrrole biotin (4 $mmol.L^{-1}$) in CH_3CN solution at 0.9 V (electrolysis: Q = 0.5 mC). Electropolymerization of pyrrole-biotin was accomplished by controlled-potential oxidation at 0.9 V to prevent the over-oxidation of the polypyrrole skeleton and hence to preserve its conductivity. In this context, the anchoring of a protein or an oligonucleotide monolayer can thus be occurred *via* avidin bridges or host-guest interactions between electrogenerated biotin films and biotinylated or β-CD modified enzymes, antibodies, bacteria or oligonucleotides respectively.

3.2.1 Immobilization of β-CD Tagged GOx on Biotin Modified Electrodes

The possibility to immobilize biological receptor units on transducer surfaces *via* the supramolecular host–guest interaction between biotin and β-CD was then investigated using β-CD tagged glucose oxidase and Pt electrodes modified by poly(pyrrole-biotin) film. As well known, GOx catalyzes the oxidation of glucose to gluconolactone by producing hydrogen

peroxide out of oxygen. The latter is due to the reduction of oxygen that allows the regeneration of the oxidized state of the active site of GOx. H_2O_2 is then oxidized at the Pt-electrode at 0.6 V *vs* SCE, leading to current increase which is directly related to the glucose concentration. The biosensor was constructed by initial electrogeneration of a poly(pyrrole-biotin) film followed by incubation of this modified electrode in a buffer solution containing β-CD tagged GOx (0.5 $mg.mL^{-1}$) for 15 min. Such freshly prepared enzyme electrodes were rinsed and then used for the amperometric measurements. **Figure 2a** presents the resulting Michaelis–Menten-type calibration curve obtained by monitoring the amperometric response at varying glucose concentrations.

The sensitivity of the bioelectrode was determined by the slope of the linear part of the curve. The sensitivity of 0.98 $mA.L.mol^{-1}.cm^{-2}$, together with a maximum current density J_{max} of 23.01 $\mu A.cm^{-2}$, and the apparent Michaelis–Menten constant K_M^{app}= 15.4 × 10^{-3} $mol.L^{-1}$ is in good correlation with previous results recorded for a poly(adamantane-pyrrole) electrode modified by the anchoring of glucose oxidase modified with β-cyclodextrin [12]. It has to be noted that all amperometric measurements of the biosensor performances were conducted under magnetic stirring. During the whole experiment, no decomplexation of the bioreceptor unit has been observed, which confirms the sufficient stability of the biotin–β-CD complex for at least several hours.

The efficiency of this new affinity system to immobilize bioreceptor units was further evaluated by comparison with the well-known bridging system biotinylated protein – avidin–biotinylated surface. This control experiment was performed under identical conditions where the poly(pyrrole-biotin) electrode was first incubated in a streptavidin (0.5 $mg.mL^{-1}$) buffer solution (phosphate, 0.1 $mol.L^{-1}$, pH 7.0) and second, after rinsing, in a buffer solution containing biotin tagged GOx (0.5 $mg.mL^{-1}$). The measured sensitivity of this setup is 29 $\mu A.L.mol^{-1}.cm^{-2}$ with J_{max}= 3.62 $\mu A.cm^{-2}$ and K_M^{app}= 35.7 × 10^{-3} $mol.L^{-1}$ (**Figure 2b**). The performances of the sensor setup based on the biotin–β-CD inclusion system are clearly higher than the corresponding immobilization technique using biotin tagged biomolecules on biotinylated polymers *via* avidin bridges. This particularly demonstrates the detrimental effect of the intermediate streptavidin layer. The latter may prevent optimal diffusion of the substrate to the active site of GOx and the diffusion of H_2O_2 to the underlying platinum surface leading thus to clearly reduced performances. Furthermore, the biotin–β-CD setup provides a larger linear range and a more sensitive detection limit.

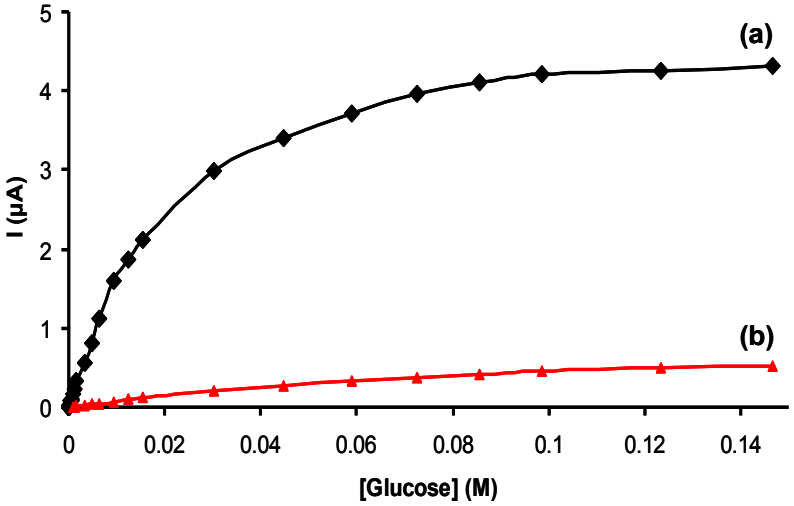

Figure 2. *Calibration curve for glucose obtained at platinum electrodes modified by poly(pyrrole-biotin) film and incubated with (a) β-CD tagged GOx or (b) streptavidin and then biotin tagged GOx. Applied potential: 0.6 V vs SCE in 0.1 mol.L^{-1}phosphate buffer (pH = 7.0).*

3.3 Electropolymerization of pyrene β-CD

Pyrene is a polyaromatic hydrocarbon, which can be electropolymerized to generate conducting polymer films. In 1983, Bargon *et al.* found polypyrene-ClO_4 film to be conducting and also proposed the mechanism for the formation of polypyrene [13]. Molecular orbital calculation reveals that the positions of highest unpaired electron density occur at the equivalent 1-, 3-, 6-, and 8-positions (**Figure 3**). The highest unpaired electron densities also identify these positions as the reactive sites, suggesting that the monomer linkages in an idealized polymer structure do occur in these same positions.

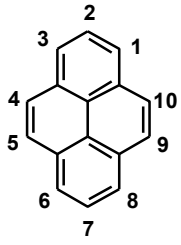

Figure 3. *Chemical structure of pyrene.*

The first step in the electropolymerization reaction sequence that is dimerization produces 1, 1'-bipyrene (**2**) (**Scheme II**). As with the monomer pyrene radical cation, the positions of the highest unpaired electron density in the 1, 1'-dimer occur at the 1-, 3-, 6-, and

8-positions [14,15] for the 1, 1'-bipyrene radical cation (**3**). Thus, when 1, 1'-bipyrene (**2**) is electro-oxidized to its radical cation, a monomer radical cation will attack the 1, 1'-dimer radical cation (**3**) at its unblocked 3-, 6-, or 8-positions, to produce trimer (**4**, **5** or **6**).

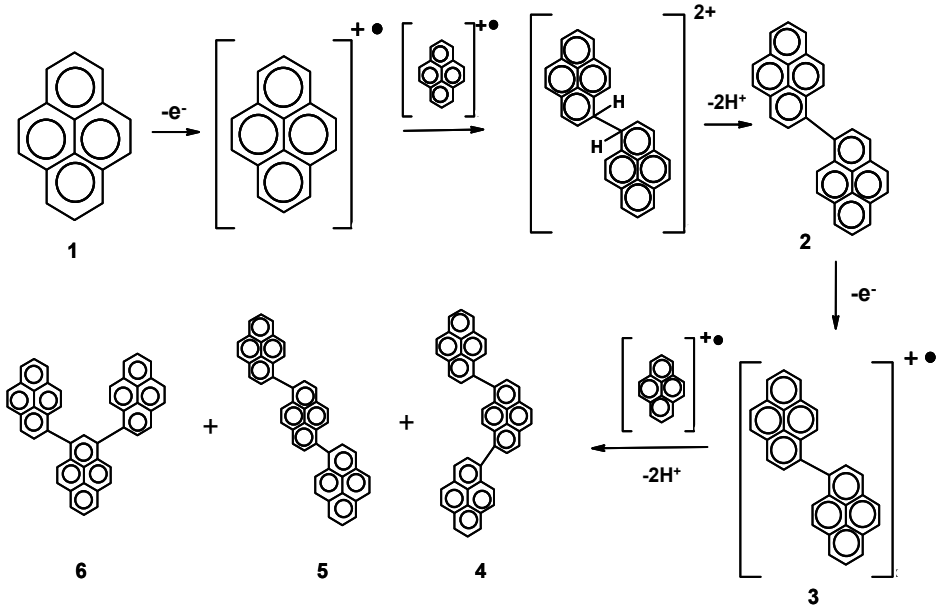

Scheme II. *Proposed mechanism scheme for the eletropolymerization of pyrene [12].*

The electrochemical behaviour of polypyrene is relative similar to polypyrrole but has several disadvantages due to its reduced permeability and its loss of electroactivity with increasing film thicknesses as well as its ability to be polymerized in an aqueous medium [16]. Nevertheless, pyrene derivatives and its electrogenerated films also have the advantage to form stable π-stacking interactions with carbonaceous species and are chemically stable. We synthesized pyrene-β-CD (**Section IV**), which allows immobilization of a wide variety of biomolecules having biotin or adamantane as functional group (**Figure 4**).

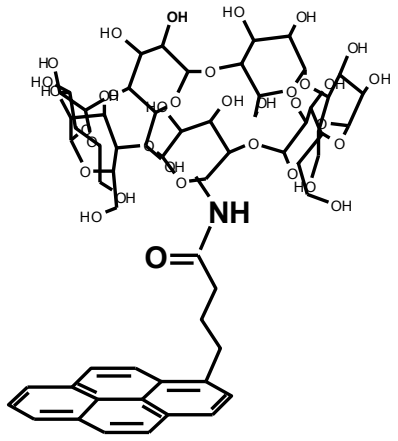

Figure 4. *Chemical structure of pyrene- β-CD.*

Pyrene β-CD was electropolymerized on the electrodes in 0.1 $mol.L^{-1}$ phosphate buffer solution pH 7.0 containing 5 $mmol.L^{-1}$ pyrene-β-CD by chronoamperometry (1.3 V, 0.5 mC). Electropolymerization of pyrene-β-CD was accomplished by controlled-potential oxidation at 1.3 V to prevent the over-oxidation of the polypyrene skeleton and hence to preserve its conductivity [17]. β-CD groups create a hydrophilic environment through the film, enabling better diffusion of the bio-macromolecules.

3.3.1 Immobilisation of Biotin Tagged GOx on β-CD Modified Electrodes

To demonstrate the appropriateness of this new affinity system, further control experiments were performed. Since one advantage of this inclusion complex is the possibility to immobilize easily producible and even commercially available biotin tagged bioreceptors, β-CD modified electrodes were formed. The enzymatic biosensor was constructed using biotinylated GOx and PPO, respectively.

For the immobilization of GOx, pyrene-β-CD (5 $mmol.L^{-1}$) was electropolymerized on the Pt electrodes (Φ = 5 mm) in 0.1 $mol.L^{-1}$ phosphate buffer by chronoamperometry (1.3 V, 0.5 mC). Such polypyrene–β-CD modified electrodes were incubated in biotin-modified GOx (0.5 $mg.mL^{-1}$) phosphate buffer solution (0.1 $mol.L^{-1}$) for 20 min at 4 °C. After rinsing, the analytical performance of the biosensors for glucose determination was examined.

Figure 5a presents the resulting calibration curve after monitoring the amperometric response of the electrode at varying glucose concentrations. The sensitivity of the electrode was 0.24 $mA.L.mol^{-1}.cm^{-2}$ and J_{max} was 21.1 $\mu A.cm^{-2}$. The apparent Michaelis–Menten constant K_M^{app}, was equal to 29.4 × 10^{-3} $mol.L^{-1}$. The inversed set-up also clearly showed better performances than the biotin–avidin system, even with the less permeable polypyrene films. Considering the high versatility of inclusion complexes with β-CD [18], the probability that hydrophobic residues of appropriate size of the GOx protein shell (e.g., the benzene ring of phenylalanine or the indole group of tryptophan) can interfere with the biotin groups was evaluated by choosing the same sensor setup but with unmodified enzymes. **Figure 5b** shows the obtained results for this configuration where a clear nonspecific binding of unmodified GOx can be observed. Nevertheless, the sensor performance with sensitivity and maximum current density of 92 $\mu A.L.mol^{-1}.cm^{-2}$and J_{max}= 9.4 $\mu A.cm^{-2}$ was still clearly below (~40%), the values obtained using the biotinylated enzyme. It can therefore be considered that biotin is a preferred guest for an inclusion complex than the hydrophobic residues of the protein shells.

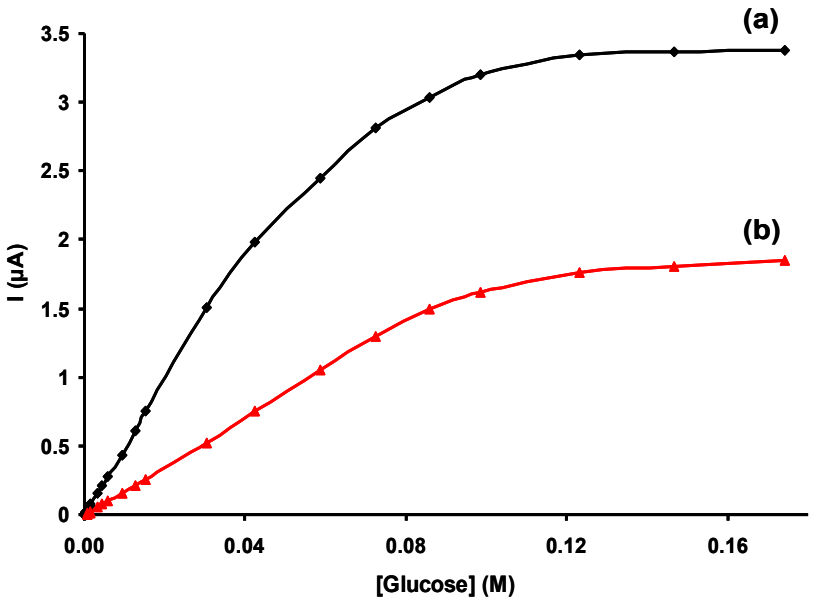

Figure 5. *Calibration curves for glucose detection obtained using poly(pyrene-β-CD) modified electrodes after incubation in buffer solution containing (a) GOx-biotin and (b) unmodified GOx. Applied potential: 0.6 V vs SCE in 0.1 mol.L^{-1}phosphate buffer (pH = 7.0).*

3.3.2 Immobilisation of Biotin Tagged PPO on β-CD Modified Electrodes.

To further confirm the successful anchoring of biotinylated proteins on β-CD modified surfaces and to evaluate the phenomenon of unspecific binding, PPO was used as a further model protein. In this context, 5 µL of biotin-modified PPO (0.3 mg.mL^{-1}) was deposited on poly(pyrene–β-CD) modified glassy carbon electrode surface (Ø = 3 mm) and remained for 20 min at 4°C. After rinsing, the analytical performance of the biosensors for catechol determination was examined in stirred 0.1 mol.L^{-1} phosphate buffer. Since PPO catalyzes the oxidation of phenols and o-diphenols into o-quinone, the amperometric biosensor was potentiostated at the o-quinone reduction potential, namely –0.2 V *vs* SCE.

Figure 6a shows the bioelectrode response as a function of catechol concentration reflecting thus the efficient anchoring of biotinylated PPO. The resulting sensitivity and maximum current density values at saturating catechol conditions are 0.57 mA.L.mol^{-1}.cm^{-2}and 22.7 µA.cm^{-2}, respectively. Again, a blank test was performed to examine non-specific binding via inclusion of the hydrophobic residues (phenyl, indole of phenylalanine or tryptophan, respectively) of the PPO protein shell. The β-CD modified electrode was therefore incubated in unmodified PPO solution followed by measuring the amperometric response toward catechol after rinsing. The obtained values for the sensitivity (54 µA.L.mol^{-1}.cm^{-2}) and J_{max}(1.0

μA.cm^{-2}) were noticeably below the performances of the sensor with biotinylated PPO and represents less than 10% of nonspecific binding (**Figure 6b**). Moreover, the comparison of J_{max} value (51.29 μA.cm^{-2}) reported for the immobilization of five compact layers of biotinylated PPO onto a biotinylated polypyrrole film via avidin bridges with that (22.7 μA.cm^{-2}) recorded with one layer of biotinylated PPO anchored onto poly(pyrene–β-CD) clearly illustrated the advantage of the β-CD-biotin system [19].

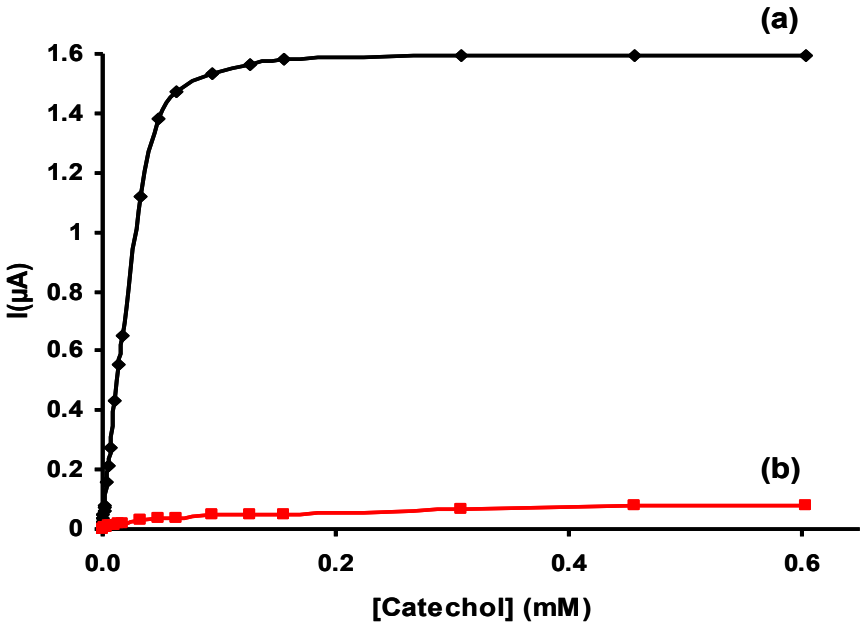

Figure 6. *Calibration curve for catechol detection obtained using poly(pyrene-β-CD) modified electrodes after incubation in buffer solution containing (a) PPO-biotin and (b) unmodified PPO. Applied potential: –0.2 V vs SCE in 0.1 mol.L^{-1} phosphate buffer (pH = 7.0).*

The visible different behavior of the two enzymes to interact with β-CD modified surfaces can be explained by the presence of the phenylalanine and tryptophan in the protein structure. **Figure 7 A,B** represents the ribbon structure of GOx (PDB-ID: 1PGE) and PPO (PDB ID: 3I6D), respectively, where phenylalanine and tryptophan are highlighted in dark gray. The protein structure of GOx contains much more phenylalanine and tryptophan units than PPO and therefore has a statistically higher probability to form non-specific inclusion complexes with β-CD coated surfaces.

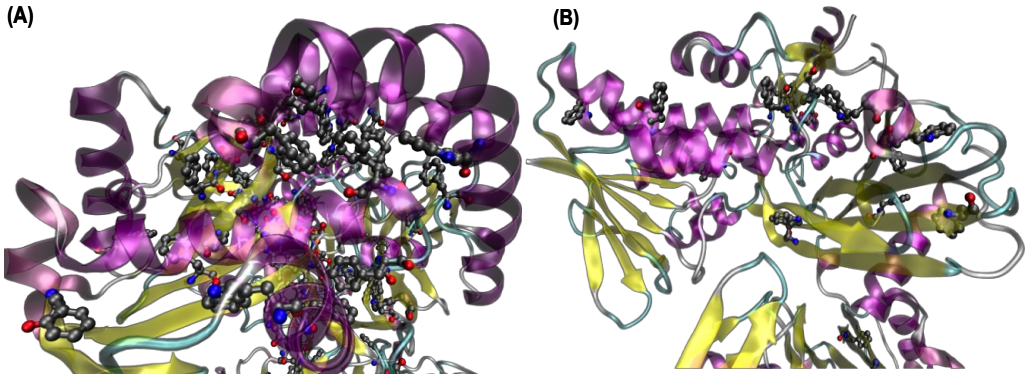

Figure 7. *Schematic representation of (A) GOx and (B) PPO highlighting the phenylalanine and tryptophan units of the protein structure in dark gray.*

3.4 Conclusion

The inclusion of biotin inside the β-CD cavity was studied and evaluated as a further alternative for biomolecule immobilization. By using biotin-modified surfaces, a clear advantage of this supramolecular interaction was demonstrated compared to the biotin–avidin–biotin bridging system. The performances could be increased by almost 1 order of magnitude using the β-CD- biotin system. Moreover, this immobilization approach can be indifferently used with biotin labeled bioreceptor molecules on β-CD modified transducers or with β-CD labeled biomolecules on biotin modified transducers. However, the versatility of β-CD to form inclusion complexes can enhance non-specific binding of phenylalanine and tryptosan-rich proteins, which is the case for GOx. Against this, non-specific binding is negligible for PPO, which contains little PHE and TRP units. The immobilization of biotin labeled bioreceptor molecules on β-CD modified transducers is therefore not appropriate for any types of proteins. Nonetheless, it is thus expected that this immobilization method will be useful for the development of biosensors and biofuel cells [Results published in Langmuir, see Ref 20].

References

1. P.-C. Nien, M.-C. Huang, F.-Y. Chang and K.-C. Ho, Electroanalysis, 2008, 20, 635–642.

2. Trojanowicz M, Krawczynski V, Krawcyk T (1995) MikrochimActa 121:167–181

3. Schuhmann W (1995) MikrochimActa 121:1-29

4. Cosnier S (1999) BiosensBioelectron 14:443–456

5. S. Cosnier, M. Holzinger; Chem Soc. Reviews, 40 (2011) 2146-2156.

6. A. F. Diaz, K . K. Kanazawa and G. P. Gardinij. Chern. Soc. Chem. Cornrnun. 635, (1979).

7. SerradillaRazola S, Lopez Ruiz B, Mora Diez N, Mark Jr HB, Kauffmann J-M (2002) BiosensBioelectron 17:921–928

8. Llaudet E, Botting NP, Crayston JA, Dale N (2003) BiosensBioelectron 18:43–52

9. K. G. Chittibabu, M. Kamath, J.-O. Lim, K. A. Marx, J. Kumar, S. K. Tripathy, L. A. Samuelson and D. L. Kaplan, MRS OnlineProc. Libr., 1993, 330, 185.

10. J. Mack, D. Leipert, A. Badia, W. Knoll and G. Jung, Adv. Mater., 1999, 11, 809–814.

11. S. Cosnier, B. Galland, C. Gondran and A. L. Pellec, Electroanalysis, 1998, 10, 808–813.

12. Holzinger, M.; Bouffier, L.; Villalonga, R.; Cosnier, S. Biosens. Bioelectron. 2009, 24, 1128–1134.

13. J .Bargons, .Mohmand and R. J. Waltman. IBM J. Res. Dev. 27, 330 (1983).

14. J . T. Cooper and W. F. Forbesc. an. J. Chern. 46, 1158 (1968).

15. J . T. Cooper and J. Chern. 48, 1996 (1970)

16. Haddad, R.; Holzinger, M.; Villalonga, R.; Neumann, A.; Roots, J.; Maaref, A.; Cosnier, S. Carbon 2011, 49, 2571–2578.

17. R. Haddad, M. Holzinger, A. Maaref, S. Cosnier, ElectrochimActa, 55 (27) (2010), pp. 7800–7803

18. Ogoshi, T.; Harada, A. Sensors2008, 8, 4961–4982.

19. Mousty, C.; Bergamasco, J.-L.; Wessel, R.; Perrot, H.; Cosnier, S. Anal. Chem. 2001, 73, 2890–2897.

20. M. Holzinger, M. Singh, S. Cosnier, Langmuir 2012, 28, 12569.

Affinity-based optical DNA sensor

Chapter 4

4.1 Context

An optical nucleic acid biosensor consists of specific nucleic acid (probe) and an optical transducer, which serves to translate the binding of a target biomolecule to the probe into an output signal. SPR biosensors represent the most advanced and mature label-free optical biosensor technology. The ability to measure biomolecular interactions directly, in real time and without the use of dyes or labels makes SPR biosensors a powerful tool for the investigation of kinetic properties of biomolecular interactions [1]. Typical DNA samples contain attomolar or femtomolar concentrations, which are well below the nanomolar detection limit of classical SPR setups. In order to increase the sensitivity of SPR, signal amplification is constantly under intensive research.

The additional use of nano-species such as metal nanoparticles, particularly gold nanoparticles (Au-NPs) or semi-conductors, namely quantum dots (QD) results in tremendous SPR signal increases and lead to enhanced sensitivities and improved detection limits [2]. QDs have the capabilities to interact with propagating surface plasmons (SP), excite the later and vice versa to emit light that can be converted to propagating SP on silver nanowires [3]. The beneficial combination of near infrared QDs and gold surfaces for drastic signal enhancement in a SPRi biosensor setup was shown for the first time by Malic *et al.* [4]. The authors attributed the signal enhancement to SP-QD energy transfer phenomenon. Au-NPs have also great advantages in bioanalytical devices since they can act as efficient mediators in enzymatic redox processes and as signal amplifying transduction element [5]. In this context, biofunctionalized Au-NPs were used as label for high sensitive detection of carcinoembryonic antigens using the SPRi technique [6].

SPR signal enhancement by employing Au-NPs is mainly caused by LSPR (localised SPR)-SPR coupling effect and size/mass-material properties associated with Au-NPs. Among

these factors, the coupling effect has been expected to play a dominant role. This comes from the fact that within the optical excitation the collective oscillation of electrons leads not only to a pile-up of charge at the surface of a metal film but also to a localised Plasmon in a particle. The metal film provides an image field for the LSPR, and the interaction between these two fields cause both SPR wavelengths associated with Au-NPs and the film to shift significantly [7].

QDs have proven to be very effective donor fluorophores in biological applications [8,9]. Conversely, when brought in close proximity to dyes, gold nanoparticles (Au-NPs) allow effective fluorescence quenching over a broad range of wavelengths [10,11]. This suggests that QDs and Au-NPs could provide excellent donor-acceptor pairs. The combination of Au-NPs and QDs in biosensor applications is mostly based on the quenching of QD fluorescence by Au-NPs via Förster (Fluorescence) Resonance Energy Transfer (FRET) [12] when both nano-objects are in close contact. QD fluorescence is reestablished after the bio-recognition event of complementary single strands DNA (ssDNA) releasing the Au-NP and leads to a quantifiable optical signal [13,14]. At right distances between QDs and Au-NP, Au-NP act as optical antennas increasing the excitation rates of QDs and therefore to enhanced photoluminescence [15]. Based on the comprehensive studies of Maye *et al.* at single molecule scale, we aimed in this chapter to transfer this phenomenon to SPRi based biosensor applications.

SPR imaging (SPRi) has proven to be a versatile tool for the real-time study of genomic and proteomic interactions and kinetics. In contrast to classical wavelength or scanning angle SPR systems, SPRi provides visualization of the multiple interactions simultaneously in real time thanks to the integration of a charge-couple device (CCD) camera with the associated sensogram. In contrast to the other endpoint measurement systems, the use of SPRi allows detailed kinetic analysis to elucidate analyte behavior further, as well as to differentiate better between specific and non-specific adsorptions.

In this chapter, Au-NPs were evaluated as further SPRi signal amplifier together with QDs for DNA-based biosensor. β-cyclodextrin (β-CD) functionalized gold nanoparticles (Au-NP) were immobilized on an electrogenerated poly(pyrrole-biotin) film *via* supramolecular host-guest interactions and served as cross-linker for the immobilization of a 5' biotin ssDNA sequence from Legionella pneumophila as model bioreceptor unit. For this initial concept validation, we used a 5' Biotin modified target ssDNA onto which near-infrared streptavidin tagged CdSe quantum dots (QD) 15-20 nm with an emission of 800 nm were attached as further SPR signal amplifier after hybridization of the target and receptor sequences.

4.2 SPRi Instrumentation

SPRi detection of biomolecular binding interactions was performed using the SPRi Lab apparatus equipped with an 800 nm LED source, CCD camera, and a flow cell (GenOptics, France), placed in a Memmert Peltier-cooled incubator (Rose Scientific, Canada) for temperature control [16]. The entire biochip surface was imaged during the angular scan, while for each experiment ten spots were selected for the monitoring of the binding interactions with the probes and each experiment was repeated at least three times. The reflected intensity (%R) was plotted as a function of time showing the kinetics of the binding events that take place at the surface of the chip. DNA hybridization experiments were carried at 37 °C with an injection volume of 450 µL. A baseline signal was first obtained for the hybridization buffer, followed by the hybridization signal for the targets. The corresponding 5' biotin ssDNA target 1 $nmol.L^{-1}$ in hybridization buffer solution was allowed to hybridize with the receptor unit under constant flow of a closed circuit. Finally, a solution of streptavidin tagged QDs 1 $nmol.L^{-1}$ in MQ water was injected in the cell under continuous monitoring of the reflectivity change. The difference in the reflected intensity (Δ%R) was computed by taking the difference between the initial and final buffer signals.

4.3 Gold surface chemistry

The Gold-coated slides were cleaned with UV/ozone for 20 min, rinsed thoroughly with MQ water, and treated with piranha solution for further 5 min. After rinsing with MQ water, the slides were dried under a nitrogen stream.

Electropolymerizations were performed, in a conventional three-electrode cell, containing 0.1 $mol.L^{-1}$ $LiClO_4$ in acetonitrile as electrolyte solution with EZstat PRO 100 (NuVant Systems, Inc. Crown Point, Indiana) using EZware software. An Ag/Ag^+ ($AgNO_3$ (10 $mmol.L^{-1}$) in CH_3CN) electrode was used as a reference electrode and a Pt wire, placed in separate compartment containing organic electrolyte served as counter electrode. The gold sensor surfaces were then functionalized by electropolymerization of the pyrrole-biotin monomer [17] (2 $mmol.L^{-1}$ in CH_3CN + 0.1 $mol.L^{-1}$ $LiClO_4$) applying five cyclic voltammetric scans between 0 V and 0.95 V. The modified gold surface was rinsed with water and dried with nitrogen stream.

These modified gold surfaces were coated with β-CD Au-NPs [18], (0.5 $mg.mL^{-1}$) *via* supramolecular host guest interactions between biotin and β-CD [19] by incubation of the

biotinylated surfaces in a β-CD Au-NPs (20µL, 0.5 mg.mL^{-1} in MQ water) containing solution. As reference experiment, streptavidin (20µL, 0.2 mg.mL^{-1} inMQ water) was used as cross linker. On each prepared surface, 20 µl of a 1 µM 4X SSPE buffer solution containing 10T spacer 5' biotin ssDNA (5' biotin TTTTTTTTTT CA GGT CGC CCC TTC GCC GCC 3') was deposited and remained for 25 min before rinsing with SSPE buffer solution. For the hybridization target DNA (5' biotin GGC GGC GAA GGG GCG ACC TGA AAA AAAAAA- 3') was injected followed with SA-QDs injection.

4.4 Scanning electron microscopy imaging

QD–dsDNA-AuNPs assemblies were examined by field emission scanning electron microscopy (SEM). In the SEM image (**Figure 1B**), the QDs assemblies can be observed as lighter particles when compared to the bare gold surface (**Figure 1A**).

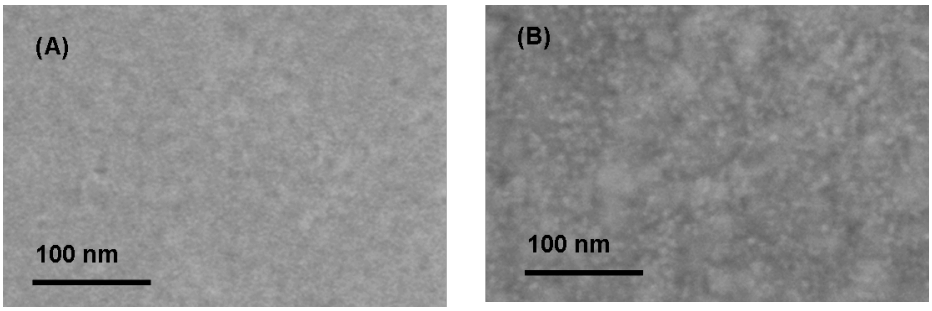

Figure 1. *SEM images of (A) unmodified gold surface and (B) gold surface modified with AuNPs-dsDNA-QD assemblies.*

4.5 DNA hybridization and signal amplification

In order to investigate the synergic effect of combining Au-NPs and QDs, biotinylated ssDNA with defined sequences and lengths (~10 nm) as receptor and target unit was used. For the control experiment using streptavidin as cross-linker to immobilize the receptor ssDNA, after injection of 1 nmol.L^{-1} of target ssDNA solution, a reflectivity change of 0.3 ± 0.05% could be observed (**Figure 2b**, inset, blue line). The subsequent labelling step using streptavidin modified QDs led to a clear signal amplification giving a reflectivity change of ΔR = 2.94 ± 0.2%. In case of β –CD, Au-NPs as linking layer for the receptor unit, the hybridization event with the biotinylated complementary ssDNA led a reflectivity change of 0.5 ± 0.03% which is similar to the streptavidin set-up (**Figure 2a**, inset, red line). After injection of the streptavidin QDs, a clear increase of the reflective change up to 16.92 ± 0.3% corresponding to an eight-fold signal amplification as compared to the streptavidin configuration was observed.

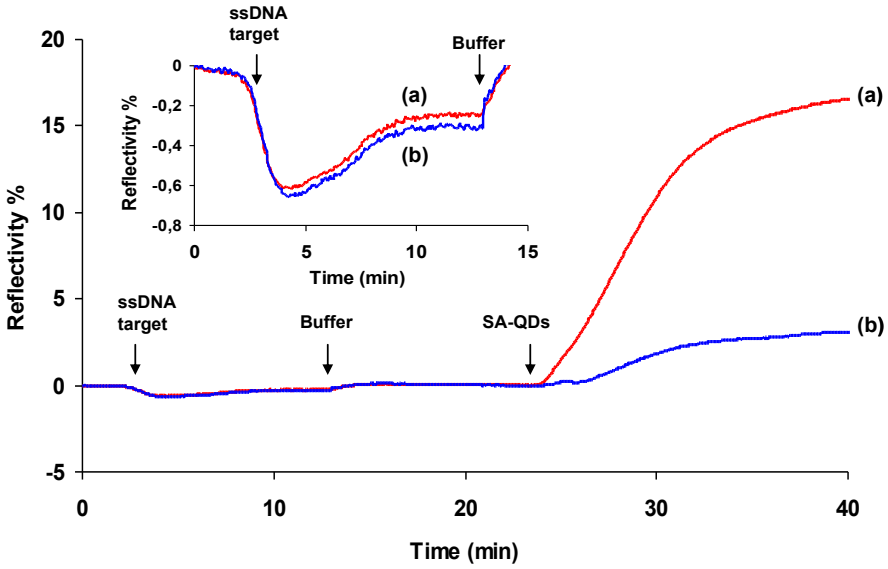

Figure 2. *Plot representation of the SPRi kinetic signal after addition of SA-QDs to the polypyrrole biotin surface, modified with β-CD Au-NPs (a) and streptavidin (b), after immobilization of the biotinylated receptor ssDNA and hybridization with the biotinylated target ssDNA. Inset: Zoom of the SPRi kinetic signal of the hybridization event of receptor and complementary target ssDNA on β-CD Au-NPs (a) and streptavidin (b) modified polypyrrole biotin surfaces.*

The signal enhancement in the case of AuNPs-DNA hybrid-SA-QDs can be justified with the antenna effect. Usually, FRET allows the detection of molecule-molecule interactions in the nanometer range. A donor fluorophore, initially in its excited state, may transfer energy to an acceptor fluorophore through non-radiative dipole-dipole interaction in the range of 10 nm scale. The efficiency of energy transfer strongly depends on the distance between the donor and acceptor molecules. The sensitivity to distance demonstrates $1/D^6$ of fluorescence energy transfer change [20]. Here, D stands for the distance between two fluorescence materials.

The interparticle distance D is estimated to be the length of the DNA (10.2 nm, 0.34 nm per base pair) plus the thickness of polymer and protein coating surrounding the QDs (5-7 nm). For an interparticle distance of 15-20 nm (D > 10 nm), quenching of the QD fluorescence *via* energy transfer with the β-CD AuNP is negligible [21,22], hence the β-CD AuNPs acts as an optical antenna by increasing the QDs excitation rate and hence enhances the SPR signal. In case of streptavidin, no change in the intensity was observed due to the absence of nanoparticles to modulate the optical properties of QDs (**Figure 3**).

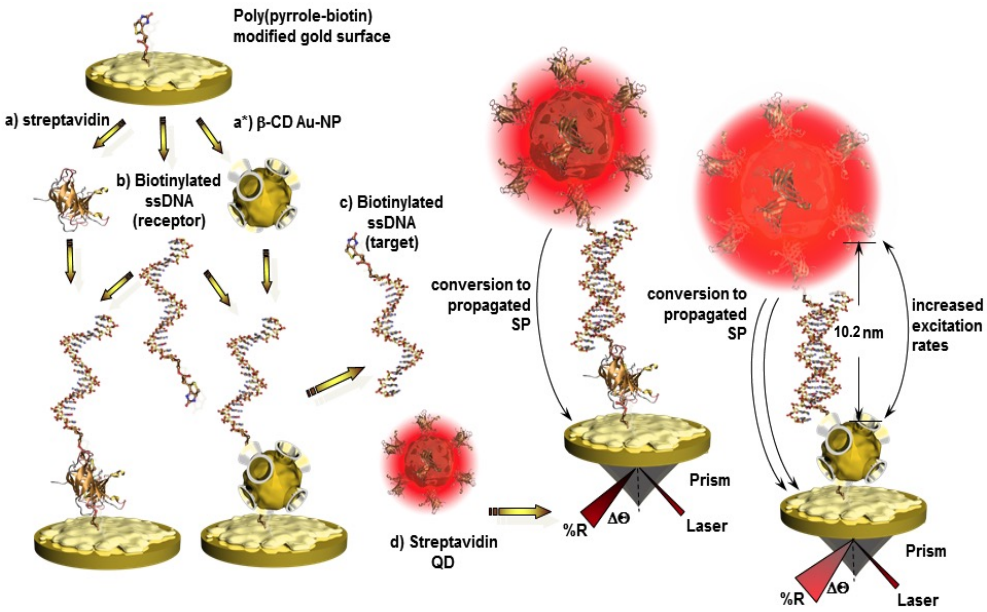

Figure 3. *Recapitulative schematic representation of the used set-ups. Immobilization of a) streptavidin and a*) β-CD Au-NP on poly(pyrrole-biotin) modified gold surfaces. b) Immobilization of the biotinylated ssDNA receptor unit. c) Hybridization with the biotinylated ssDNA target. d) Labelling with streptavidin modified QDs.*

We also measured SPR signal, where the β-CD gold nanoparticles were directly linked to the SA-QDs without DNA linker. For this construct, the gap between the emitter (QDs) and the quencher (Au-NPs) is 5-7 nm (D< 10 nm) and quenching of the QD fluorescence via energy transfer with the Au-NP was observed (**Figure 4**). The reflectivity change was 1.5 ± 0.23%, which is eight times lower than in the presence of DNA linker. This result supports the non-radiative transfer of energy within SA-QDs and β-CDAu-NPs.

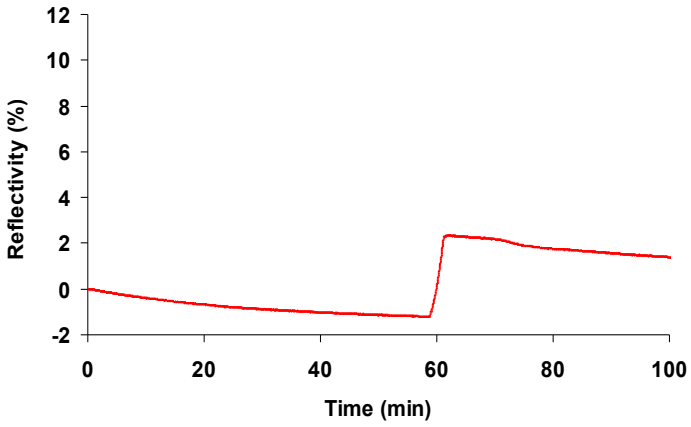

Figure 4. *Plot representation of the SPRi kinetic signal after addition of SA-QDs to the polypyrrole biotin surface, modified with β-CD Au-NPs.*

4.6 Conclusion

β-CD modified Au-NPs were successfully applied as an optical antenna for additional SPRi signal amplification using QD labels. These functional Au-NPs also served as crosslinker for the biotinylated ssDNA receptor. After hybridization with the complementary biotinylated ssDNA and the labelling step with streptavidin tagged QDs, a particle-particle distance of around 15-20 nm could be estimated. Compared to the setup using streptavidin as receptor linker an eight fold SPRi signal enhancement could be obtained and demonstrates the appropriateness of such additional signal amplification in biosensor applications using SPRi as transduction technique. The perspective lies in determining the efficiency of this principle with ssDNA of different lengths todetermine an optimal distance range. A real DNA sensor setup can then be imagined using a biotinylated receptor unit that hybridizes with an unmodified DNA target, which can then be labelled with a secondary QD tagged DNA. The beneficial effect of the combination of these nano-species might also be extended to immunosensors when the operational distance widow is determined.

References

1. C. Wong and M. Olivo, *Plasmonics*, 2014, 1-16.

2. S. Scarano, M. Mascini, A. P. F. Turner and M. Minunni, *Biosens. Bioelectron.*, 2010, **25**, 957-966.

3. H. Wei, D. Ratchford, X. Li, H. Xu and C.-K. Shih, *Nano Lett.*, 2009, **9**, 4168-4171.

4. L. Malic, M. G. Sandros and M. Tabrizian, *Anal. Chem.*, 2011, **83**, 5222-5229.

5. Y. Li, H. Schluesener and S. Xu, *Gold Bull*, 2010, **43**, 29-41.

6. T. Špringer and J. Homola, *Anal. Bioanal. Chem.*, 2012, **404**, 2869-2875.

7. Hong, X., & Hall, E. A. (2012). *Analyst*, *137*(20), 4712-4719.

8. Michalet, X.; Pinaud, F. F.; Bentolila, L. A.; Tsay, J. M.; Doose, S.; Li, J. J.; Sundaresan, G.; Wu, A. M.; Gambhir, S. S.; Weiss, S. *Science* **2005**, *307*, 538.

9. Medintz, I. L.; Uyeda, H. T.; Goldman, E. R.; Mattoussi, H. *Nat. Mater.* **2005**, *4*, 435.

10. Daniel, M. C.; Astruc, D. *Chem. Re*V.**2004**, *104*, 293.

11. Dubertret, B.; Calame, M.; Libchaber, A. J. *Nat. Biotechnol.* **2001**, *19*, 365.

12. M. Frasco and N. Chaniotakis, *Sensors*, 2009, **9**, 7266-7286.

13. L. Dyadyusha, H. Yin, S. Jaiswal, T. Brown, J. J. Baumberg, F. P. Booy and T. Melvin, *Chem. Commun.*, 2005, 3201-3203.

14. Z. Dai, J. Zhang, Q. Dong, N. Guo, S. Xu, B. Sun and Y. Bu, *Chin. J. Chem. Eng.*, 2007, **15**, 791-794.

15. M. M. Maye, O. Gang and M. Cotlet, *Chem. Commun.*, 2010, **46**, 6111-6113.

16. Malic, L.; Cui, B.; Tabrizian, M.; Veres, T. Opt. Express 2009,17, 20386.

17. S. Cosnier and A. Lepellec, *Electrochim. Acta*, 1999, **44**, 1833-1836.

18. R. Villalonga, R. Cao, A. Fragoso, A. E. Damiao, P. D. Ortiz and J. Caballero, *J. Mol. Cat. B.*, 2005, **35**, 79-85.

19. M. Holzinger, M. Singh and S. Cosnier, *Langmuir*, 2012, **28**, 12569–12574.

20. Forster, T.Ann. Phys.1948,437,55–75

21. R. S. Swathi and K. L. Sebastian, J. Chem. Sci., Vol. 121, No. 5, September 2009, pp. 777–787

22. S. Kühn, U. Håkanson, L. Rogobete and V. Sandoghdar, *Phys. Rev. Lett.*, 2006, **97**, 017402

Nanomaterials and Nanostructures

Section III

Nanodiamonds and nanotubes based 3D scaffolds for biosensor

Chapter 5

5.1 Context

In the last chapter, signal amplification through biomolecules modified with nanomaterials depending upon their unique absorption properties was studied. Another approach towards enhancing sensitivity of the biosensors involves the modification of transducer with nanomaterials itself. The formation of nanostructures on electrodes is a steady increasing research field since such nanostructured electrodes drastically improve the performances of electric devices. There are a huge number of possible applications for the use of nanostructured electrodes in solar cells [1], for energy storage, as capacitors, for energy conversion [2,3], and as electrochemical biosensors [4]. There are many examples for the formation of nanostructures on electrodes using nanoparticles, carbon nanotubes (CNTs) and other nanomaterials [4] where these nanomaterials can be linked to the electrode via self-assembled monolayer (SAM) [5], layer by layer (LBL) techniques [6], direct growth of highly entangled [7] or aligned nanotubes [8–10], or template assisted formation of nanostructures [11].

Designing of nanostructures composed of carbon nanotubes and nanodiamonds has been theoretically studied in recent years [12] and their applications in biotechnology or electronics have been envisioned. Lots of efforts were invested showing the appropriateness of both, nanodiamonds [13,14] and carbon nanotubes [15] individually in bioanalytics but no significant research has been conducted on nanostructures based on the combination of carbon nanotubes (CNTs) and nanodiamonds (NDs). Since several years, highly porous nanostructures combining nano-objects and carbon nanotubes were designed in order to develop high performance biosensors [16]. Recently, it has been reported that using different functionalization methods for carbon nanotubes, different densities of attached nanoparticles on the nanotubes are obtained [17]. In particular, the use of nanostructured materials in

electrochemical biosensor devices enables the immobilization of a high number of receptor molecules or biocatalyst due to the enhanced surface/volume ratio.

Within this chapter, highly porous 3D nanostructured scaffolds are formed using carbon nanotubes and nanodiamonds for biosensor applications. The deposition of nanodiamonds on CNTs was optimized to obtain porous nanostructures for the diffusion of biomolecules of sizes up to 3-10 nm. This was also made to create an optimal spacing between the deposited layers of carbon nanotubes leading to nanochannels of suitable size in the device. The porous nanostructured scaffolds were reinforced via electrogeneration of an ultrathin functional polypyrene film around the whole structure. This polymer also allows efficient immobilization of the bioreceptor unit (here, GOx-B) *via* affinity interactions. Such 3D layered structures improved drastically the sensor performances compared to the equivalent pure nanotube set-up.

5.2 Scaffold construction and their characterization

The different nanostructures based on different possibilities such as only nanotube modified electrodes, a mixture of nanotubes and nanodiamonds and layer by layer nanotube and nanodiamond deposition on electrodes were investigated and characterized. For the different approaches to form the nanostructures on electrode using CNT/ND mixtures or layer-by-layer techniques, the CNTs were oxidized to achieve water solubility of this material.

In order to evaluate different preparation methods to form the porous nanostructures on electrodes from aqueous dispersions, the SWCNTs were treated with HNO_3 forming hydrophilic groups out of the sidewall carbon atoms. This surface modification of CNTs leads to a reduced hydrophobicity and to the possibility for improved interactions with the functional ND shell. ND powders prepared by explosion techniques present a novel class of nanomaterials possessing unique surface properties. Due to the very small particle size (2–10 nm), a larger percentage of atoms in NDs contribute to the defect sites on grain boundaries than in single crystal natural or microcrystalline synthetic diamonds. For example, in individual 4.3 nm spherical particles of ND comprising about 7200 carbon atoms, nearly 1100 atoms are located at the surface [18]. For this reason, the surface modifications of the nanosized diamond can affect the bulk properties of this material more strongly than those of micro- and macroscale diamonds. They have therefore been considered as potential medical

agents due to their high adsorption capacity, high specific surface area, and chemical inertness [18–20] and were suggested for the design of biosensors as stable biologically active substrates after DNA-modification [21].

5.2.1 Oxidation of Single – Walled Carbon nanotubes (SWCNTs)

Single-walled carbon nanotubes (SWCNTs), produced by the HiPCO® process (Purified, Unidym Grade/Lot #PO346) were purchased from Unidym Inc. and oxidized with 69 % nitric acid (10.8 $mol.L^{-1}$) by stirring under reflux at 110°C for 2 h. After cooling down to room temperature, the reaction mixture was filtered over a cellulose membrane filter (pore size 0.45 μm) and washed several times with distilled water. The solid was re-dispersed in distilled water and filtered again to remove entrapped or intercalated acid. Further washing steps were carried out with distilled water until the filtrate became neutral pH. The resulting black solid was re-dissolved in slightly basic sodium carbonate (Na_2CO_3) water (pH 9.0) to disperse homogeneously oxidized nanotubes (SWCNTs-ox) and to dissolve a large amount of the formed amorphous carbon around the nanotubes. Not dispersed material was allowed to deposit. The supernatant was decanted off and filtered over regenerated cellulose. The resulting oxidized SWCNTs were washed with distilled water and then dried in vacuum.

5.2.2 Synthesis of nanodiamonds

We used commercial ND powder (size 2–10 nm, specific surface of 300 $m^2.g^{-1}$) and obtained from the company SINTA (Ukraine, Kharkov) in this study. These NDs were synthesized by detonation of specially prepared charges from trotyl-hexogen mixture in explosive chambers filled with a non-oxidizing environment. The resulting diamond blend (mixture of diamonds with non-diamond forms of carbon) was subjected to chemical treatment in an environment of nitric acid at high temperature and pressure, followed by post treatment and repeated washing. These NDs have classic cubic (diamond) crystal lattice with essential surface defects (hydroxylic, carbonylic, carboxylic), which determines high surface energy of such crystals. The ND samples were received as aqueous dispersions (5 %) and diluted to ten times. Features of the technological process of the ND and size distribution of the nanodiamonds are described by Aleksenskiy *et al.* [22].

5.2.3 Scaffolds construction

For the control electrodes and the layer-by-layer approaches, the Pt-electrodes (Φ = 2 mm) were modified with 10 µL of SWCNTs-ox dispersed in distilled water (0.1 mg mL^{-1}) by classical casting method [23]. 5 µL of NDs dispersion (0.5%) were then deposited on the SWCNTs-ox layer. Further CNT and ND layers were formed accordingly by depositing 5 µL of both repetitively. Other electrodes were modified by casting 10 µL of a SWCNTs ox/ND mixture (1:1). These as formed deposits were finally dipped in a 4 $mmol.L^{-1}$ solution of pyrene-NTA [24] in CH_3CN to obtain an ultrathin coating providing anchoring groups for bioreceptor immobilization all over the framework **(Figure 1)**.

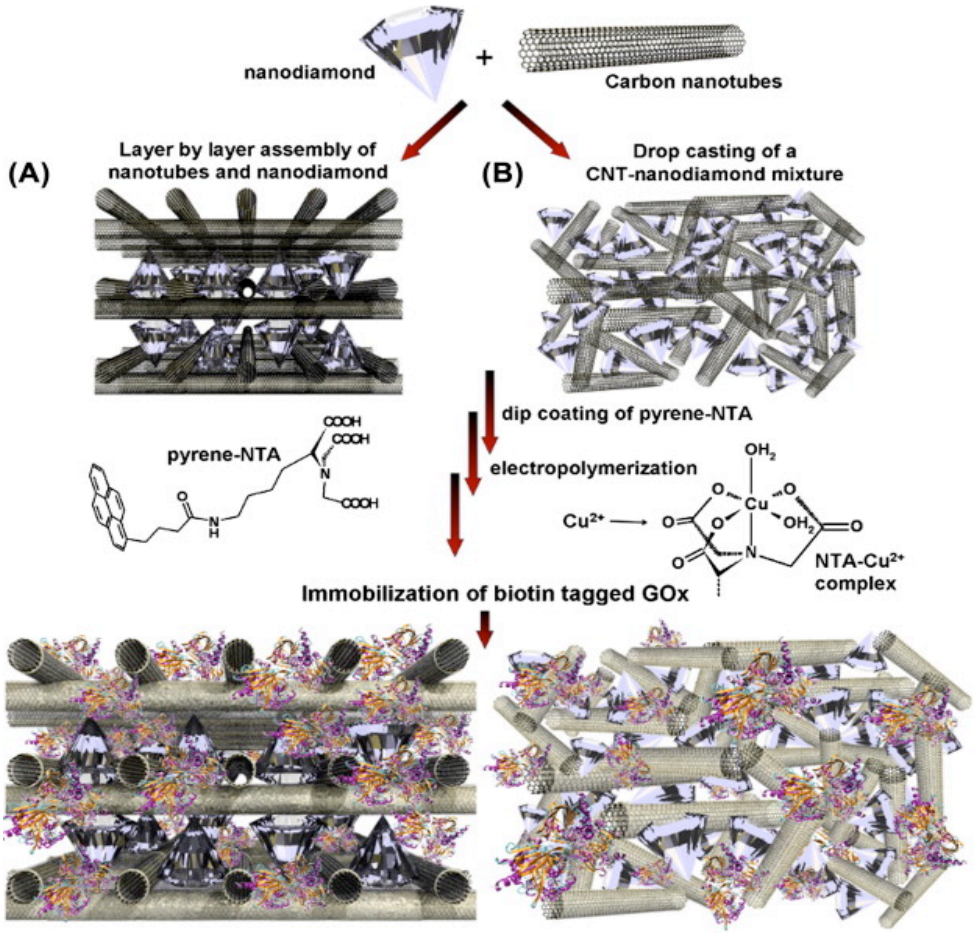

Figure 1. *(A) Schematic representation of a layer-by-layer and (B) of the mixed SWCNT-ox and ND assembly with subsequent functionalization with pyrene-NTA-Cu^{2+} and biotin tagged GOx, GOx-B.*

5.2.4 Electrochemical characterization

To investigate the pyrene adsorption on the SWCNTs-ox and NDs modified electrode, cyclic voltammetry studies were carried out in a CH_3CN + 0.1 $mol.L^{-1}$ $LiClO_4$ monomer free solution. **Figure 2A** represents the first scan for the SWCNTs-ox without pyrene adsorption on the Pt electrode used as reference. Upon oxidative scanning between 0.5 to 1.5 V, the cyclic voltammogram of the pure SWCNTs-ox deposit without any modification with pyrene-NTA (**Figure 2A**) showed a reversible redox system at 0.1 V *vs* Ag/Ag^+, which was also observed for all other SWCNTs-ox modified electrodes. Luo *et al.* assigned this reversible redox system to the formed "carbonyls" groups on the SWCNT sidewalls during the HNO_3 acid treatment [25]. A control with the deposit of only NDs confirmed no adsorption of pyrene-NTA onto the nanodiamonds (**Figure 2B**).

Figure 2C-E represents the cyclic voltammograms for the elecrodes prepared by a similar procedure as (**A**) but modified further with SWCNT-ox/ND mixtures or ND and SWCNT-ox layers after such dip-coating with pyrene-NTA. For all coated nanostructures, the presence of two irreversible peaks for the first scan of each electrode indicates the formation of pyrene radicals [26] initiating the polymerization. After integration of the oxidation peaks of the first scan of the pyrene oxidation and calculating its ratio, the amount of attached pyrene groups can already be estimated. The best ratio could be obtained for the layer-by-layer SWCNT-ox/ND/SWCNT-ox structure (**Figure 2D**) and for the deposition of the SWCNT-ox/ND mixture (**Figure 2C**) as a result of good diffusion of the monomer through these structures. However, the SWCNT-ox/ND/SWCNT-ox/ND/SWCNT-ox layers (**Figure 2E**) seems to trigger to some extent partial collapse of the scaffold structure that perturbs the diffusion of pyrene monomers, leading to, a reduced polymerized pyrene coating.

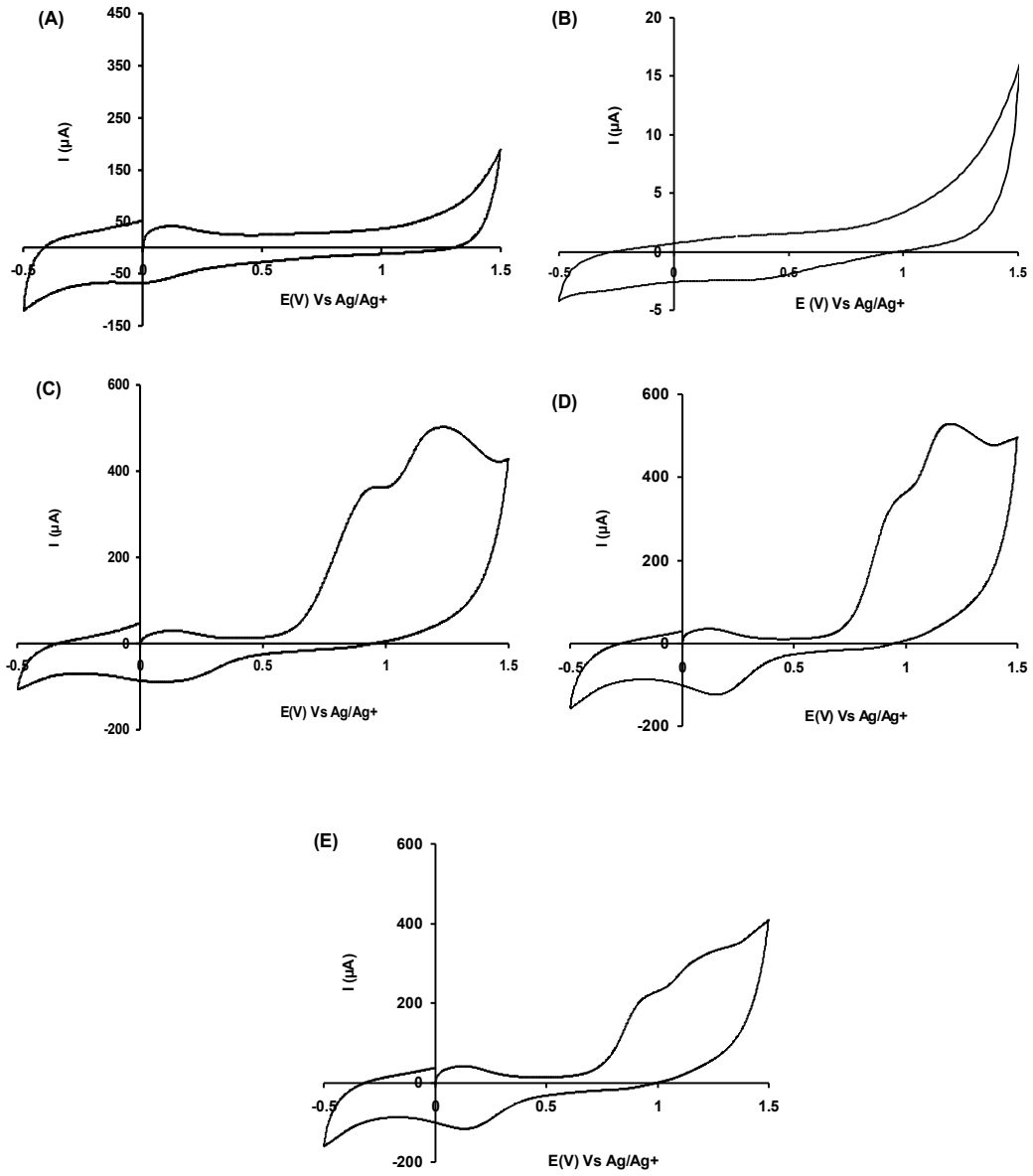

Figure 2. *Cyclic voltammetry characterization of (A) SWCNT-ox and (B) NDs modified Pt electrode without functionalization, and SWCNT-ox modified Pt electrode with (C) SWCNT-ox/ND mixture, (D) ND/SWCNT-ox layers and (E) ND/ SWCNT-ox/ND/SWCNT-ox layers functionalised by dip coating in pyrene-NTA solution.*

The non-covalent attachment of pyrene derivatives via dip-coating on the sidewalls of CNTs forms an ultrathin layer of pyrene groups which can further be electropolymerized [17,26].

5.2.5 Scanning electron microscopy imaging

The porosity of the formed nanostructures was evaluated using scanning electron microscopy of a cross section of the layer-by-layer deposition of SWCNTs-ox and NDs as shown in **Figure 3** (middle) where the ND/SWCNT-ox interfacial layer (**Figure 3A**, left) and the SWCNTs-ox top layer (**Figure 3B**, right) were zoomed in. SWCNTs-ox shows a highly dense packaging in dry state [27]. This highly dense structure is perturbed in presence of the NDs, which appears as bright spots in the SEM images.

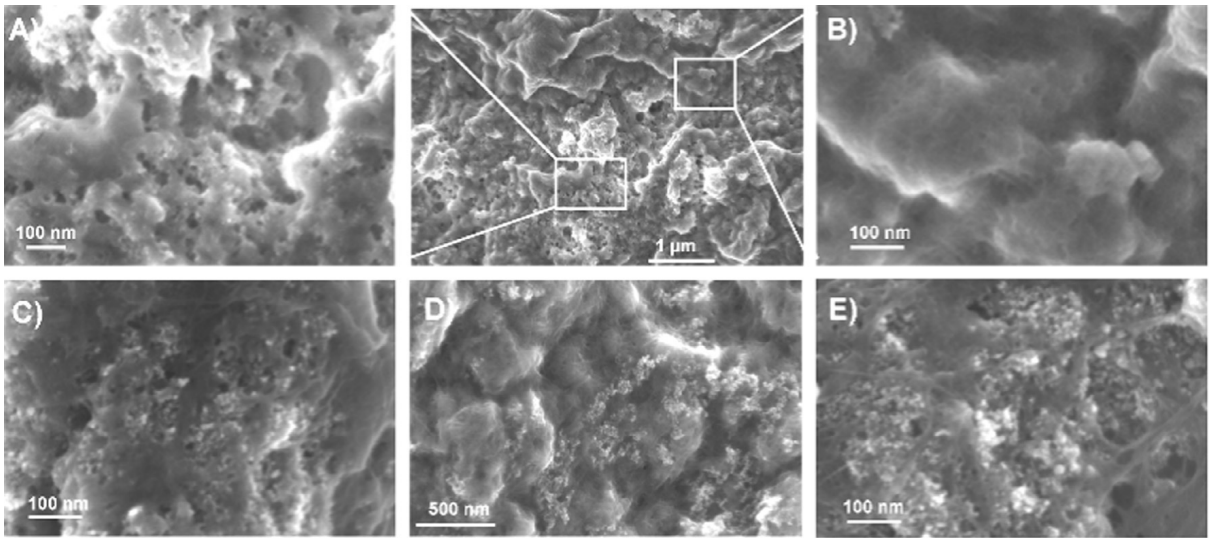

Figure 3. *SEM image for the layer-by-layer deposition of SWCNT-ox/ND/SWCNT-ox (in the middle). Zoom of SWCNT-ox and ND interfacial layer (A) and nanotube top layer (B). (C)–(E): SEM images of different regions of the mixed SWCNT-ox/ND deposit.*

Nevertheless, a layered structure is not observed which might be due to some incorporation of the NDs in the nanotube layer during deposition of the liquid phases. In spite of the dense packaging of the nanotubes, a highly porous structure was formed using the layer-by-layer deposition technique (**Figure 3A**, left). A less pronounced porosity is observed for the deposited mixture of NDs and SWCNTs-ox (**Figure 3C-E**) that reveals more compact structures (**Figure 3C and E**) and separated domains of SWCNT-ox and ND agglomerates (**Figure 3D**). This is not surprising considering the one step deposition of the mixture whereas for the layer-by-layer technique, cavities can be formed by removing weakly adsorbed NDs during the rinsing step which are not filled after the nanotube deposition. It has to be noted, that these SEM images are not completely representative to evaluate the porous scaffold structure since morphological changes might occur during the drying of the sample.

5.2.6 Spectroscopic characterization

The SWCNT-ox/ND assemblies were studied using Raman and FTIR spectroscopy.

5.2.6.a. Raman Spectroscopy

Raman scattering has been used to probe the features of sp^2 and sp^3 carbon materials [28]. **Figure 4A** shows a representative spectrum of the as received SWCNT sample produced by the HiPCO® process [29]. After oxidation using nitric acid, an expected increase of the D-Band around 1350 cm^{-1} is observed (**Figure 4B**) [27]. Contrary to CNTs, NDs have no resonant behavior [30] and therefore, only one clear peak at 1318 cm^{-1}, indicating the vibration mode of the ND sp^3 lattice, is observed. A weakly pronounced wave around 1610 cm^{-1} reveals the presence of amorphous carbon at the ND surface (**Figure 4D**). Not only the non-resonant behavior but also the luminescence of NDs [31] clearly reduced the signal capture of the SWCNT-ox/ND assembly where no difference between the layer-by-layer structure and the deposit of a mixture was observed. Nevertheless the layer-by- layer deposition, representative for both configurations, as depicted in **Figure 4C,** shows all features of a CNT spectrum where the D and G band might contain the features of NDs.

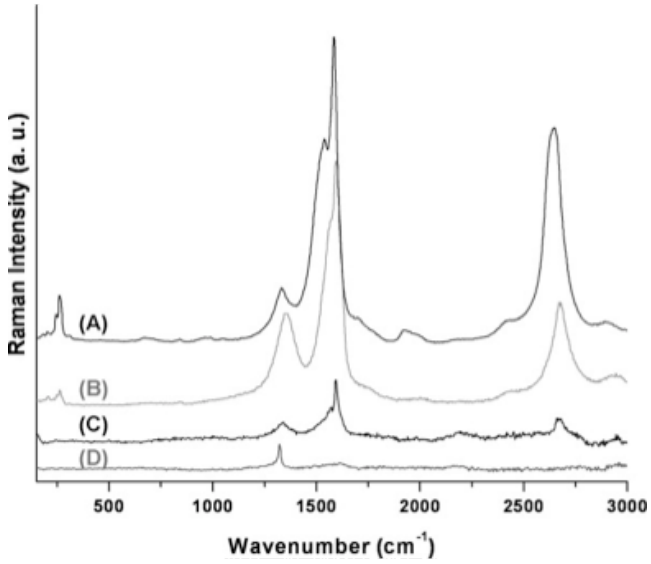

Figure 4. *Raman spectra of (A) as received SWCNTs, (B) SWCNTs-ox, (C) SWCNTs-ox /ND mixture, and (D) ND.*

5.2.6.b. FTIR Spectroscopy

Infrared (IR) spectroscopy, on the other hand, has shown significant promise for the study of SWNT wall chemistry. Several examples of tube wall functionalization have been reported where IR spectra were used to identify the functional groups added to the tube wall [32]. FITR spectrum for as received SWCNTs showed no features in the carbonyl region (**Figure 5A**). Conversely, the C=O stretching mode of oxidized CNTs is represented as a broad band centered at 1722 cm^{-1} (**Figure 5B**). A similar peak is observed for the ND spectrum with its maximum at 1731 cm^{-1} (**Figure 5C**).

The FTIR spectrum of the SWCNTs-ox/ND mixture (**Figure 5D**) reveals some interactions between the carboxylic acid groups of the NDs and the nanotubes. The main part of the carboxyl stretching mode shifted to 1765 cm^{-1} forming a very broad band that indicates some kind of equilibration of the respective protonated and deprotonated (proton donor) forms of the carboxylic acid groups [33] of NDs and SWCNTs-ox. Some further weak modes, centered at 1698 cm^{-1} and 1716 cm^{-1}, can be due to the formation of hydrogen bonds [34] between the nano-moieties. A blue shift of the bend mode of water (1574 cm^{-1} to 1601 cm^{-1}, **Figure 5B** and **D**) underlines this thesis [35].

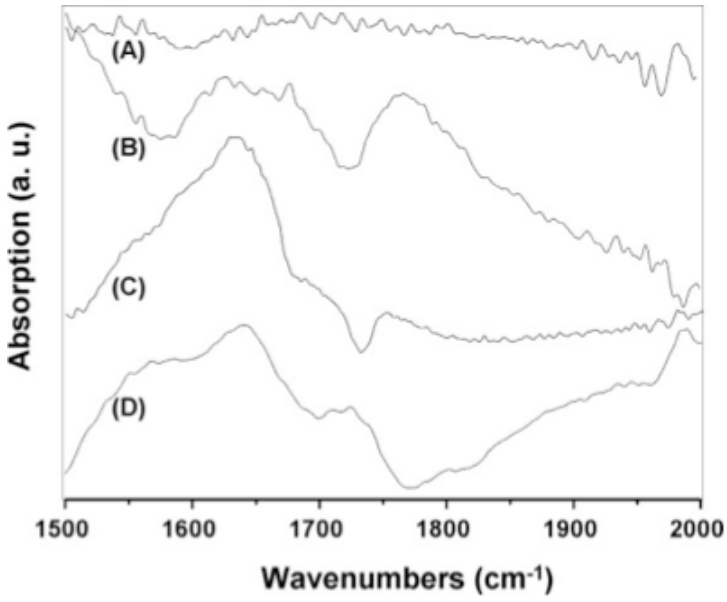

Figure 5. *FTIR spectra of (A) as received SWCNTs, (B) SWCNTs-ox, (C) ND, and (D) the SWCNTs-ox /ND mixture.*

5.3. Fabrication of the bioelectrodes and amperometric measurements

The as prepared electrodes were then soaked for 20 min in 0.01 mol.L^{-1} CuCl2 acetate buffer solution (0.1 mol.L^{-1}, pH 4.8) followed by successively washing for 5 min with NaCl (0.5 mol.L^{-1}) and phosphate buffer (0.1 mol.L^{-1}, pH 7.0). All modified electrodes were incubated in phosphate buffer solution (0.1 mol.L^{-1}, pH 7.0) containing biotinylated modified GOx (0.5 mg.mL^{-1}) for 30 min at 4 °C. The resulting electrodes were then rinsed several times with phosphate buffer solution (0.1 mol.L^{-1}, pH 7.0).

GOx-B was immobilized throughout the above-mentioned SWCNT-ox/ND/SWCNT-ox assembly via subsequent coordination of copper (II) ions at the NTA chelate and the biotin groups of GOx at the Cu^{2+}–NTA complex. The resulting sensors were then calibrated using amperometry. The different procedures to form the nanostructures were evaluated in order to determine the most promising setup for bioanalytical devices. The performance of the biosensors for glucose determination was examined in stirred 0.1 mol.L^{-1} phosphate buffer. Since GOx catalyzes the aerobic oxidation of glucose withthe concomitant production of H_2O_2, the biosensors were potentiostated at 0.6 V *vs* SCE in order to detect amperometrically the generated H_2O_2.

Figure 6 shows the anodic current response of the biosensors as a function of glucose concentration of all biosensor configurations based on different deposition procedures of SWCNTs-ox and NDs. All electrodes were initially modified with 10 µL SWCNTs-ox deposits and used as support electrodes for all biosensor configurations. A control electrode was further modified only with SWCNTs-ox (5 µL) in order to keep the same amount of SWCNTs-ox for all set-ups. After its functionalization via electrogeneration of a thin polypyrene-NTA layer and completing the biosensor by the immobilization of biotin labelled GOx, such modified electrodes displayed in average (RSD = 4.23%) a sensitivity of 20.22 mA.L^{-1}.mol.cm^{-2}, determined by the slope of the linear part of the calibration curve (**Figure 6A**), and a maximum current density of 40.44 µA.cm^{-2}.

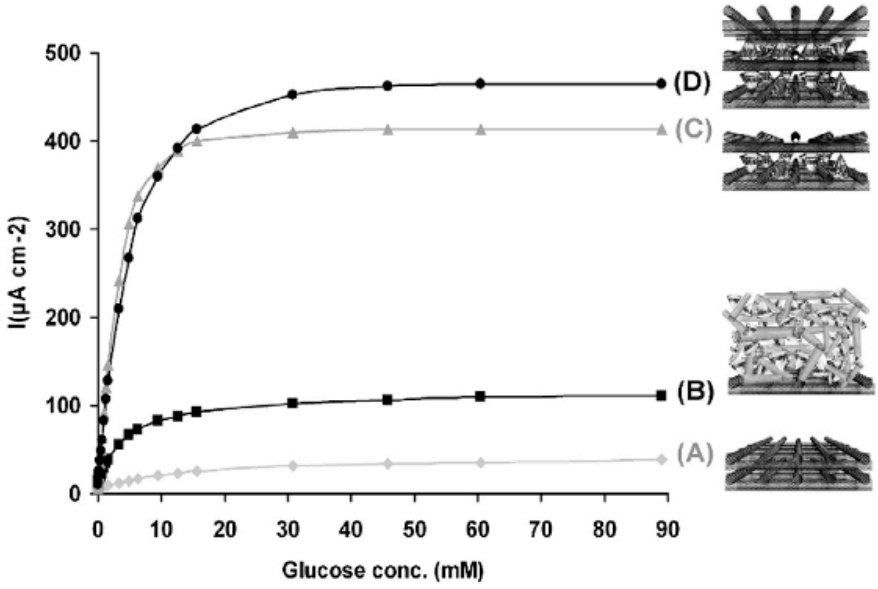

Figure 6. *Schematic representations of SWCNTs-ox and ND assemblies and corresponding calibration curves for glucose for (A) control reference electrode modified with only with SWCNT-ox/SWCNT-ox layer, (B) SWCNTs-ox/(SWCNT-ox–ND mixture), (C) SWCNT-ox/ND/SWCNT-ox layers, and (D) SWCNT-ox/ND/SWCNT-ox/ND/SWCNT-ox layers.*

NDs were then introduced in the nanostructures to avail the unique properties of both components in terms of high surface area-to-volume ratio and high electroactivity. For this purpose, two assemblies were prepared for glucose quantification. Firstly, a mixture of 5 µL of SWCNTs-ox and 5 µL of a ND suspension (0.5%) was deposited by drop-casting method on the electrode having homogeneous deposit of 10 µL of SWCNTs-ox. The quantities of the used dispersions were optimized towards best biosensor performances while varying the amount of deposited ND dispersion keeping the SWCNT-ox deposits constant. The SWCNTs-ox and ND framework was then reinforced by incubating the whole assembly in pyrene-NTA solution for 20 min functionalizing the whole SWCNTs-ox and ND deposit through π-stacking interactions followed by electrogeneration of an ultrathin film. The finalized sensor set-up after GOx–B immobilization via copper coordination showed an average (RSD = 2.05%) maximum current density of 111.8 $\mu A.cm^{-2}$ and sensitivity was 32.16 $mA.L^{-1}mol.cm^{-2}$ (**Figure 6B**). This increase can be assigned to the presence of small size NDs inside the SWCNTs-ox matrix, endowing improved specific surface characteristic. Secondly, a layer-by-layer assembly constituted of SWCNTs-ox and NDs was prepared. 5 µL of ND was first spread and dried on SWCNT-ox modified electrode followed by another layer of 5 µL of SWCNTs-ox. Also for this setup, 5 µL

deposition of the ND dispersion gave optimal sensor performances. The assembly was then modified as usual with functionalized pyrene and successively with Cu^{2+} and GOx-B. A drastic change in both the average (RSD = 5.66%) maximum current density (414 $\mu A.cm^{-2}$) and sensitivity (85.78 $mA.L^{-1}.mol.cm^{-2}$) was observed compared to previous mentioned nanostructures (**Figure 6C**). The marked increase in maximum current density values (from 40.44 to 414 $\mu A.cm^{-2}$) clearly indicates a drastic increase in the amount of immobilized amount of GOx-B within the whole composite matrix. This reflects an expansion of the SWCNT-ox deposit by NDs that facilitates the protein penetration. Furthermore, the nanostructured scaffold provides also after immobilization of the receptor unit an optimized diffusion of the analyte (glucose) throughout the matrix. These results were compared with the classical biotin–avidin–biotin/streptavidin layer system on SWCNTs-ox modified electrode [26,36], clearly indicates that highly porous, 3D nanostructures based on SWCNTs-ox and NDs show 80-fold increase in biosensor performance (in both maximum current density and sensitivity). Compared to the biosensor performances obtained using the SWCNTs-ox/ND mixture, an almost 4-fold increase could be obtained using the same amounts of SWCNTs-ox and NDs.

An attempt to further improve the biosensor performances was realized by depositing a further level of NDs and SWCNTs-ox before bioreceptor immobilization. The obtained average (RSD = 2.87%) maximum current density of 465 $\mu A.cm^{-2}$ just slightly increased while the sensitivity (70.71 $mA.L^{-1}.mol.cm^{-2}$) of this biosensor setup even declined slightly (**Figure 6D**). Conversely, the increase of the maximum current density reflects the immobilization of a higher amount of GOx-B even when the value obtained with the one level construction could not be doubled. However, the estimation of the increase in the amount of immobilized GOx-B through the maximum current value may be underestimated. Indeed, the theoretical doubling of the GOx-B amount must lead to a glucose oxidation and oxygen consumption that occurs mainly at the solution/matrix interface. As a consequence, a large part of the enzymatically generated H_2O_2 may diffuse to the bulk solution instead to be detected at the underlying electrode surface. Likewise, the sensitivity decrease is most likely due to the increased distance between immobilized enzymes and the electrode surface and an increase in steric hindrances towards the permeation of both glucose and H_2O_2 through the nanoassembly.

5.4 Conclusion

The construction of highly porous, three-dimensional nanostructures based on an innovative process combining SWCNTs-ox and NDs were demonstrated using different approaches. The functionalization of these components with affinity system like NTA/Cu^{2+}/biotin was simply achieved via non-covalent interactions of pyrene with nanotubes. The assembly based on SWCNTs-ox and ND layered structure provided better diffusion and an increase in the amount of immobilized of biological entities. In spite of the layer-by-layer approach, the whole assembly can be functionalized with pyrene –NTA to obtain anchoring points all over framework to immobilize a high number of bioreceptor units like biotin or histidine tagged proteins. It should be noted that these biosensor performances for the detection of glucose are among the best described to date, the highest sensitivity and maximum current density being 58–82 $mA.L^{-1}.mol.cm^{-2}$ and 410–950 $\mu A.cm^{-2}$, respectively [37,38]. The latter are relative to biosensor configurations based on the physical entrapment of enzymes inside inorganic coatings. By comparison of similar biosensor performances, it appears that the affinity anchoring of GOx within the SWCNT-ox and ND assembly may correspond to the entrapment of 330 $\mu g\ cm^{-2}$. Taking into account that one GOx occupies an area of 56 nm^2, a compact monolayer corresponds to a coverage of 3 x 10^{-12} $mol.cm^{-2}$ or 0.48 $\mu g.cm^{-2}$ [39]. Consequently, the layered SWCNTs-ox/ND composite allows for the immobilization of the equivalence of 687 compact enzyme monolayers and thus highlights the advantage of this strategy for biomolecule immobilization owing the large specific surface of carbon nanotubes. Furthermore, optimal diffusion of the substrate was achieved even after the immobilization of the bioreceptor unit. The homogeneous and reproducible deposition of SWCNTs-ox - ND layers up to two levels revealed that this setup still can be optimized. This approach for constructing highly porous 3D nanostructured bioelectrodes will contribute as highly sophisticated material for the development of bioelectrode sused in biosensors or biofuel cells [Results published in Carbon, see Ref 40].

References

1. Law M, Greene LE, Johnson JC, Saykally R, Yang P. Nat Mater 2005;4:455–9.

2. Simon P, Gogotsi Y. Nat Mater 2008;7:845–54.

3. Arico AS, Bruce P, Scrosati B, Tarascon J-M, Schalkwijk WV. Nat Mater 2005;4:366–77.

4. Gooding JJ, Lai LMH, Goon IY. Weinheim: Wiley-Vch Verlag GmbH & Co. 2009. p. 1–56.

5. Love JC, Estroff LA, Kriebel JK, Nuzzo RG, Whitesides GM. Chem Rev 2005;105(4):1103–70.

6. Blonder R, Sheeney L, Willner I. ChemCommun 1998;13:1393–4.

7. Chen J, Minett AI, Liu Y, Lynam C, Sherrell P, Wang C, et al. Adv Mat 2008;20(3):566–70.

8. Hata K, Futaba DN, Mizuno K, Namai T, Yumura M, Iijima S. Science 2004;306(5700):13624.

9. Bennett RD, Hart AJ, Cohen RE. Adv Mat 2006;18(17):2274–9.

10. Esconjauregui S, Fouquet M, Bayer BC, Ducati C, Smajda R, Hofmann S, et al. ACS Nano 2010;4(12):7431–6.

11. Walcarius A, Kuhn A. Trends Anal Chem 2008;27(7):593–603.

12. Shenderova OA, Areshkin D, Brenner DW. Mat Res 2003;6(1):11–7.

13. Liu YL, Sun KW. Nanoscale Res Lett 2010;5(6):1045–50.

14. Zhu Y, Li J, Li W, Zhang Y, Yang X, Chen N. 2012;2(3):302–12.

15. YangW, Ratinac KR, Ringer SP, Thordarson P, Gooding JJ, Braet F. AngewChemInt Ed 2010;49(12):2114–38.

16. Le Goff A, Holzinger M, Cosnier S. Analyst 2011;136(7):1279–87.

17. Haddad R, Holzinger M, Villalonga R, Neumann A, Roots J, Maaref A, et al. Carbon 2011;49:2571–8.

18. Shenderova O, Zhirnov V, Brenner D. Crit Rev Solid State Mater Sci 2002;27(3–4):227–356.

19. El-Say KM. J Appl Pharm Sci 2011;1(6):29–39.

20. Dolmatov VY. Russ Chem Rev 2001;70(7):607–26.

21. YangW, Auciello O, Butler JE, CaiW, Carlisle JA, Gerbi JE, et al. Nat Mater 2002;1(4):253–7.

22. Aleksenskiy AE, Eydelman ED, Vul AY. NanosciNanotechnolLett 2011;3(1):68–74.

23. Haddad R, Cosnier S, Maaref A, Holzinger M. Sensor Lett 2009;7(5):801–5.

24. Holzinger M, Baur J, Haddad R, Wang X, Cosnier S. ChemCommun 2011;47(8):2450–2.

25. Luo H, Shi Z, Li N, Gu Z, Zhuang Q. Anal Chem 2001;73(5):915–20.

26. Haddad R, Holzinger M, Maaref A, CosnierS, ElectrochimActa 2010;55(27):7800–3.

27. Kukovecz A, Kramberger C, Holzinger M, Kuzmany H, Schalko J, Mannsberger M, et al. J PhysChem B a2002;106(25):6374–80.

28. Analytical Applications of Raman Spectroscopy; Michael J. Pelletier, Ed.;Blackwell Science: Cambridge, MA, 1999

29. Chen G, Sumanasekera GU, Pradhan BK, Gupta R, Eklund PC, Bronikowski MJ, et al. J NanosciNanotechnol 2002;2(6):621–6.

30. Prawer S, Nugent KW, Jamieson DN, Orwa JO, Bursill LA, Peng JL. ChemPhysLett 2000;332(1–2):93–7.

31. Dolenko TA, Burikov SA, Rosenholm JM, Shenderova OA, Vlasov II. J PhysChem C 2012;116(45):24314–9.

32. Un Jeong Kim, Clascidia A. Furtado, Xiaoming Liu, Gugang Chen, and Peter C. Eklund, J. Am. Chem. Soc. 2005,127, 15437–15445.

33. Nabedryk E, Paddock ML, Okamura MY, Breton J. Biochemistry 2007;46(5):1176–82.

34. Jones RN, Angell CL, Ito T, Smith RJD. Can J Chem1959;37(12):2007–22.

35. Zelsmann HR. J MolStruct 1995;350(2):95–114.

36. Baur J, Holzinger M, Gondran C, Cosnier S. ElectrochemCommun 2010;12(10):1287–90.

37. Cosnier S, Mousty C, Gondran C, Lepellec A. Mater SciEng C 2006;26(2–3):442–7.

38. Shan D, Zhu M, Han E, Xue H, Cosnier S. BiosensBioelectron 2007;23(5):648–54.

39. Cosnier S, Stoytcheva M, Senillou A, Perrot H, Furriel RPM, Leone FA. Anal Chem 1999;71(17):3692–7.

40. Singh, M.; Holzinger, M.; Biloivan, O.; Cosnier, S. Carbon, **2013**, 61, 349.

Magnetic nanoparticles and nanotubes based 3D scaffolds for biosensors

Chapter 6

6.1 Context

The design of 3D porous nanostructures that increase the density of the immobilized bioreceptor units, targets mainly the detection of small organic molecules or ions which can easily diffuse throughout these mostly mesoporous (2-50 nm) structures [1,2]. In the particular case of immunosensors, not only the biorecognition moieties (*e.g.* an antigen) have to be immobilized within these nanostructured coatings, but also the analyte, the corresponding antibody, should have unhindered access to its corresponding antigen [3]. Furthermore, for optical or electrochemical transduction, an additional secondary antibody, labelled with a fluorescent marker or a redox enzyme should also permeate through these structures [4]. Antigens, antibodies, and labelled secondary antibodies are biological macromolecules with over several nanometers in diameter. In the recent years, great efforts were invested to control pore sizes to extend the beneficial effect of nanostructures from enzymatic biosensing applications to immunosensors [5]. However, the construction of three-dimensional (3D) scaffolds with sufficient large pores allowing for the diffusion of all these biological compounds remains a challenge.

Single-walled carbon nanotubes (SWCNTs) produced by the HiPCO® process are available with almost no carbon impurities and have a relative intact π-system for efficient non-covalent functionalization [6,7]. However, these nanotubes can contain up to 15% (weight) iron catalyst particles, [8] which often require supplementary purification steps for further use of these SWCNTs [9-12]. Based on a recent study revealing magnetic properties of these iron nanoparticle impurities [13], we sought to take advantages of the undesirable presence of these catalyst particles to construct highly porous structures for immunosensing and enzymatic glucose sensing applications through magnetic interaction of these iron particles with commercial super paramagnetic nanoparticles of different sizes (**Figure 1**).

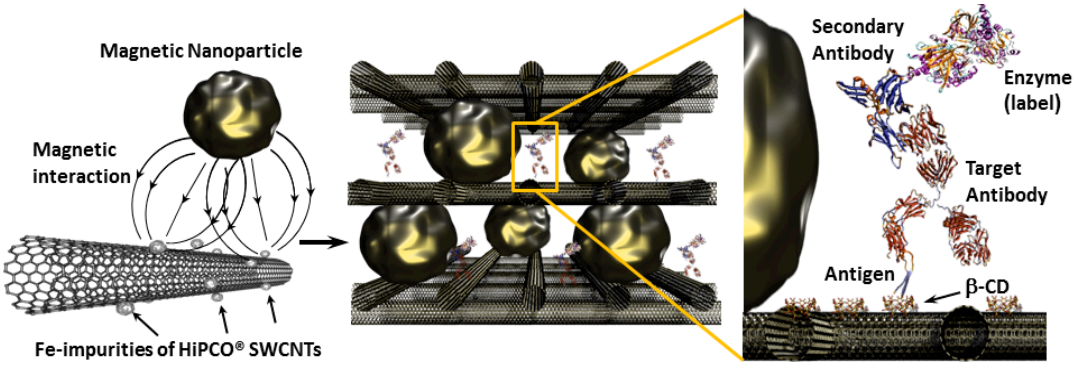

Figure 1. *Schematic representaion of the concept to construct 3D layer by layer scaffolds using HiPCO® produced SWCNTs and magnetic nanoparticles through magnetic interactions, for the immobilization of biomolecules such as antigen- antibody.*

6.2 Scaffold construction and their SEM characterization

The possibility of using iron catalyst impurities of HiPCO® produced SWCNTs as anchor points for magnetic nanoparticles, was first evaluated with magnetic carboxylated nanobeads (mNP) of an average diameter of 100 nm. A first SWCNT layer was formed by drop casting and drying of SWCNT dispersion in N-methyl pyrrolidone (NMP, 0.1 $mg.mL^{-1}$ in 20 µL). After deposition of the magnetic nanoparticles and subsequent rinsing, a relative homogeneous but not very dense layer of these nanoparticles was observed in the scanning electron microscopy (SEM) images (**Figure 2A**). To get further indications that the nanoparticles are principally retained *via* magnetic attraction, latex nanobeads (average diameter 100 nm) with the same surface functions (COOH) were drop cast on the SWCNT deposit. After applying identical treatments, only few individual particles or agglomerates could be identified on the SWCNT deposit (**Figure 2B**).

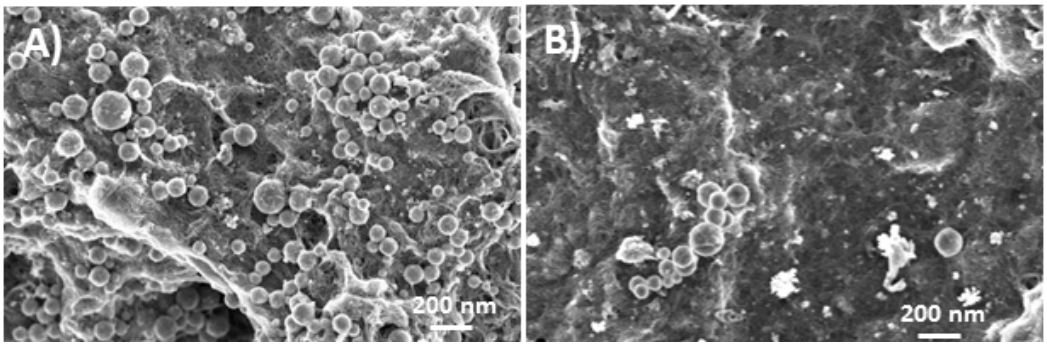

Figure 2. *A) Layer of mNP (100 nm) on the SWCNT deposit after rinsing. B) Layer of latex nanoparticles (100 nm) on the SWCNT deposit after rinsing.*

After deposition of the next SWCNT layer, the resulting structures were examined using SEM. **Figure 3** shows the morphology of the surface and the cross-section of SWCNT-mNP-SWCNT layer and the randomly distributed mNP coated with a second SWCNT deposit. The cross-section of these first layers reveals that nanoparticles are covered by a thin film of web-like SWCNT deposit leaving as wanted some vacancies of up to several hundred nanometers.

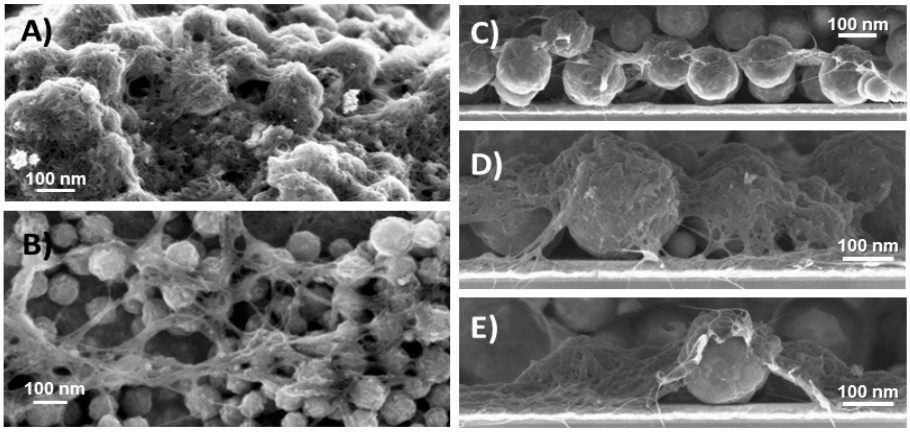

Figure 3. *SEM images of (A and B) the topographic morphology of two representative areas of a SWCNT-mNP (100 nm)-SWCNT layer. C, D, and E are SEM images of the cross-section of these deposits.*

These experiments were also performed using mNPs of 500 nm size and magnetic microbeads (~2.4 µm). **Figure 4** shows the SEM images of a double layer scaffold construction (SWCNT-mNP-SWCNT-mNP-SWCNT layer). Similarly, the top view of these deposits shows a web-like SWCNT layer on the top of both 100 nm and the 500 nm mNPs (**Figure 4A** and **Figure 4B** respectively). The cross-section of these deposits reveals a more compact structure for the 100 nm nanoparticles whereas for the 500 nm nanoparticles, a recognizable LBL structure is visible (**Figure 4D**).

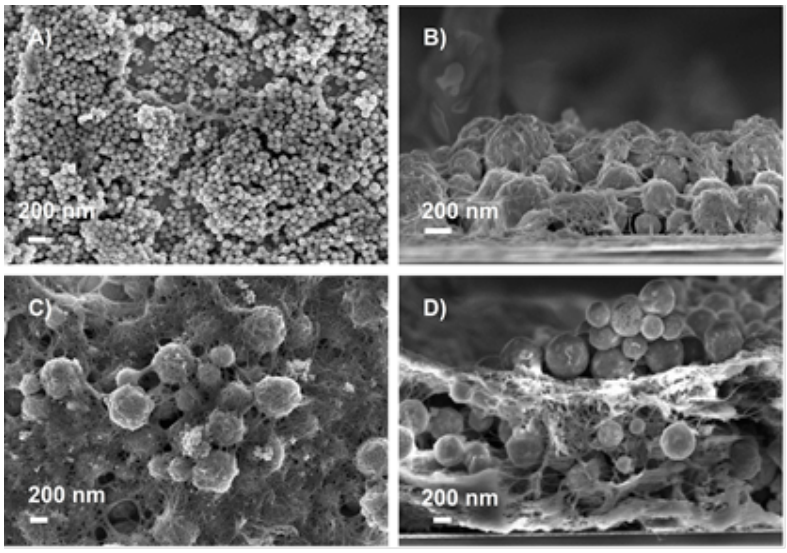

Figure 4. *SEM images of A) top view and B) cross-section of a SWCNT-mNP (100 nm)-SWCNT-mNP (100 nm)-SWCNT deposit. C) Topview and D) cross-section of a SWCNT-mNP (500 nm)-SWCNT-mNP (500 nm)-SWCNT deposit.*

In case of magnetic microbeads, some empty areas of the first SWCNT deposit were found. This might be due to the heavy weight of these particles and insufficient magnetic forces leading to rinsing off some of these microbeads during washing step. In addition, there was not a clear difference between single and double-layered structure.

6.3 Anti-CT antibody detection using the HRP-labelled secondary antibody for amperometric transduction

To determine the most efficient scaffolds for anti-CT detection, all the LBL structures were compared to pure SWCNT deposits with an equivalent amount of nanotubes. The different 3D nanotube/nanoparticle scaffolds were applied to the elaboration of amperometric immunosensors. The first layer of nanotubes (20 µL of 0.1 $mg.mL^{-1}$ in NMP) was deposited on glassy carbon (Φ = 3mm) by classical drop casting [14]. Then, a nanoparticle suspension (5µL, 0.5% volume) was deposited on top of the first SWCNT layer and dried under vacuum followed by washing with PBS. The second SWCNT layer was formed by depositing 10 µL (0.1 $mg.mL^{-1}$) of nanotubes on the nanotube-nanoparticle assembly and dried as described earlier. These steps were carried out using nanoparticles of different sizes (100 nm, 500 nm and 2.4 µm) to determine the appropriate pore size for the specific immunosensor application. Supplement levels were constructed by repeated deposition of nanotube (10 µL, 0.1 $mg.mL^{-1}$) and nanoparticle (5 µL, 0.5% volume) suspensions. The constructed scaffolds were then

functionalized by incubating in a solution of pyrene-β-CD (2 mmol.L^{-1} in NMP) to form a thin pyrene coating throughout the nanotube/nanoparticle deposits [15]. Pyrene-β-CD (see **Chapter 3**) was chosen since the pyrene groups form stable π-stacking interactions with the SWCNT sidewalls and the β-CD groups create a hydrophilic environment throughout the scaffold, enabling better diffusion of the biomacromolecules. Furthermore, β-CD forms stable inclusion complexes with biotin [16] which then allows the use of commercialized biotinylated, antigen-antibody immunosystems. To reinforce the formed construct, the attached pyrene groups were electropolymerized. The pyrene layer was electropolymerized using cyclic voltammetry [17] by scanning between 0 and 1.3 V *vs* Ag/AgCl until the irreversible oxidation wave of pyrene disappeared (in average 2-3 scans).

The "as prepared" electrodes were incubated with biotinylated cholera toxin B subunit (10 µl, 0.5 mg.mL^{-1}) dissolved in 1 % (w/v) BSA/PBST for 20 min. After each step, the electrodes were rinsed with 0.1 mol.L^{-1} PBS (pH 7.0) for several times. The immunosensors were incubated for 20 min with the analyte rabbit anti cholera toxin (anti-CT) antibody (10 µl, 0.5 mg.mL^{-1}). For labelling, horseradish peroxidase-labelled goat anti-rabbit IgG immunoglobulin secondary antibody (10 µl) at a concentration of 0.5 mg.mL^{-1} dissolved in antibody diluent was deposited onto the sample exposed electrode for 20 min at 4°C. The electrodes were then rinsed extensively with PBS. The amperometric set-up for HRP labelled immunosensor is illustrated in **Figure 5**.

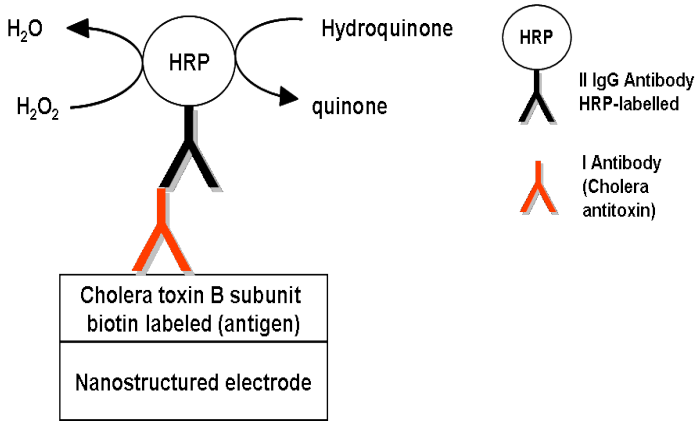

Figure 5. *Amperometric immunosensor set-up based on nanostructured electrode modified with poly(pyrene β-CD) and HRP-labelled secondary antibody as marker for the detection of cholera antitoxin (anti-CT).*

For optimal particle size determination, one analyte concentration (0.5 mg.mL^{-1}) was used. After labelling with the horseradish peroxidase-tagged goat anti-rabbit IgG

immunoglobulin, the maximum current densities of the different setups were determined by potentiostating the electrodes at -0.1 V *vs* Ag/AgCl in presence of hydroquinone (2 $mmol.L^{-1}$) and 1 $mmol.L^{-1}$ of H_2O_2 [4]. HRP catalyses the reduction of H_2O_2, and the oxidation of hydroquinone to quinone species. The enzymatically generated quinone is then reduced at the electrode -0.1 V *vs* Ag/AgCl.

Figure 6 shows the histogram for the single and double layer structures formed with differently sized magnetic nano/microparticles and SWCNTs. As expected, there is a significant increase in immunosensor performance for nanostructures composed of nano/microparticles - nanotubes than for nanotubes only. Furthermore, higher current density was measured for all the double layer structures except for 100 nm. This behaviour may be related to SEM observations, where a more compact structure was observed for 100 nm NPs leading to hindered diffusion of proteins. The highest maximum current density (J_{max} = 117.14 ± 2.5 $\mu A.cm^{-2}$) was recorded for 500 nm particles, clearly indicating the appropriateness of this construct arrangement for subsequent immobilization of the antigen, the analyte, and the HRP labelled secondary antibody. In contrast, the J_{max} value for the same amount of SWCNT without particles only reaches 41% of that observed for 500 nm particles (48.57 ± 0.8 $\mu A.cm^{-2}$). The measured J_{max} also increased for the scaffold made of 100 nm particles and microbeads to reach 57.14 ± 0.9 $\mu A.cm^{-2}$ for 100 nm particles and 89.28 ± 2.7 $\mu A.cm^{-2}$ for microbeads (~2.4 μm), despite the inhomogeneity of the formed deposits. The response time of all anti-CT immunosensors were considerably fast, ranging from 5 to 15 s.

To confirm the beneficial role of magnetic attraction for the assembly of these structures, an additional control experiment using multiwalled carbon nanotubes (MWCNTs) with 95% carbon purity and magnetic nanoparticles (500 nm) was performed under identical conditions as for HiPCO® produced SWCNTs. The combination of HiPCO® produced SWCNTs with its Fe impurities and magnetic nanoparticles of 500 nm size showed to be the best configuration to construct such porous scaffolds for this immunosensor set-up. Furthermore, to evaluate possible nonspecific binding of the secondary antibody and/or HRP on the modified nanotube surface, the poly(pyrene β-CD) modified nanotube/mNP (double layer, 500 nm mNPs) electrodes were incubated in PBS containing the HRP labelled secondary antibody. The obtained maximum current density of J_{max} = 4.3 $\mu A.cm^{-2}$ represents a general error of 3.6% compared to specific immune interactions with good reproducibility. The

relative standard deviation (RSD) of three identically formed structures was 2.8% for 100 nm, 3.76% for 500 nm nanoparticles, and 5.46% for 2.4 µm microbeads.

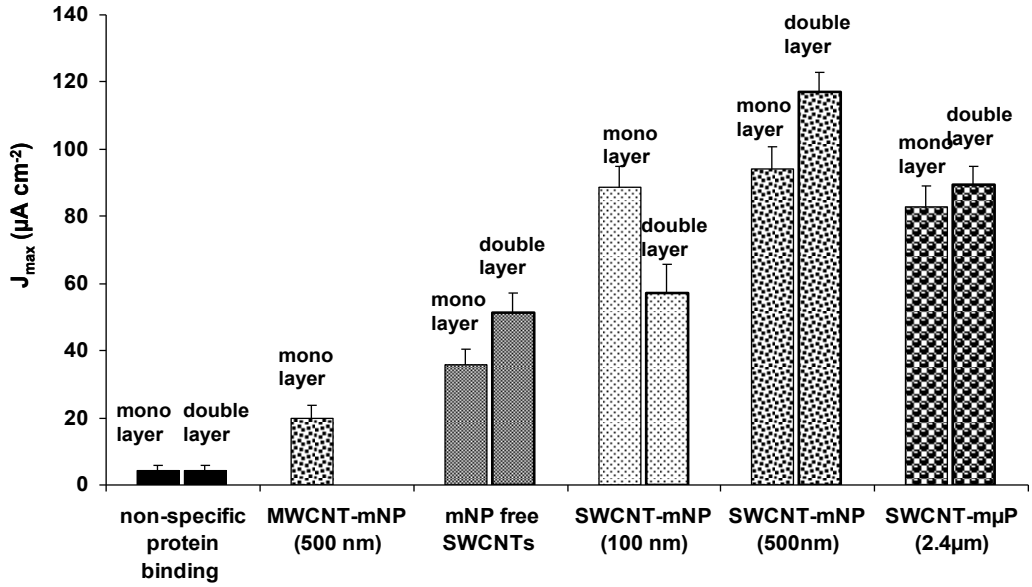

Figure 6. *Histogram for initial evaluation of different mono- and double-layered nanostructured scaffolds using SWCNT, MWCNT and mNP (500 nm), SWCNT and mNP (100 nm and 500 nm), and SWCNT/micro- beads (2.4 µm) along with a control experiment for non-specific binding of HRP labelled secondary antibody on poly(pyrene-β-CD) modified scaffolds without antigen receptor. The current densities were obtained after HRP labelling of the immobilized analyte with the secondary antibody (0.5 mg.mL^{-1}) in PBS containing 2 mmol.L^{-1} hydroquinone and 3 µmol.L^{-1} of H_2O_2. Applied potential: -0.1 V vs Ag/AgCl.*

6.3.1 Anti-CT immunosensor performances using 500 nm particles

To determine the sensitivity to anti CT, the immunosensors were constructed with 500 nm nanoparticles and SWCNTs, and tested with different concentrations of the target analyte (0.01 to 500 µg.mL^{-1}). The calibration curve for the amperometric detection of CT antibody was evaluated for both, single and double-layered constructions. For each analyte concentration, an immunosensor was fabricated under same conditions. The sensitivities were determined as the slope of the linear portion of the calibration curves (**Figure 7**). For single layered scaffold electrodes, a sensitivity of 77.55 ± 1.5 µA.µg^{-1}.mL.cm^{-2} for the linear range between 0.05 - 0.2 µg.mL^{-1} and a detection limit of 50 ng.mL^{-1} could be determined. For the double-layered electrodes, the detection limit (10 ng.mL^{-1}) is clearly improved and also a better sensitivity of 87.77 ± 2.2 µA.µg^{-1}.mL.cm^{-2} for a linear range between 0.01 - 0.2 µg.mL^{-1} is obtained. At lower

antibody concentration, interferences with non-specifically bound HRP labelled secondary antibody appeared.

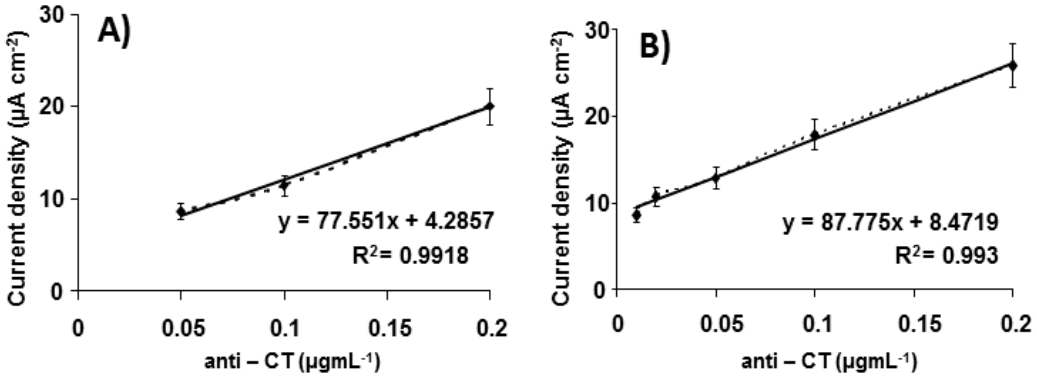

Figure 7*. Linear range of the calibration curves for anti-CT with HRP-assisted amperometric transduction of (A) SWCNT - NP (500 nm) – SWCNT layer, and (B) SWCNT - NP (500 nm) – SWCNT - NP (500 nm) – SWCNT layer.*

Significant features of the HRP immunosensor are summarized in **Table I**.

Table I. *Enzymatic performances of different nanoscaffolds for anti-CT HPR immunosensor.*

Particle size - layers	**CNTs - mono layer**	**CNTs - double layer**	**100 nm-mono layer**	**100 nm-double layer**	**500 nm-mono layer**	**500 nm-double layer**	**2.4 µm - mono layer**	**2.4 µm-double layer**
Current density: J_{max} ($\mu A.cm^{-2}$)	34.3± 0.3	48.5± 0.8	87.5± 1.7	57.1± 0.9	93 ± 2.3	117.1± 2.5	83.2± 1.5	89 ± 2.7
Sensitivity ($\mu A.\mu g^{-1}.mL.cm^{-2}$)	-	-	-	-	77.5	87.8	-	-
Detection limit ($ng.mL^{-1}$)	-	-	-	-	50	10	-	-

6.4 Anti-CT antibody detection using GOx for amperometric transduction

Since the double layer scaffolds presented superior performance than mono layer scaffolds in terms of sensitivity, they were further evaluated for amperometric detection of anti-CT (500 $\mu g.mL^{-1}$) using GOx as enzymatic marker for the detection of anti-CT. The detection of anti-CT was achieved using a sandwich immunoassay through the immobilization of biotinylated cholera toxin B subunit, as the bio-recoginition layer onto the poly(pyrene β-

CD) coated nanostructured electrodes by affinity interactions [5]. The analyte (anti-CT) was detected through enzymatic marker GOx-CD conjugated to biotinylated IgG antibodies (**Figure 8**).

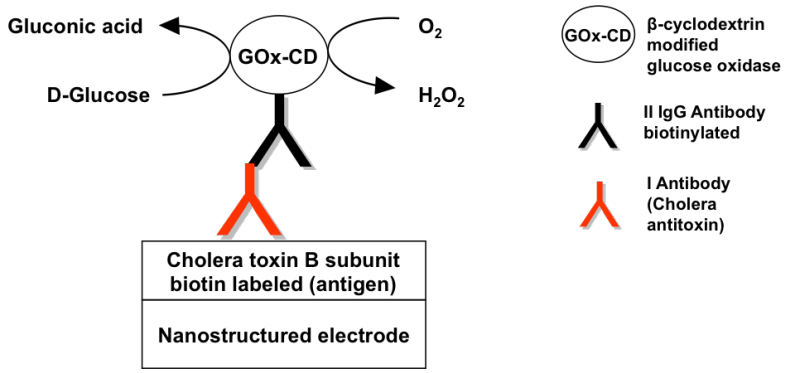

Figure 8. *Amperometric immunosensor set-up using poly(pyrene β-CD)coated nanostructured electrode and GOx-CD as enzymatic marker for the detection of cholera antitoxin (anti-CT).*

The amperometric transduction of an immunoreaction consists in the post-labelling of the detected target (here, anti-CT) by an enzyme (here, GOx) able to catalyze the production or the consumption of electroactive species. Electrodes were modified in the same manner as for HRP immunosensor on the platinum electrodes (Φ = 2 mm). β-cyclodextrin modified glucose oxidase (GOx-CD) was immobilized on the nanotube – nanoparticle assembly and the resulting glucose sensor was calibrated with amperometric measurements. As described before, GOx catalyses the oxidation of glucose to gluconolactone with the concomitant reduction of oxygen into hydrogen peroxide. H_2O_2 is then oxidized at the underlying Pt-electrode at 0.6 V *vs* Ag/AgCl, leading to current increase, which intensity is proportional to the amount of immobilized enzyme and hence to the immobilized amount of target.

Figure 9 shows the histogram obtained by measuring the maximum current density of different scaffolds, which are related to the amount of immobilized antibody (anti-CT) in presence of glucose, along with the blind experiment performed for non-specific binding of GOx-CD labelled secondary antibody without antigen receptor on polypyrene β-CD modified SWCNTs scaffolds.

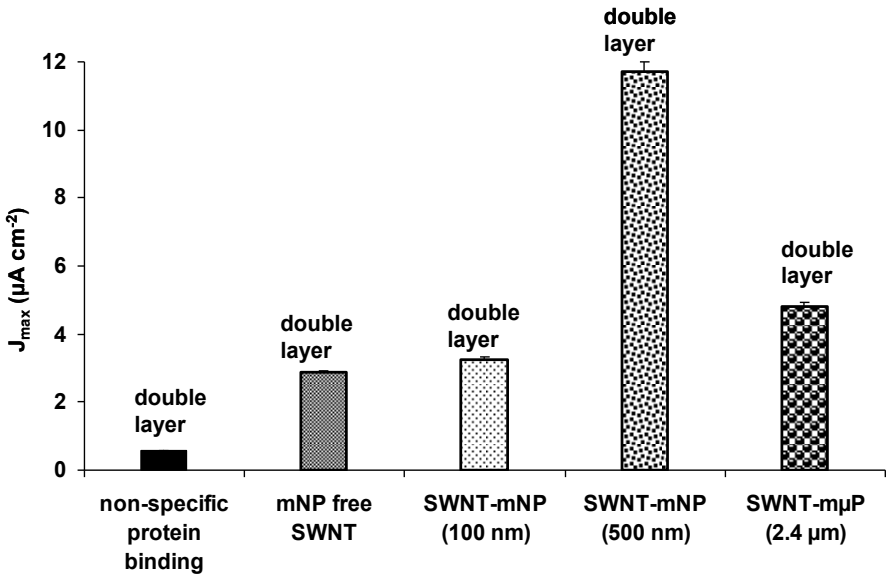

Figure 9. *Histogram for initial evaluation of different double-layered nanostructured scaffolds using SWCNT, SWCNT and mNP (100 nm and 500 nm), and SWCNT/micro-beads (2.4 µm) along with a control experiment for non-specific binding of GOx-CD labelled secondary antibody on poly(pyrene-β-CD) modified scaffolds without antigen receptor. The current densities were obtained after GOx-CD labelling of the immobilized analyte with the secondary antibody (500 µg.mL^{-1}) in 0.1 mol.L^{-1} PBS containing glucose (0.3 mol.L^{-1}). Applied potential: 0.6 V vs Ag/AgCl.*

The change in maximum current density for non-specific binding of antibody represents an error of 5% compared to specific immune interactions. The comparison of the measured current densities of various scaffolds, clearly shows that the most sensitive amperometric immunosensor was based on the nanoscaffold constructed with 500 nm nanoparticle with higher maximum current density and sensitivity values (11.71 µA.cm^{-2}, 116.2 µA.L.mol^{-1}.cm^{-2}), compared to microbeads (4.8 µA.cm^{-2}, 29.7 µA.L.mol^{-1}.cm^{-2}) and 100 nm (3.2 µA.cm^{-2}, 47.44 µA.L.mol^{-1}.cm^{-2}). Again, scaffold containing only nanotubes (2.8 µA.cm^{-2}, 22.7 µA.L.mol^{-1}.cm^{-2}), had lowest current density and sensitivity but comparable to that of microbeads.

It's evident that there is again a significant increase in the performance of immunosensor constructed with 500 nm NPs scaffolds, with optimal pore sizes to immobilize large number of bioreceptors which are several hundred nanometers in size and even, further allows unhindered diffusion of the H_2O_2 to the electrode surface. Significant features of the GOx immunosensor are summarized in **Table II**.

Table II. *Enzymatic performances of different nanoscaffolds for anti-CT GOx immunosensor.*

Particle size - layers	**CNTs - double layer**	**100 nm-double layer**	**500 nm-double layer**	**2.4 µm-double layer**
Current density: J_{max} ($\mu A.cm^{-2}$)	2.8 ± 0.8	3.2 ± 0.9	11.71 ± 2.5	4.8 ± 2.7
Sensitivity ($\mu A.L.mol^{-1}.cm^{-2}$)	22.7	47.44	116.2	29.7

6.5 Assessment of the scaffolds with different particle sizes for enzymatic glucose detection

For comparison, the aforementioned constructions using different NP sizes were also used for enzymatic glucose biosensing. Biotinylated glucose oxidase (GOx-B) was immobilized on the nanotube – nanoparticle assembly and the resulting glucose sensor was calibrated with amperometric measurements. The biosensor set-up was constructed by depositing single and double layered structures of nanotubes and nanoparticles of different sizes on the Pt-electrodes functionalized with pyrene-β-CD (as discussed earlier) and then used for the amperometric measurements. **Figure 10** presents the histogram of recorded J_{max} values in presence of 70 $mmol.L^{-1}$ glucose.

For the enzymatic glucose sensor, 100 nm magnetic particles were found to be the optimal mNP size for the double-layer setup with an average maximum current density of 41.7 ± 0.7 $\mu A.cm^{-2}$. By using the same procedure for scaffold construction, the maximum current density decreased with increasing particle size from 24.4 ± 0.5 $\mu A.cm^{-2}$ using 500 nm particles to 16.9 ± 0.5 $\mu A.cm^{-2}$ using 2.4 µm microbeads. The 100 nm nanoparticle/nanotube scaffolds, both the mono and double layer have the highest maximum current density (J_{max}) and hence lead to the highest amount of enzyme that can be immobilized onto the surface. The values of J_{max} increased with the decrease in the size of particles, and increase in the scaffold levels. This indicates that the pore sizes created using 100 nm NPs allow unhindered diffusion of small glucose substrate and hence, thus produced H_2O_2 to the underlying electrode surface.

The results indicate that the coating based on 100 nm beads not only allows an excellent immobilization of the enzyme but even a better fixation than other configurations. The fact that the immunosensor configuration with 100 nm mNPs was not the best may indicate that

the created pores are sufficient for the diffusion of GOx but after its anchoring, the remaining space is not sufficient for the subsequent anchoring of other proteins.

This demonstrates the flexibility of the developed approach, which can be adjusted and be optimized to the size of both the bioreceptor unit and the analyte (small molecules or biomacromolecules). A convincing reproducibility was also obtained for the enzyme biosensor configuration with RSDs of 1.7% for 100 nm, 2.2% for 500 nm nanoparticles, and 2.9% for 2.4 µm microbeads, evaluating three identically formed structures. Significant features of the glucose biosensor are summarized in **Table III.**

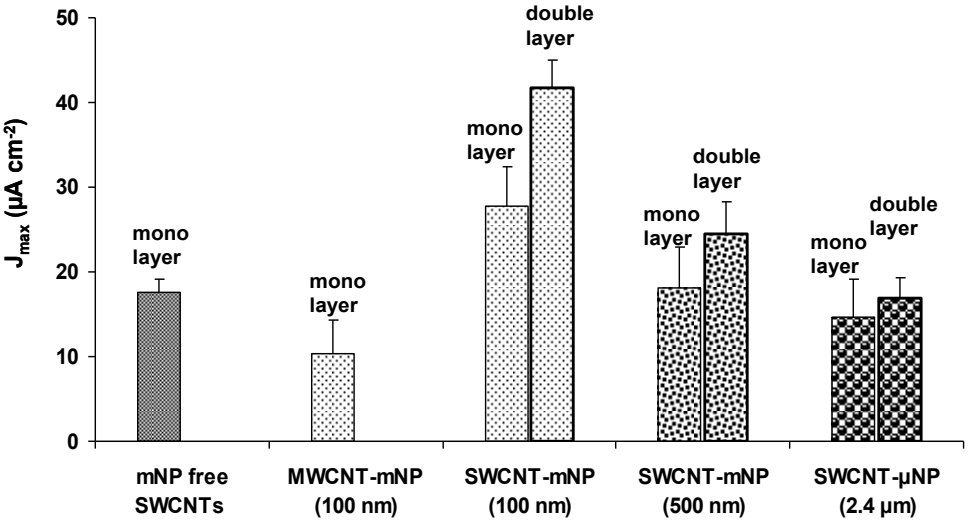

Figure 10. *Histogram of the measured J_{max} values at 70 mmol.L^{-1} containing glucose solution obtained with different mono-and double-layered scaffolds on Pt-electrodes using SWCNT, SWCNT and mNP (100 nm and 500 nm) and SWCNT/micro-beads (2.4 µm) along with control experiment performed with mono-layered MWCNT and mNP (100 nm) scaffolds. Applied potential: 0.6 V vs Ag/AgCl in 0.1 mol.L^{-1}PBS .*

Table III. *Enzymatic performances of different nanoscaffolds for Glucose biosensor.*

Particle size - layers	CNTs - mono layer	CNTs - double layer	100 nm-mono layer	100 nm-double layer	500 nm - mono layer	500 nm-double layer	2.4 µm - mono layer	2.4 µm-double layer
Current density: J_{max} (µA.cm^{-2})	-	17.6 ± 0.3	27.8 ± 0.8	41.7 ± 0.7	18.1 ± 0.8	24.4 ± 0.5	14.6 ± 1.0	16.9 ± 0.5
Sensitivity (mA.L.mol^{-1}.cm^{-2})	-	1.0	1.9	3	1.4	4.5	0.4	0.5

6.6 Conclusion

3D nanostructured scaffolds made with "as received" commercial HiPCO® SWCNTs and magnetic nanoparticles (mNPs) with different sizes were constructed on transducer surfaces using a simple layer-by-layer process for high performance immunosensors. The iron nanoparticle impurity in HiPCO® SWCNTs was used as anchor points to retain randomly mNPs. The proof of concept for their application in biosensing has been shown by enzymatic glucose detection. While both, monolayer and double layer scaffolds containing 100 nm particles were found to meet the desirable sensitivity for this enzyme biosensors, scaffolds embedding 500 nm mNPs, presented the highest anti-CT immunosensors performance compared to other constructions using either smaller or bigger particle sizes. Therefore, the vacancies created with 500 nm mNPs seem to present the most suitable pore size for the permeation of the analyte and for HRP labelled secondary antibody. By using the nanoparticle size of 500 nm, a detection limit of 10 $ng.mL^{-1}$ and a sensitivity of 87.77 $\mu A.\mu g^{-1}.mL.cm^{-2}$ towards anti-CT could be reached. This is by far the highest sensitivity for anti-CT immunosensors compared to amperometric transduction [4] or ELISA [18]. It has to be noted that the used commercialized mNPs are polydisperse with average particle sizes. Together with the inhomogeneous deposition of the mNPs on SWCNTs, pore sizes from several nanometers to several micrometers were observed. This allows on the one hand unhindered diffusion of all biomolecules throughout the structure to the more densely packed anchor groups and receptor units. Nonetheless, these randomly assembled structures shows as a whole good reproducibility for all evaluated setups. One could therefore take advantages of the approach developed within this work, where the proof of concept has been shown by enzymatic glucose and anti-CT detection, to customize any type of bioanalytical or bioenergy devices by tuning mNP sizes [Manuscript under revision].

References

1. A. Walcarius, S. D. Minteer, J. Wang, Y. Lin, A. Merkoci, Journal of Materials Chemistry B 2013, 1, 4878.
2. Z. Dai, H. Ju, TrAC, Trends Anal. Chem. 2012, 39, 149.
3. C. A. Marquette, L. J. Blum, Biosens. Bioelectron. 2006, 21, 1424.
4. R. E. Ionescu, C. Gondran, S. Cosnier, L. A. Gheber, R. S. Marks, Talanta 2005, 66, 15.

5. H. Ju, X. Zhang, J. Wang, in NanoBiosensing, Springer New York, 2011, pp. 425.
6. M. Holzinger, R. Haddad, A. Maaref, S. Cosnier, J. Nanosci. Nanotechnol. 2009, 9, 6042.
7. R. Haddad, S. Cosnier, A. Maaref, M. Holzinger, Analyst 2009, 134, 2412.
8. Y. Chen, Z. Iqbal, S. Mitra, Adv. Funct. Mater. 2007, 17, 3946.
9. I. W. Chiang, B. E. Brinson, A. Y. Huang, P. A. Willis, M. J. Bronikowski, et al., J. Phys. Chem. B 2001, 105, 8297.
10. V. Georgakilas, D. Voulgaris, E. Vazquez, M. Prato, D. M. Guldi, et al., J. Am. Chem. Soc. 2002, 124, 14318.
11. E. Vazquez, V. Georgakilas, M. Prato, Chem. Commun. 2002, 2308.
12. J. G. Wiltshire, A. N. Khlobystov, L. J. Li, S. G. Lyapin, G. A. D. Briggs, et al., Chem. Phys. Lett. 2004, 386, 239.
13. B. Bittova, J. P. Vejpravova, M. Kalbac, S. Burianova, A. Mantlikova, et al., The Journal of Physical Chemistry C 2011, 115, 17303.
14. R. Haddad, S. Cosnier, A. Maaref, M. Holzinger, Sensor Lett. 2009, 7, 801
15. R. Haddad, M. Holzinger, R. Villalonga, A. Neumann, J. Roots, et al., Carbon 2011, 49, 2571.
16. M. Holzinger, M. Singh, S. Cosnier, Langmuir 2012, 28, 12569.
17. R. Haddad, M. Holzinger, A. Maaref, S. Cosnier, Electrochim. Acta. 2010, 55, 7800.
18. B. Leshem, G. Sarfati, A. Novoa, I. Breslav, R. S. Marks, Luminescence 2004, 19, 69.

Graphene based Optical Immunosensor

Chapter 7

7.1 Context

Surface plasmon resonance (SPR) biosensors have now established as a central tool for the study of biomolecular interactions, chemical detection, and immunoassays in various fields. Immunochemical methods like ELISA, spectroscopy and chromatography are the most used in antigen-antibody detection. Different methods have been linked, e.g. liquid chromatography and mass spectrometry (LC-MS), in order to detect as low concentrations as possible. SPR biosensors offer unparalleled advantages such as label-free and real-time analysis with very high sensitivity. To further push the limits of SPR capabilities, novel SPR configurations and approaches are being actively investigated. However there are limitations involved with optical sensors and conventional SPR biosensors such as low optical sensitivity and poor adsorption of biomolecules on gold resulting in low sensitivity of the device.

Plenty of methods have been employed to enhance the sensitivity of SPR biosensor, mainly focusing on the improvement of modification of sensor surface. For example, magnetic microbeads [1], Ag film [2], Au/Ag alloy nanocomposites [3] and thin films of titanium dioxide [4] have been used to modify the sensor surface. At the same time, there is a growing interest in the applications of carbon nanomaterials, notably carbon nanotubes and graphene, for biosensing [5].

Graphene as discussed in **Chapter 1**, a single sheet of carbon atoms in a hexagonal lattice (**Figure 1**), has attracted great interest in various fields [6,7]. The recent development of large-scale graphene synthesis and transfer techniques, as well as the structural modification of graphene by chemical or biological molecules, established it as a promising candidate for label-free monitoring methods for chemical or biomolecular interactions [8,9]. Due to its high carrier mobility and zero-band gap characteristics, graphene exhibits unique and desirable optical properties, such as broadband and tunable absorptions [10,11].

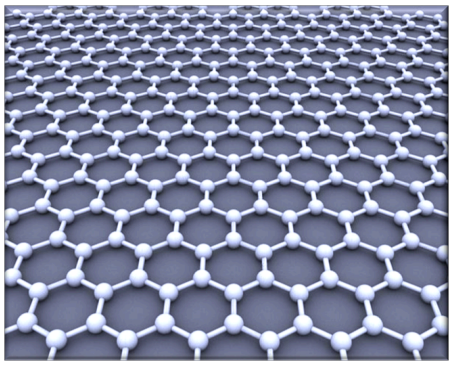

Figure 1. *Structure of Graphene.*

The unique surface physicochemical characteristics of graphene make it very attractive particularly for biosensing. This graphene based SPR biosensor can be quite easily realized due to the similarity of graphene's electronic and surface properties to carbon nanotubes. Through the π-stacking interactions between its two-dimensional hexagonal cells and the carbon-based ring structures widely present in organic and biological molecules, graphene can strongly and stably adsorb biomolecules [12]. Hence the incorporation of graphene into SPR biosensors structure can substantially simplify the bioreceptors linking to the sensor surface. Moreover, graphene is extremely thin and, due to the ease of functionalization, can act as simple double face scotch tape.

To assess the sensitivity of the graphene based optical sensor, it is necessary to know the optical property of graphene. In **Chapter 1**, optical property of graphene was reviewed and it was shown that the light transmittance through monolayer graphene is about 97.7 % [13]. It implies that a one-atom-thick graphene layer will absorb only 2.3 % of incident light. The simulated transmittance is also found to decrease with increasing graphene layers and each additional graphene layer absorbs another 2.3 %. In fact, it has been theoretically predicted that the incorporation of a single layer of graphene adds 2.5 % to the optical sensitivity of SPR sensors [14]. Improvement results from the optical property of graphene. At λ_o = 633 nm, graphene is a dielectric material, thus coating of the gold surface with a dielectric film (graphene) will change the power flow in different layers and modify the field of the surface plasmons [15]. Thus, sensitive and real-time monitoring of the refractive index using a graphene based optical sensor can be envisioned with high sensitivity and excellent stability, the qualities that are all essential for a versatile SPR sensor. The flexibility and ease of functionalization of graphene makes it ideal basis choice for fabricating optical biosensor devices [16].

Since the overall sensitivity of an SPR biosensor is determined by both the intrinsic optical sensitivity of the SPR sensor and the characteristics of the surface functionalization, another alternative approach to improve the sensitivity of SPR biosensor is to functionalize the gold surface with a sensing layer which takes both factors into account. For this purpose, in this chapter we propose to use single layer of graphene sheet transferred onto gold surface functionalized further with electrogenerated thin polymer films or pure π-π stacking of pyrene entities to graphene sheet through its extended π – system.

7.2 Functionalization of graphene modified gold sensing surface

7.2.1. Transfer of graphene layer on gold

The graphene layers were synthesized and characterized at CRANN by the Duesberg Groups at Trinity college, Dublin, Irelandon copper foils by chemical vapor deposition. The copper foil was placed in a quartz chamber and heated to 1035°C using a 2:1 mixture of methane and hydrogen. After the growth, the graphene was transferred using a polymer assisted transfer process. A film of PMMA was spun onto the graphene and the copper was then etched away using a 1 $mol.L^{-1}$ ammonium persulfate solution. The remaining PMMA/graphene film was then floated onto deionised water using a glass slide to rinse away any etchant residue. After the rinse, the graphene was fished onto the gold substrate and allowed to dry. The PMMA is removed by immersion in HPLC acetone. As a result, we have large area of one graphene sheet on 50 nm thick gold disk (NSF 15 from KE instrument BV).

7.2.2 Characterization of graphene by Raman spectroscopy

Figure 2 shows a typical Raman spectrum of single-layer graphene. On SiO2 substrate, D-, G- and 2D peaks appear at approximately 1350 cm^{-1}, 1583 cm^{-1} and 2680 cm^{-1} respectively (**Figure 2B**). The gold substrate spectrum is noisier and has a sloped background due to the metal substrate (**Figure 2B**). The 2D band can be used to determine the number of layer of graphene. The 2D band in the single-layer graphene is much more intense and sharper as compared to the 2D band in multi-layer graphene [17,18]. From these spectrums, we can conclude that the area is mostly monolayer graphene due to the narrow 2D peak and the high 2D/G peak ratio.

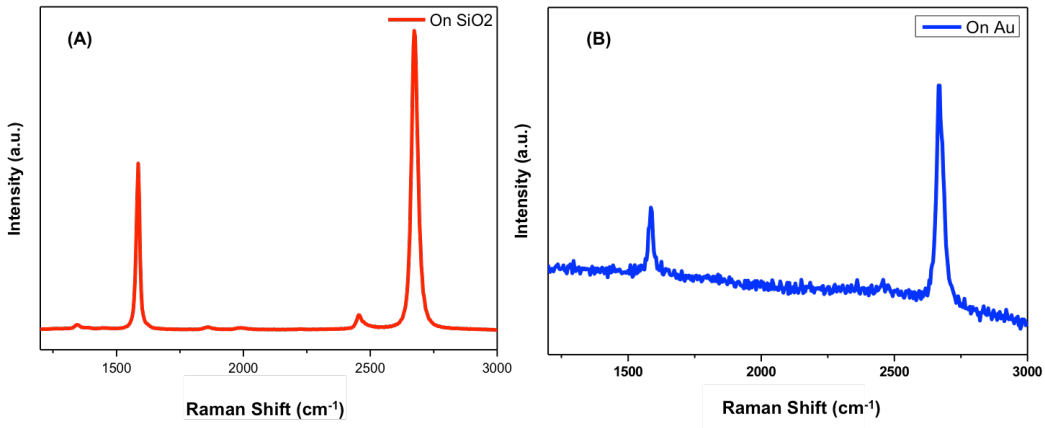

Figure 2. *Raman spectrums of pristine single layer graphene on (A) SiO2 (in red) and (B) gold (in blue) substrates.*

7.2.3 Functionalization of graphene modified gold surface

Effective immobilization of biomolecules on the sensor surface has been considered as one of the most important points in the development for high quality of biosensors. As a matter of fact, one of the first steps in any SPR-based protocol concerns the way that the receptor molecules are anchored onto the SPR surface. The bioreceptors are either physically absorbed or chemically attached onto the sensor surface. The covalent immobilization strategies include chemical reactions such as amine, aldehyde or thiol coupling on previously formed functional self-assembled monolayers [19]. However, covalent immobilization results in the loss of the bioreceptor unit due to its chemical modification. Here we demonstrate a novel approach by using a graphene layer as the SPR bio-interface for the immobilization of biological entities using affinity based systems preserving their activity.

The approach described here exploits the direct electrodeposition or non-covalent functionalization of polymer bearing affinity group onto graphene-gold SPR interfaces. A polypyrrole-NTA film [20] was electrodeposited onto the conventional and graphene-modified gold surface. Conversely, pyrene-NTA film [21] was non-covalently attached to the graphene surface *via* π-π stacking interactions.

The gold slides with or without graphene were first modified with polypyrrole - NTA (2 $mmol.L^{-1}$ in DMF + 0.1 $mol.L^{-1}$ TBAP) using controlled potential electrolysis method. Pyrrole - NTA was polymerized at 0.95 V for different charges 1 $mC.cm^{-2}$, 3 $mC.cm^{-2}$ and 5 $mC.cm^{-2}$ to analyze the sensitivity variation. We make another modification of gold slides with polypyrene

NTA (2 mmol.L^{-1} in DMF + 0.1 mol.L^{-1} TBAP) using electrolpolymerization of pyrene NTA (1 mC.cm^{-2}) at 1.3 V *vs* Ag/Ag^{+}. The unique structure of graphene allows its easy and rapid functionalization. Non-covalent functionalization is particular interesting for the development of graphene based biosensors since the physical properties of the graphene are entirely preserved. For this purpose, pyrene-NTA was non-covalently attached to the graphene by drop-casting 3 µL of 2 mmmol.L^{-1} pyrene-NTA solution in DMF on the graphene and dried under vacuum followed by thorough rinsing with DMF. The deposit was then electropolymerized in a monomer free solution to generate a polymeric monolyaer of polypyrene- NTA by controlled potential electrolysis at 1.3 V *vs* Ag/Ag^{+}.

The resulting coatings of respective polymers were used for the successive attachment of biotinylated biomolecule *via* subsequent coordination of copper (II) ions at the NTA chelate (**Figure 3**) and the biotin groups of biomolecule at the Cu^{2+}–NTA complex [21]. 0.01 mol.L^{-1} of $CuCl_2$ acetate buffer solution (0.1 mol.L^{-1}, pH = 4.8) was used for the chelation procedure.

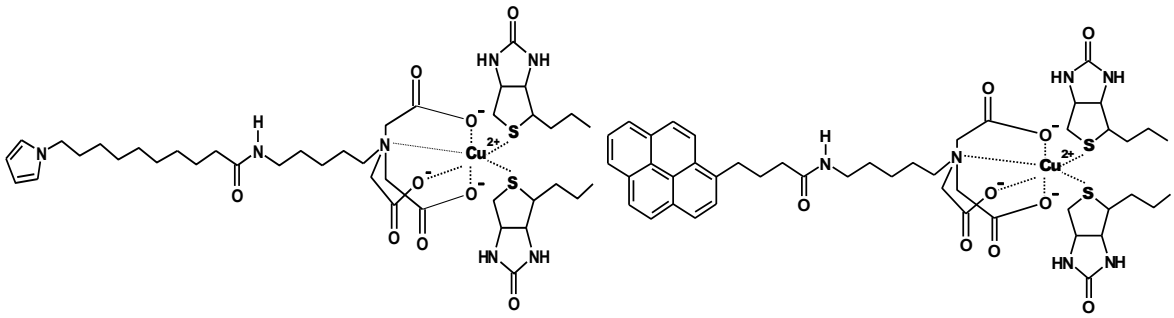

Figure 3. *Structure of (A) pyrrole-NTA and (B) pyrene-NTA, showing NTA/Cu^{2+}/ biotin interaction.*

7.2.4 Characterization of functionalized graphene by optical microscopy

Figure 4 shows laser microscope image of gold disk modified with graphene and graphene further modified with electrogenerated polypyrrole-NTA film (1 mC.cm^{-2}, 0.95 V) along with the height and intensity profiles. As observed, the height profile (in blue) remain same after transfer of graphene and electrodeposition of polymer, while the intensity profile (in green) decreases a little. This confirms that the monolayer of graphene and polymer film is thin enough to to prevent detrimental effects on the plasmonic properties and should allow proper surface chemistry for immobilization of specific bioreceptor.

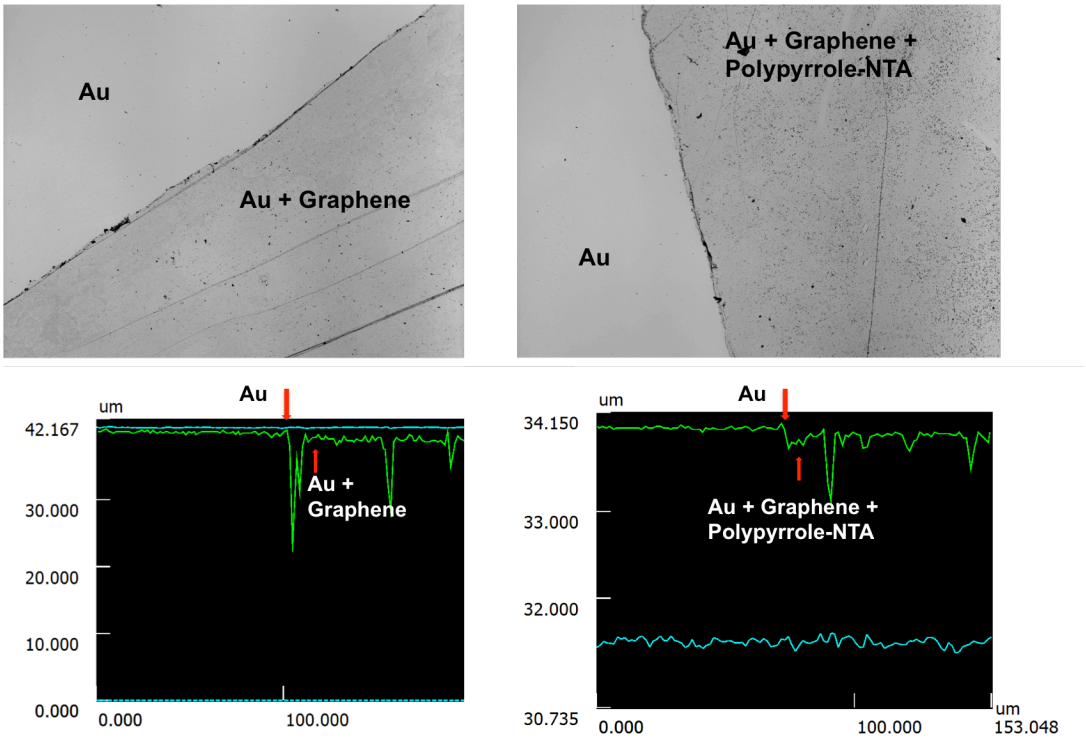

(A) (B)

Figure 4. *Laser microscope images of (A) graphene on gold and (B) graphene on gold modified with polypyrrole-NTA, along with their height (in blue) and intensity (in green) profiles.*

7.3 Detection of Antibody Cholera toxin (Anti-CT)

7.3.1 Immobilization of cholera toxin

Immobilization of bioreceptors on SPR sensors is an essential issue for bioanalytical applications. Direct adsorption of proteins on metal surface results in denaturatation of proteins and loss of their binding activity. Thus, electropolymerized films can act as a solid support for efficient and stable immobilization of the biological macromolecules. We used cholera toxin as immuno-model. The gold/gold-graphene surfaces were functionalized with polypyrrole/pyrene film bearing NTA group. The NTA group form coordination complex with Cu^{2+}, the biotin groups attached to cholera toxin can then coordinate at the Cu^{2+}–NTA complex (**Figure 5**).

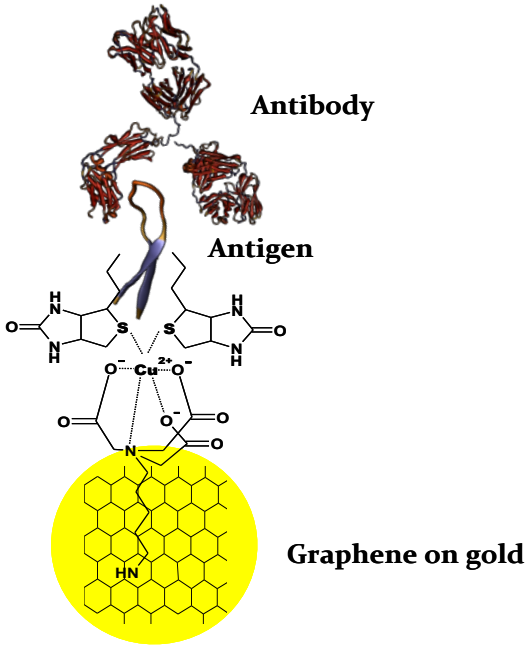

Figure 5. *Schematic representation of graphene modified gold sensing surface functionalized with NTA group coordinated with Cu^{2+}. Biotinylated cholera toxin (antigen) coordinates with Cu^{2+}/NTA complex, onto which the analyte anti-CT (antibody) is immobilized.*

The modified gold slides were incubated with 5 µL of biotinylated cholera toxin (0.1 $mg.mL^{-1}$ in 1 % (w/v) BSA/PBS) for 30 mins at 4°C. The glass slide was then assembled into the Autolab, springle SPR instrument. 90 µL of PBS (10 $mmol.L^{-1}$, pH 7.4) was injected as the baseline solution. The immunoreaction between the biotinylated cholera toxin and anti cholera toxin from rabbit immobilized on the surface was monitored as a shift of angle in real time. Different concentrations of anti-cholera toxin (anti-CT) diluted with PBS were injected into the flow cell over the immobilized antigen surface. Control experiments were performed in the absence of antigen cholera toxin and all the experiments were conducted three times to examine the reliability of the assays.

7.3.2 Polypyrrole – NTA sensing surface

Using the fabricated sensing surfaces, we first examined the optimal conditions for the immobilization of biorecoginition element, different polypyrrole – NTA films were studied depending on the charges employed at a constant potential of 0.95V. Three different charges 1 $mC.cm^{-2}$, 3 $mC.cm^{-2}$, 5 $mC.cm^{-2}$ were used to electrogenerate polymer films of different thicknesses on the gold surface. The eletcrogenerated films were then modified with antigen as described previously and the resulting sensing surfaces were tested using SPR. A

concentration of 35 ng.mL^{-1} of anti-CT was then injected and SPR angle shift of antibody was measured for evidence of the adsorption of antibody on gold surface. The angle of resonance is a function of thickness and the optical properties of the gold and the sensing layer. The response also depends on the refractive index of the bulk solution. There is a linear relationship between the amount of bound material and shift in SPR angle [22]. The SPR angle shifts in millidegrees and is used as a response unit to quantify the binding of macromolecules to the sensor surface. A change of 122 millidegrees (m°) represents a change in surface protein of approximately 1 ng.mm^{-2}, or in bulk refractive index of approximately 10^{-3} [23]. The highest angle shift (213 m°) was observed with film generated with 1 mC.cm^{-2}, and angle shift decreases with the increase in charge for the electrogeneration of polypyrrole-NTA film (**Figure 6**). This behaviour can be attributed to the equation (**1**), where apparent surface coverage of monomer on electrode Γ, is directly related to the charge deposited.

$$\Gamma\ (\text{mol cm}^{-2}) = \frac{Q\ (C)}{nF\ (\text{Cmol}^{-1})\ A\ (\text{cm}^2)} \qquad (1)$$

Q is the charge in Coulombs, n is the number of electrons taking place in polymerization, F is the Faraday's constant and A is the surface area of the electrode. Thus, the results clearly indicate that the most suitable film was developed with minimum charge and was appropriate for SPR sensing.

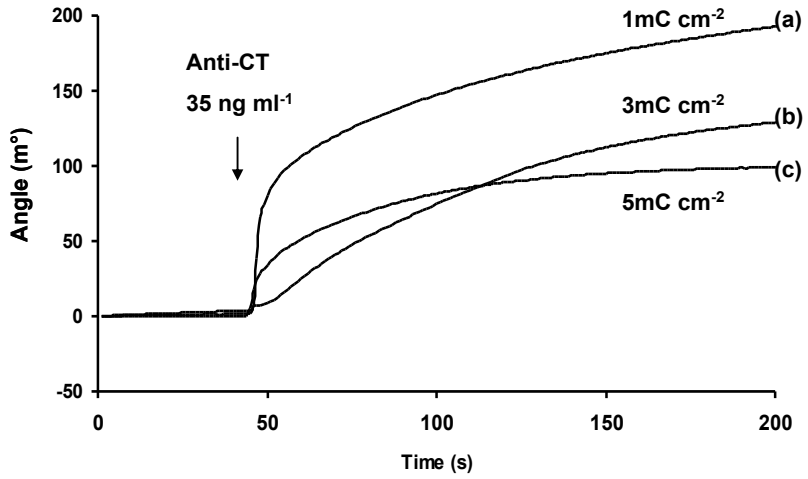

Figure 6. *SPR angle of conventional gold film modified with polypyrrole-NTA by controlled potential electrolysis at 0.95 V at different given charges (a) 1 mC.cm^{-2}, (b) 3 mC.cm^{-2} and (c) 5 mC.cm^{-2} in the presence of 35 ng.mL^{-1} of anti-CT.*

The next step was to employ graphene for the sensitivity enhancement. The polymer film was then electrogenerated on graphene-modified gold disk, and the immunoreaction was measured between antigen and antibody. **Figure 7** shows SPR angle of conventional gold film and graphene modified gold films towards two different concentrations of anti-CT (35 ng.mL^{-1} and 4 ng.mL^{-1}). The graphene modified gold slides had higher sensitivity, yielding a maximum angle shifts of 328° and 75° for concentration of 35 ng.mL^{-1} and 4 ng.mL^{-1} respectively. The high sensitivity is attributed to the better optical properties of graphene modifying the plasmons behavior.

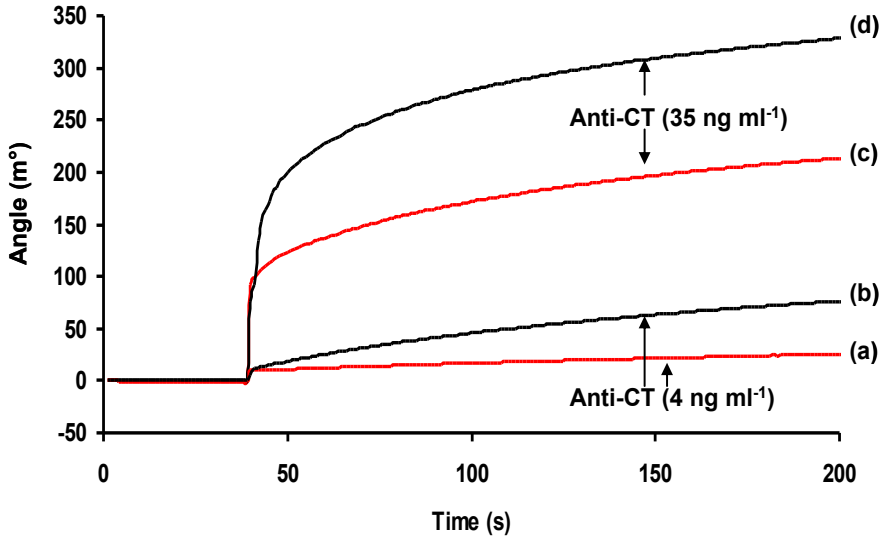

Figure 7. *SPR angle of conventional gold (in red) and graphene modified gold (in black) surfaces functionalized with polypyrrole-NTA by controlled potential electrolysis (0.95 V, 1 mC.cm^{-2}) with two different concentrations of anti-CT. SPR angle shifts (a,b) with 4 ng.mL^{-1} and (c,d) with 35 ng.mL^{-1} of anti-CT.*

Figure 8 shows histograms for the change in reflectivity (%) of conventional and graphene-modified gold sensing surfaces. A 9% increase in reflectivity was recorded with graphene-based SPR biosensor, while for conventional gold surface the reflectivity change was 7%. The control experiment was performed with conventional gold surface in the absence of antigen giving a change of 2% in the reflectivity with 35 ng.mL^{-1} of antibody. The values of angle shift and reflectivity change for different sensing surfaces are summarized in **Table I**.

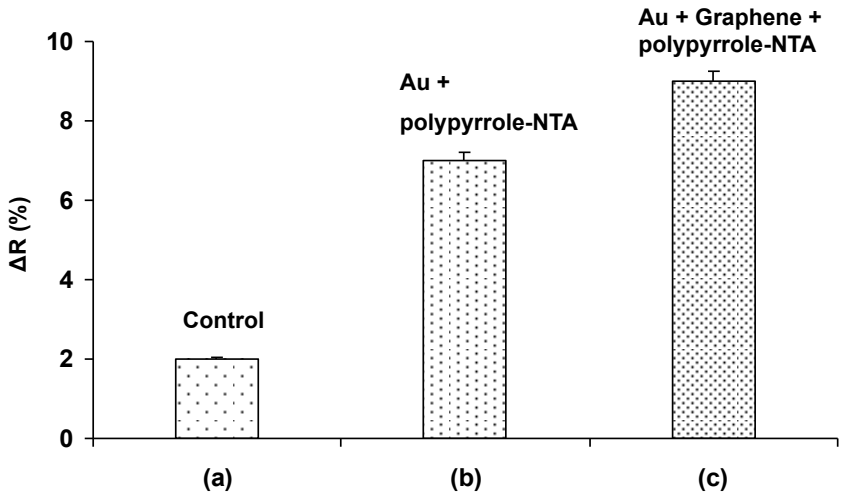

Figure 8. *Histograms for reflectivity change (%) with 35 ng.mL^{-1} of anti-CT for (a) gold surface functionalized with polypyrrole –NTA in absence of antigen as a control experiment; (b) gold surface and (c) graphene-modified gold surface functionalized with polypyrrole –NTA in the presence of antigen.*

Table I. Resonance angle shift and change in reflectivity of different sensing surfaces for 35 ng.mL^{-1} of anti-CT.

Sensing surfaces	Angle shift (m°)	Change in reflectivity (%)
Au-polypyrrole NTA (1 mC.cm^{-2})	196	7
Au-polypyrrole NTA (3 mC.cm^{-2})	138	3.6
Au-polypyrrole NTA (5 mC.cm^{-2})	100	2
Au-Graphene-polypyrrole NTA (1 mC.cm^{-2})	328	9
Au-Graphene-polypyrrole NTA (1 mC.cm^{-2})(without antigen)	80	2

7.3.3 Polypyrene-NTA sensing surface

To compare electrochemical and non-covalent functionalization of pyrene derivative, the conventional and graphene-modified gold surfaces were modified as discussed in **Section 7.2.3**. The sensing surfaces were modified in the same manner as for pyrrole-NTA surface for the coordination of Cu^{2+} and immobilization of biotinylated anti-CT.

A concentration of 35 ng.mL^{-1} of anti-CT was then injected and SPR angle shift of antibody was measured to evidence of the adsorption of antibody on gold surface. **Figure 9a** and **9b** shows SPR angle of conventional gold and graphene-modified gold surface towards 35 ng.mL^{-1} of anti-CT respectively. As expected, the film electrogenerated directly on the graphene-modified gold surface gave a higher angle shift (300 m°) compared to the conventional gold surface (213 m°). On the contrary, the highest angle shift (534 m°) was observed with graphene functionalized non-covalently with pyrene-NTA (**Figure 9c**). The high sensitivity is attributed to the presence of graphene layer, which not only enhances the optical sensitivity but also increases the adsorption of organic molecule due to π-π stacking interactions and minimizes the detrimental effects on plasmonic properties. Hence, it can be concluded that non-covalent functionalization of graphene provides the most sensitive SPR.

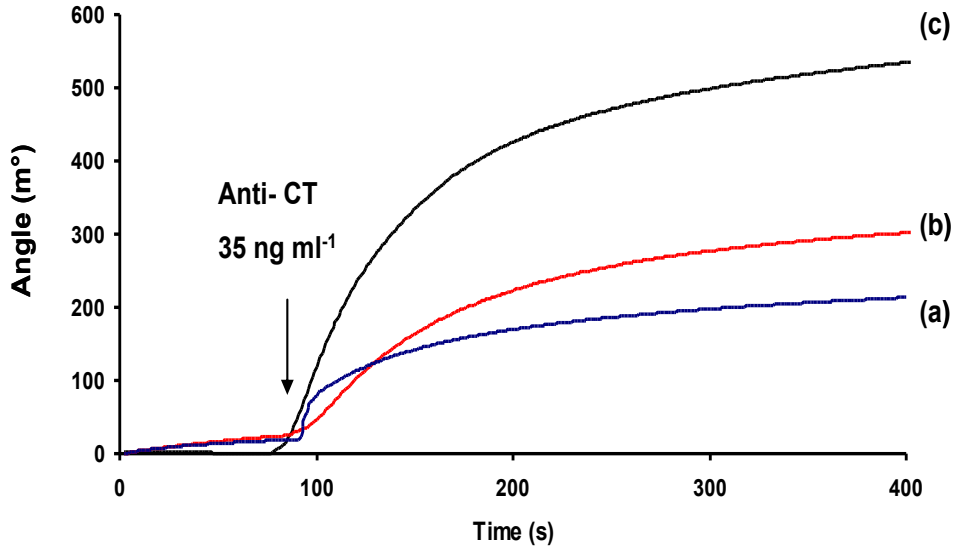

Figure 9. *SPR angle of (a) conventional gold, (b) graphene modified gold surfaces functionalized with polypyrene-NTA by controlled potential electrolysis (0.95 V, 1 mC.cm^{-2}) with 35 ng.mL^{-1} of anti-CT and (c) graphene –modified gold surface functionalized non-covalently by drop-casting technique.*

Figure 10 shows histograms for the change in reflectivity (%) of conventional and graphene-modified gold sensing surfaces. A 12% increase in reflectivity was recorded with non-covalently functionalized graphene-based SPR biosensor. The increase is two-fold in comparison to conventional gold surfaces functionalized with direct electrodeposition. The control experiment in the absensce of antigen gave 2% change in reflectivity for 35 ng.mL^{-1} of antibody. The values of angle shift and reflectivity change for different sensing surfaces are summarized in **Table II**.

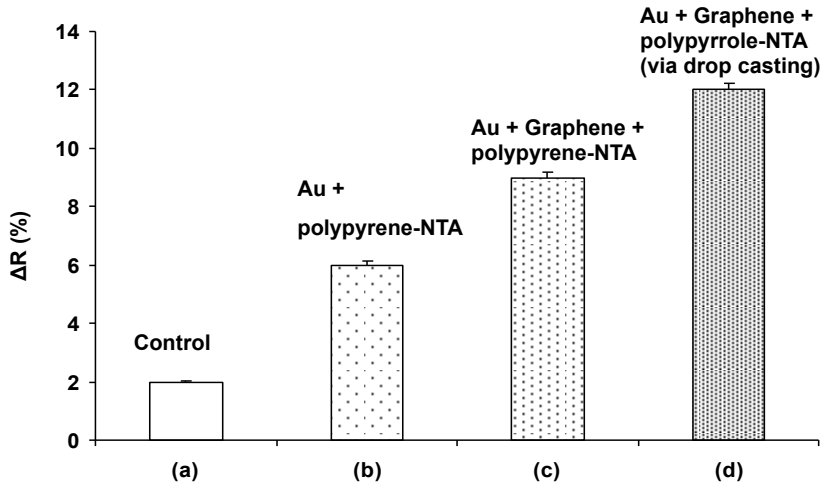

Figure 10. *Histograms for reflectivity change (%) with 35 ng.mL^{-1} of anti-CT for (a) gold surface functionalized with polypyrene –NTA in absence of antigen as a control experiment; (b) gold, (c) and (d) graphene-modified gold surface functionalized by electrodeposition and drop-casting, in the presence of antigen.*

Table II. Resonance angle shift and change in reflectivity of different sensing surfaces for 35 ng mL^{-1} of anti-CT.

Sensing surfaces	**Angle shift (m°)**	**Change in reflectivity (%)**
Au-polypyrene NTA (1 mC.cm^{-2})	213	6
Au-Graphene-polypyrene NTA (1 mC.cm^{-2})	300	8
Au-Graphene-polypyrene NTA (1 mC.cm^{-2}) via drop-casting	534	12
Au-Graphene-polypyrene NTA (1 mC.cm-2) (without antigen)	80	2

7.4 Conclusion

In this chapter, it is concluded that two-fold increase in the sensitivity and nanomolar detection limit can be achieved using graphene-based SPR interface where the specificity is ensured by the functionalization of graphene with conducting polymers. A highly sensitive

graphene based SPR biosensor with good detection limit (4 ng.mL^{-1}) has been successfully developed for label free and real time detection of anti – cholera toxin. Electrodeposition and non-covalent functionalization are the two main approach used for the optimization of highly sensitive sensing surface. The results obtained, clearly indicates the increase in sensitivity when graphene was used as a sensing layer. Graphene, with perfect 2D structure possesses desirable mechanical and chemical stability, while nanometer-order thickness of graphene greatly increases the propagation distance of evanescent waves in liquids, thereby producing a more accurate detection limit [16]. Due to graphene's extended conjugated system, non-covalent functionalization of graphene with pyrene derivatives provides the most sensitive surface for the detection of biomolecule. Therefore, the use of graphene as a sensing layer along with the proposed strategy for the detection of various biomolecules can be intended for sensitive and specific diagnostic applications.

References

1. Y. Sun, Y.P. Bai, D.Q. Song, X.Z. Li, L.Y. Wang, H.Q. Zhang, 23 (2007) 473–478.

2. L.Y. Wang, Y. Sun, J. Wang, X.N. Zhu, F. Jia, Y.B. Cao, X.H. Wang, H.Q. Zhang, D.Q.Song, Talanta 78 (2009) 265–269.

3. J. Wang, D.Q. Song, L.Y. Wang, H. Zhang, H.Q. Zhang, Y. Sun, Sensors Actuators B 157 (2011) 547–553.

4. J. Wang, L.Y. Wang, Y. Sun, X.N. Zhu, Y.B. Cao, X.H. Wang, H.Q. Zhang, D.Q.Song, Colloids and Surfaces B: Biointerfaces 75 (2010) 520–525.

5. Yang, W., Ratinac, K. R., Ringer, S. P., Thodarson, P., Gooding, J. J. and Braet, F., Angew. Chem. Int. Ed. 49(12), 2114 – 2138 (2010).

6. Geim, A. K. Science 324, 1530–1534 (2009).

7. Geim, A. K. and Novoselov, K. S., Nature Mater. 6, 183-191 (2007).

8. Wang, Y., Li, Z., Wang, J., Li, J., & Lin, Y. (2011Trends in biotechnology, 29(5), 205-212.

9. Salavagione, H. J., Díez-Pascual, A. M., Lázaro, E., Vera, S., & Gómez-Fatou, M. A. (2014). Journal of Materials Chemistry A, 2(35), 14289-14328.

10.Bonaccorso, F., Sun, Z., Hasan, T. & Ferrari, A. C. Graphene photonics and optoelectronics. Nat. Photonics 4, 611–622 (2010).

11. Bao, Q. & Loh, K. P. Graphene Photonics, Plasmonics, and Broadband Optoelectronic Devices. ACS Nano 6, 3677–3694 (2012).

12. Song, B., Li, D., Qi, W., Elstner, M., Fan, C. and Fang, H, ChemPhysChem 11(3), 585–589 (2010).

13. R. R. Nair, P. Blake, A. N. Grigorenko, K. S. Novoselov, T. J. Booth, T. Stauber, N. M. R. Peres, and A. K.Geim, Science 320(5881), 1308 (2008).

14. Wu, L., Chu, H. S., Koh, W. S. and Li, E. P., Opt. Express 18(14), 14395-14400 (2010).

15. I. Pockrand, Surf. Sci. 72(3), 577–588 (1978).

16. Xing, F., Liu, Z. B., Deng, Z. C., Kong, X. T., Yan, X. Q., Chen, X. D, & Tian, J. G. (2012). Scientific reports, 2.

17. Wink, T., Van Zuilen, S. J., Bult, A., & Van Bennekom, W. P. (1997). Analyst, 122(4), 43R-50R

18. C. Ferrari, J. C. Meyer, V. Scardaci, C. Casiraghi, M. Lazzeri, F. Mauri, S. Piscanec, D. Jiang, K. S. Novoselov, and S. Roth, A. K. Geim, Phys. Rev. Lett., 2006, 97, 187401.

19. M. A. Pimenta, G. Dresselhaus, M. S. Dresselhaus, L. A.Cancado, A. Jorio, and R. Sato, Phys. Chem. Chem. Phys., 2007, 9, 1276.

20. N. Haddour, S. Cosnier, C. Gondran, J. Am. Chem. Soc. 127 (2005) 5752.

21. Baur, J.; Holzinger, M.; Gondran, C.; Cosnier, S. Electrochem.Commun.2010, 12, 1287–1290.

22. Stenberg, E., B. Persson, H. Roos, and C. Urbaniczky. 1991. J. Coll. Interface Sci. 143: 513-526.

23. Autolab TWINGLE/SPRINGLE Data Acquisition 4.4 User manual

CNT forest as biocathode for Bio-fuel Cells

Chapter 8

8.1 Context

In the field of bio-fuel cell (BFC) engineering, carbon nanotube (CNT) based bioelectrodes are among the best materials for high-performance BFCs for glucose or hydrogen [1]. Carbon nanotube based electrodes have an excellent combination of electrochemical properties and high specific surface area for the efficient wiring of a large amount of enzymes. Although carbon nanotube based electrodes have been studied extensively for electrochemical applications, most of them utilized randomly dispersed nanotubes on the surface. Since the random confinement of the CNTs on to the electrodes causes difficulties in determining the contributions of the ends and the sidewalls of the nanotubes to the electrocatalytic activity of CNTs, thus aligned carbon nanotubes have been proved beneficial for electrochemical and electroanalytical studies.

Carbon nanotube forests are suitable components of various chemical sensors and bio-sensors [2-4] due to large specific surface area of CNT forest and by the ratio of the surface area of CNTs to the substrate surface area. Thus, the aim is to fabricate aligned carbon nanotube arrays having surface area, that are attached to a bulk electrode at one end and thus become nanoscale extensions of the bulk electrode, which are highly electroactive and sufficiently small to penetrate into redox proteins, shortening the distance that electron must tunnel from redox active site of the enzyme to the electrode. Thus, the next generation of biosensors and bioelectronics devices with efficient direct electron transfer between the enzymes and the electrodes can be realized.

8.2 CNT forest

A CNT forest comprises CNTs of different diameter and chirality; a fraction of CNTs exhibit metallic conductivity, while the remaining CNTs behave as semiconductors. A CNT forest can be grown using various versions of the CVD method [5-7]. The CNT forest morphology depends on the substrate properties [8,9]. In the case of strong interaction

between catalyst particles (e.g., Fe/Al_2O_3) and substrate, the particles are immobilized and favor the base growth of CNT forest. Potential application fields of CNT forest are diverse and continuously extending [10,11].

Almost since they were first produced in large quantities [12] carbon nanotubes (CNTs) have been used in electrochemistry [13,14]. A large surface area, good electric conductivity and excellent mechanical properties have made CNTs popular as material for electrode modification. The CNT electrodes can be scaled from a single nanotube [15] to electrodes containing tens of millions of tubes [16]. Carbon nanotubes are also used in electrochemistry as vertically aligned CNT forests, where the nanotubes are oriented perpendicularly to the electrode surface. This arrangement allows for good utilization of the extended surface of the assembly. Furthermore, the arrangement takes advantage of the very fast electron transfer along the CNTs [17].

Electrodes with vertically aligned CNTs (VACNTs) have been shown to support very fast electrochemistry of redox-probes or enzymes [18]. This has led the functionalised VACNT electrodes to be successfully employed in a large number of amperometric sensor applications, e.g. [19-23]. The large effective electrode area also leads to a very large double-layer capacity, which has been used in the electrodes of supercapacitors [24].

This chapter deals with characterization of such aligned carbon nanotubes forest grown by CVD and their application as bio-cathode for bio-fuel cells for the oxygen reduction. An efficient way of immobilizing and wiring a large amount of laccase on non-covalently functionalized nanotube forest to have high performance biocathodes for oxygen reduction by direct electron transfer is described.

8.2.1 Carbon nanotube forest preparation

The CNT forest, received from the Duesberg Group at CRANN, Trinity College in Dublin, Ireland, was grown by CVD at 750°C using a gas mixture of C_2H_2 and H_2 with equal flow rates. The catalyst was a 3 nm layer of CoFe on a layer of Tantalum (Ta) (30 nm) on a substrate of SiO_2. The Ta layer ensured that the CNTs were connected to a conductive substrate. Initially pure H_2 was flowed for 10 minutes to condition the catalyst and then the growth was carried out for 10 minutes with the gas mixture. The carbon nanotube forest can be grown up to several millimetres. An example of 60 µm long forest is shown in **Figure 1**.

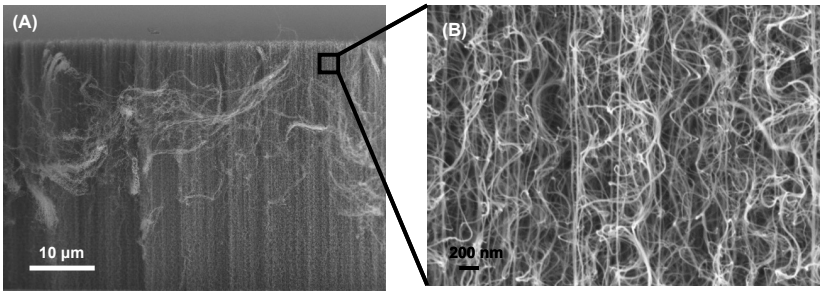

Figure 1. *SEM image of (A) an as-grown carbon nanotube forest and (B) zoom out of nanotube forest.*

8.3 Laccase

Laccase is one of the multicopper oxidoreductase (MCOs) that uses molecular oxygen as the ultimate receptor and catalyzes its reduction to water in neutral or slightly acidic medium. The specific four electron reduction of oxygen of this enzyme relies on its copper based active sites, the T1 and the T2/T3 copper centres.

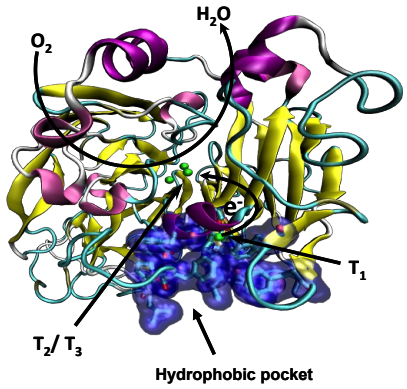

Figure 2. *Schematic representation of laccase structure displaying the copper centres T2/T3 and T1 (green balls) and the hydrophobic pocket.*

A general mechanism involves the T1 copper site accepting electrons from substrates that act as electron donors, then passing those electrons to the T2/T3 tricopper cluster, in which O_2 is coordinated and reduced to water (**Figure 2** shows the coil and ribbon structure of laccase and its active centers for the reduction of oxygen to water). Because the T1 copper site in the enzyme is responsible for electron transfer between substrate and enzyme, its redox potential determines the maximum potential of the enzymatic cathode, and this redox potential can change depending on the source or type of the enzyme [25,26]. Interestingly, the electron tunneling distance from the T1 copper site to the T2/T3 tricopper cluster is ~ 13 A˚, which is the same as the distance between the FAD cofactor in GOx and the surface of the

enzyme. In GOx, the 13 A° distance makes DET extremely difficult, but MCOs can easily transfer electrons across this distance due to a large electron coupling matrix element [27].

It was demonstrated that wiring the T1 centre allows this enzyme to operate at low overpotential [28]. This is the reason why many efforts have been made to control the orientation of surface-confined laccases. Covalent immobilization has also shown to improve stabilization and efficiency of the bioelectrocatalytic enzyme properties. Few years ago, F. A. Armstrong proposed an alternative to covalent immobilization by elegantly taking advantage of the presence of the hydrophobic pocket near the laccase T1 centre to orientate and immobilize the enzyme on pyrolytic graphite which were covalently modified with anthracene groups [29].

8.4 Non-covalent functionalization of CNT forest

Recently, Bourourou *et al.* reported a new compound 1-[bis (2anthraquinonyl)-aminomethyl] pyrene, (pyr-$(AQ)_2$) to non-covalently (π-π stacking interaction) functionalize carbon nanotube electrodes and immobilize and orientate laccase on the nanostructured electrodes (**Figure 3**) [30]. These modified electrodes can integrate with high potential "blue" multicopper enzymes to achieve efficient oxygen reduction. Moreover, owing to the hydrophobic and planar structures of the polycyclic molecules used for laccase anchoring, the latter may stack onto the CNT sidewalls instead of interacting with laccase. Nevertheless, compared to covalent modifications of carbon nanotubes, faster and easier non-covalent methods are interesting because the physical and electronic properties of the CNTs are preserved.

Figure 3. *Schematic representation of non-covalent functionalization of nanotube with 1-[bis(2 anthraquinonyl)aminomethyl] pyrene, [pyr-$(AQ)_2$].*

8.5 SEM characterization of CNT forest

The pristine carbon nanotube forest and carbon nanotube forest functionalized with pyrene derivatives were characterized with SEM. **Figure 4A** represents nanotube forest without functionalization. After the dip coating of nanotube forest with pyrene derivative dissolved in NMP followed by electropolymerization in monomer free PBS solution, 0.1 mol.L^{-1}, (pH = 5.0), the nanotube forest was nicely covered with thin layer of polypyrene (**Figure 4B**).

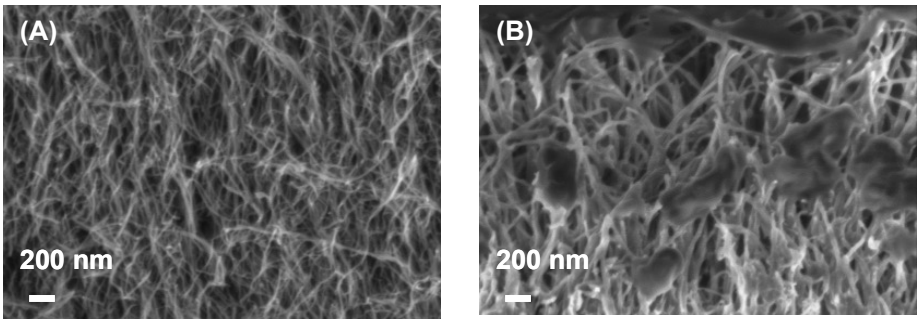

Figure 4. *SEM image of (A) pristine carbon nanotube forest, and (B) nanotube forest after incubation in a solution of polypyrene derivative in NMP.*

8.6 Electrochemical characterization of non-covalently functionalized CNT forest

Functionalization of CNT forest through π-stacking interactions with pyr-$(AQ)_2$ was achieved by incubating the CNT forest electrodes in solution of 2 mmol.L^{-1} pyr-$(AQ)_2$ in NMP for 60 minutes. The cyclic voltammogram of anthraquinone-functionalized CNT forest electrodes was recorded in 0.1 mol.L^{-1}, PBS (pH = 5.0) electrolyte solution (**Figure 5**).

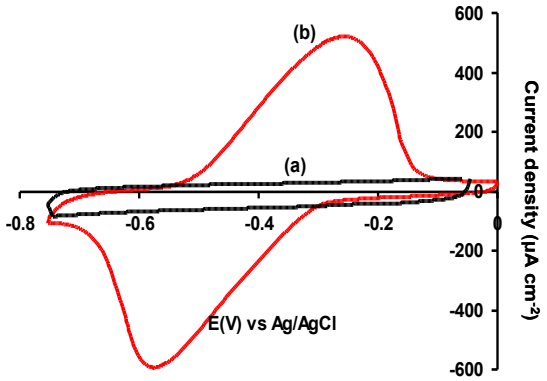

Figure 5. *Cyclic voltammograms of pristine carbon nanotube forest (a) and nanotube forest functionalized with pyr-$(AQ)_2$(b) in PBS (0.1 mol.L^{-1}, pH 5.0). Scan rate, v = 0.02 V s^{-1}.*

A reversible peak system was observed for pyr-$(AQ)_2$.This redox process was attributed to the two overlapping two-electron reductions of the two anthraquinone groups, and it thus exhibits a relatively large ΔE_p value of 200 mV.

The benefit of anthraquinone-functionalized nanotube forest electrodes is underlined in terms of catalytic oxygen reduction currents and long-term stability. The unmodified CNT forests and anthraquinone-functionalized CNT forests forests were incubated in a 5 $mg.mL^{-1}$ solution of laccase in PBS for 48 hours followed by washing with PBS. Cyclic voltammetry scans were performed for the two electrodes under argon and constant oxygen flow at a scan rate of 0.01 $V.s^{-1}$ (**Figure 6**). Under argon, no electrocatalytic activity was observed. Under oxygen, both electrodes exhibit an onset potential of 0.58 V, closely matching the redox potential of the T1 centre of Trametes versicolor laccase.

All these electrodes exhibit an electrocatalytic reduction wave, confirming direct electron transfer (DET) between CNT forest and laccase (Lac). These catalytic currents account for the electrocatalytic properties of laccase directly wired on the CNT forest surface. When CNT forest was first incubated with the anthraquinone-pyrene derivative (pyr-AQ_2), the maximum current density increased approximately four times compared to laccase non-specifically adsorbed on CNT forest (0.38 $mA.cm^{-2}$), reaching 0.9 $mA.cm^{-2}$.

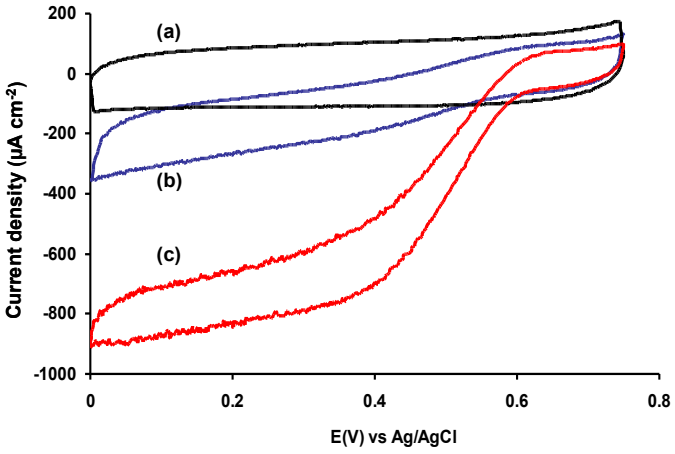

Figure 6. *Cyclic voltammograms of laccase-functionalized carbon nanotube forest electrodes. a) CNT forest/Lac under argon (in black), b) CNT forest/Lac (in blue) and c) CNT forest/ pyr-$(AQ)_2$/Lac under oxygen purging (in red) in 0.1 $mol.L^{-1}$ PBS (pH 5.0); scan rate, v = 0.01 $V.s^{-1}$, 25 °C.*

The fact that maximum current densities were obtained for pyrene bearing two anthraquinone groups is likely due to the higher availability of the anthraquinone groups at the electrode surface for interaction with the laccase. The possible π-stacking of both pyrene and anthraquinone group may lead to immobilized compounds unavailable for the subsequent anchoring of laccase. In the case of pyr-$(AQ)_2$, at least one anthraquinone group cannot stack on the nanotube surface due to steric hindrance of the molecule (**Figure 7**) [30].

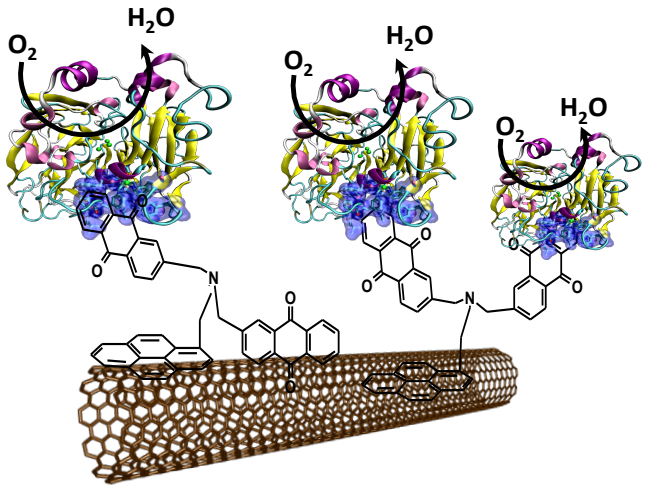

Figure 7. *Schematic representation of possible π-stacking interactions between anthraquinone and nanotube of CNT forest, using pyr-$(AQ)_2$.*

Zloczewska *et al.* employed vertically aligned carbon nanotube (VACNT) film electrodes for bioelectrocatalytic dioxygen reduction and found very high non-mediated catalytic dioxygen reduction current 0.4 $mA.cm^{-2}$ using VACNTs functionalized with 1-pyrenesulfonic acid and laccase embedded in a silicate matrix [31]. Minteer and co-workers covalently modified MWCNTs with anthracene groups and reached maximum currents of 0.14 $mA.cm^{-2}$ for direct oxygen reduction [32]. Bilewicz and co-workers obtained 0.24 $mA.cm^{-2}$ by covalent modification of single-walled CNTs with a diazonium derivative of anthraquinone [33].

In our strategy, non-covalently functionalization of nanotube forest helps in fixing laccase preserving its bioactivity and the anthraquinone plays the major role to guide the enzyme efficiently on the electrode surface by interacting with the hydrophobic pocket near the T1 copper centre. High-performance biocathode thus can be obtained using nanotube forest enabling efficient immobilization of enzymes.

We also investigate the long-term stability of the electrodes by performing one-hour discharge at 0.3 V using chronoamperometry over several weeks (**Figure 8**). The CNT forest functionalized with pyr-$(AQ)_2$ and laccase exhibit excellent stability over continuous discharge.

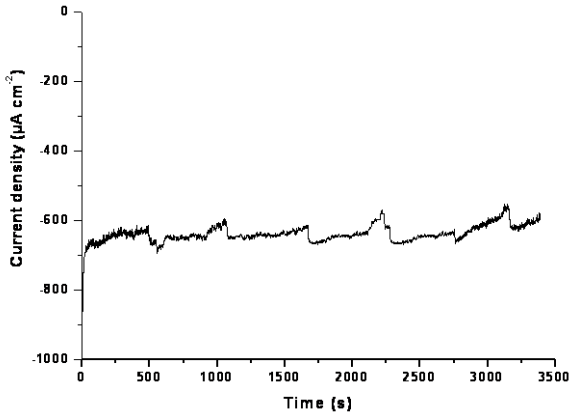

Figure 8. *Chronoamperometric response for a CNT forest/pyr-$(AQ)_2$/Lac. E_p= 0.3 V (vs Ag/AgCl) in 0.1 mol.L^{-1} PBS solution (pH 5.0) put under continuous oxygen purging at 25 °C.*

A 25 % loss of the catalytic activity for CNT forest/pyr-$(AQ)_2$/Lac electrode during each week (**Figure 9**). The decrease likely arises from desorption of both weakly adsorbed pyrene molecules and enzymes. The preparation of these prototype CNT-forest biocathodes is easy, and enzyme layers are stable for weeks.

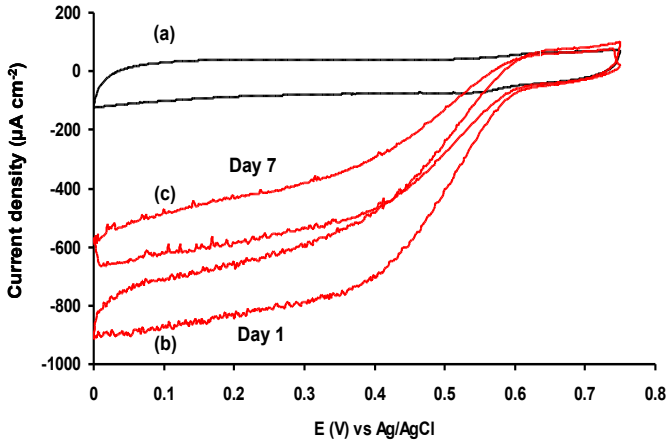

Figure 9. *Cyclic voltammograms of laccase-functionalized carbon nanotube forest electrodes. a) CNT forest/Lac under argon, b) CNT forest/ pyr-$(AQ)_2$/Lac (Day 1), and c) CNT forest/ pyr-$(AQ)_2$/Lac under oxygen purging after one week (Day 7) in 0.1 mol.L^{-1} PBS (pH 5.0); scan rate, v = 0.01 V.s^{-1}, 25 °C.*

8.7 Conclusion

In conclusion, we have shown that non-covalently functionalization of vertically aligned CNT forests with anthraquinone derivatives bearing pyrene groups enhance the direct electrical communication from the electrode the T1 copper site of the enzyme. This novel strategy improves the bioelectroctalytic reduction of dioxygen along with the increase in the stability of the electrocatalyst which always remain a weak point in most of the biological fuel cells reported.

References

1. M. Holzinger, A. Le Goff and S. Cosnier, Electrochim. Acta 2012, 82, 179–190.
2. C Wei, L Dai, A Roy, T B Tolle J. Am. Chem. Soc. 128 1412 (2006)
3. J J Gooding, R Wibowo, J Q Liu,WYang, D Losic, S Orbons, F J Mearns, J G Shapter, D B Hibbert, J. Am.Chem. Soc. 125 9006 (2003)
4. Sang Nyon Kim, James F. Rusling, and Fotios Papadimitrakopoulos, Adv. Mater. 2007, 19, 3214–3228
5. Q Zhang,WZhou,WQian, R Xiang, J Huang, D Wang, F Wei J. Phys. Chem. C 111 14638 (2007)
6. M Pinault, V Pichot, H Khodja, P Launois, C Reynaud, M Mayne-L'Hermite, Nano Lett. 5 2394 (2005)
7. R Xiang, G Luo, Z Yang, Q Zhang,WQian, F Wei, Nanotechnology 18 415703 (2007)
8. P B Amama, C L Pint, S M Kim, L McJilton, K G Eyink, E A Stach,R H Hauge, B Maruyama, ACS Nano 4 895 (2010)
9. L Zhu, D W Hess, C-P Wong J. Phys. Chem. B 110 5445 (2006)
10. C C Lin, I C Leu, J H Yen, M H Hon Nanotechnology 15, 176 (2004)
11. J M Schnorr, T M SwagerChem. Mater. 23 646 (2011)
12. T.W. Ebbesen, P.M. Ajayan, Nature 358 (1992) 220.
13. J.M. Planeix, N. Coustel, B. Coq, V. Brotons, P.S. Kumbhar, R. Dutartre, P. Geneste, P. Bernier, P.M. Ajayan, J. Am. Chem. Soc. 116 (1994) 7935.
14. P.J. Britto, K.S.V. Santhanam, P.M. Ajayan, Bioelectrochem. Bioenerg. 41 (1996) 121.
15. J.K. Campbell, L. Sun, R.M. Crooks, J. Am. Chem. Soc. 121 (1999) 3779.
16. J. Koehne, J. Li, A.M. Cassell, H. Chen, H.T. Ng, J. Han, M. Meyyappan, J. Mater. Chem. 14 (2004) 676.
17. J. Liu, A. Chou, W. Rahmat, Michael N. Paddon-Row, J.J. Gooding, Electroanalysis17 (2005) 38.

18. J.J. Gooding, R. Wibowo, J. Liu, W. Yang, D. Losic, S. Orbons, F.J. Mearns, J.G.Shapter, D.B. Hibbert, J. Am. Chem. Soc. 125 (2003) 9006.

19. J.J. Gooding, A. Chou, J. Liu, D. Losic, J.G. Shapter, D.B. Hibbert, Electrochem.Commun. 9 (2007) 1677.

20. Q. Yang, Y. Qu, Y. Bo, Y. Wen, S. Huang, Microchim. Acta 168 (2010) 197.

21. W.-D. Zhang, J. Chen, L.-C. Jiang, Y.-X. Yu, J.-Q. Zhang, Microchim. Acta 168 (2010) 259.

22. J.-S. Ye, Y. Wen, W.D. Zhang, L.M. Gan, G.Q. Xu, F.-S. Sheu, Electroanalysis 15 (2003) 1693.

23. J.J. Gooding, Electrochim. Acta 50 (2005) 3049.

24. Don N. Futaba, Kenji Hata, Takeo Yamada, Tatsuki Hiraoka, Yuhei Hayamizu, Yozo Kakudate, Osamu Tanaike, Hiroaki Hatori, Motoo Yumura & Sumio Iijima. Nature Materials 5, 987 - 994 (2006)

25. Christenson A, Shleev S, Mano N, Heller A, Gorton L. 2006, Biochim. Biophys. ActaBioenerg. 1757:1634–41

26. Xu F, Shin W, Brown SH, Wahleithner JA, Sundaram UM, Solomon EI. 1996. Biochem. Biophys. Acta1292:303–11

27. Solomon EI, Sundaram UM, Machonkin TE. 1996.Chem. Rev.96:2563–605

28. S. Shleev, J. Tkac, A. Christenson, T. Ruzgas, A. I. Yaropolov, J. W. Whittaker, L. Gorton, Biosens. Bioelectron. 2005, 20, 2517 – 2554.

29. C. F. Blanford, R. S. Heath, F. A. Armstrong, Chem. Commun. 2007,0, 1710 –1712.

30. Mariem Bourourou, Kamal Elouarzaki, Noemie Lalaoui, Charles Agnes, Alan Le Goff, Michael Holzinger, Abderrazak Maaref, and Serge Cosnier, Chem. Eur. J. 2013, 19, 9371 – 9375

31. Adrianna Zloczewskaa, Martin Jönsson-Niedziolkaa, Jerzy Rogalskib, MarcinOpalloa, Electrochimica Acta 56 (2011) 3947–3953

32. M. T. Meredith, M. Minson, D. Hickey, K. Artyushkova, D. T. Glatzhofer, S. D. Minteer, ACS Catal. 2011, 1, 1683 – 1690.

33. K. Stolarczyk, M. Sepelowska, D. Lyp, K. Z. elechowska, J. F. Biernat, J. Rogalski, K. D. Farmer, K. N. Roberts, R. Bilewicz, Bioelectrochemistry, 2012, 87, 154 –163.

General Conclusion

General Conclusion

The ultimate goal of this thesis is to design bio-interfaces using electrogenerated polymers and nanomaterials for the construction of high performance biosensors (electrochemical as well as optical) and bio-fuel cells (biocathode). A detailed study on how to securely immobilize biosensor components on a transducer surface and the use of nanostructures for efficient biosensing is carried out.

Firstly, a new-affinity system based on supramolecular host-guest interaction between β-CD and biotin is successfully studied using NMR and fluorescence microscopy techniques. An association constant of 3 x 10^2 $L.mol^{-1}$ is determined by NMR analyses. Since immobilization of biomolecules using affinity interactions is the most convenient technique, amperometric biosensors based on the newly developed affinity system are further evaluated. Pyrrole- and pyrene- derivatives are electrogenerated on transducer surface for immobilizing biotin or β-CD modified enzymes. The biosensor clearly indicates the improvement in the sensitivity and maximum current density in comparison to the classical biotin-avidin affinity system.

An optical DNA sensor with improved signal performance involving new inclusion complex between biotin and β-CD using SPR was developed. The studies reflect the synergic effect of quantum dots and gold nanoparticles for amplification of SPR signal. Gold nanoparticles acts as an optical antenna for enhancing or quenching the SPR signal depending on the length of DNA as linker between quantum dot and gold nanoparticle. Therefore, nanoparticles modified with biomolecules are successfully employed for optical signal enhancement. Another category, which leads to improvement in sensitivity of biosensor, is the modification of transducers with such nanomaterials. The next part is dedicated to the incorporation and combination of various nanomaterials (carbon nanotubes, nanodiamond, magnetic nanoparticles and graphene) leading to novel biosensor designs.

In this part, a new approach i.e. layer-by-layer deposition of oxidized SWCNTs onto the electrode surface is shown with nanodiamonds as spacer units in between the two layers. Pyrene-NTA is non-covalently attached to nanotubes *via* π-stacking interactions by dip-coating. Again, an 80-fold increase in the current density and sensitivity of glucose sensor is observed on comparing highly porous 3D nanostructures based on SWCNTs-ox and NDs with

the classical biotin–avidin/streptavidin – biotin layer system on only SWCNTs-ox modified electrodes. To target the detection of antibody – antigen with over several nanometers in diameter, 3D layer-by-layer nanostructures based on magnetic attraction between magnetic nanoparticles and iron impurities present in HiPCO® produced SWCNTs are designed and functionalized non-covalently with pyrene derivatives. Optimal pore sizes for the diffusion of not only the biorecoginition element, but also the analyte and a further label are found for 500 nm sized magnetic NPs. With such nanostructures highly sensitive immunosensors are obtained and, a detection limit of 10 $ng.mL^{-1}$ is reached towards antibody, anti-CT.

Another interesting carbon material, graphene as a sensing layer is employed for the SPR sensing of anti-CT. The π-system of graphene and its nanometer order thickness allows enhancement in the sensitivity towards the detection of the analyte. The gold surfaces are optimized with different polymer thickness to optimize signal capture. Pyrene derivatives that are non-covalently attached to the graphene layer provide the most sensitive SPR signal. A detection limit of 4 $ng.mL^{-1}$ towards anti-CT is also observed with electropolymerized pyrrole derivatives.

Lastly, a preliminary study to design a bio-cathode for bio-fuel cell application is carried out. CNT forest electrodes are non-covalently functionalized with pyrene derivative by dip-coating. The anthraquinone moiety attached to pyrene helps in orienting laccase for efficient direct electron transfer between the laccase and the nanotube forest. An improved bioelectrocatalytic reduction of oxygen (0.9 $mA.cm^{-2}$) is thus obtained with increased stability.

The research work in this thesis introduces a novel affinity system for immobilization of bioreceptors, novel signal amplification strategies, and novel nanostructured bio-designs with high reproducibility and long term stability.

Experimental Part

Section IV

Experimental Part

IV.1 Materials

IV.1.1 Organic compounds

Pyrene-β-CD and Pyrene-NTA were synthesized as follows:

(a) Pyrene-β-CD

240 mg of pyrenebutanoic acid succinester (0.2 mmol) is dissolved in 20 ml dry DMF. 250 mg β-cyclodextrin monoamine (0.2 mmol) was added and the mixture was stirred for 76h at room temperature under argon. Acetone of analytical grade was used for rinsing the precipitate obtained. 108 mg of pyrene-β-CD was obtained as slight yellow solid.

^{1}H-NMR (DMSO, 300 MHz): δ (ppm) = 7.5(6H,m), 7.1(4H,m), 5.8, 4.8, 4.5(22H,m), 3.6 (49H,d)

UV/Vis (NMP): λ_{max} (nm) = 256, 266, 275.6, 314.7, 327.35, 342.3

(b) Pyrene-NTA

To a solution of pyrene butyric acid succinimid ester (400 mg, 1 mmol) in 50 mL of dry DMF, N_α',N_α-bis(carboxymethyl)-L-lysine (350 mg, 1.25 mmol) was added. To dissolve the NTA, NaOH (50 mg, one pellet) solubilised in 2 mL of water was added and one drop of triethylamine was also added to assure the basic environment in the organic phase. The mixture was stirred for 3 days at 60 °C. After removal of the volatiles, the residue was dissolved in water and the product (pyrene-NTA) was precipitated after titration with HCl (1 mol.L^{-1}). 450 mg of pyrene-NTA was obtained as slight yellow solid

^{1}H NMR (CD_3OD, 300 MHz): δ(ppm) = 8.38 (1H, d), 8.17 (1H, dd), 8.15 (1H, d), 8.11 (2H, 2d), 8.02 (2H, 2d), 8.00 (1H, d), 7.93 (1H,d), 3.87 (2H, t), 3.63 (4H, q), 3.45 (1H, t), 3.39 (2H, t), 3.17 (2H, t), 2.17 (2H, t), 1.95-1.23 (6H, m).

MS (EI, 200 °C): m/z = 531.2 ($[M+H]^+$, $C_{30}H_{32}N_2O_7$).

UV/Vis (THF): λ_{max} (nm) = 243, 255.5, 266, 276.5, 313.5, 327.5, 343.5.

Pyrrole biotin, Pyrene-biotin, Pyrrole-NTA, Pyrene-$(AQ)_2$ were available in the laboratory.

IV.1.2 Biomolecules

(a) Enzymes

Glucose oxidase (GOX, EC 1.1.3.4.) from *Aspergillus niger*, polyphenol oxidase(PPO, EC 1.4.18.1.) from *Mushroom*, avidin (EC 215.783.6) from *Hen egg white*, streptavidin, laccase from *Trametes versicolor* and biotin (EC 200.399.3) were obtained from Sigma-Aldrich. Streptavidin-R-PhycoErythrin (Streptavidin-RPE) was purchased from Interchim. Streptavidin Qdot 800 was purchased from Invitrogen.

Biotin tagged GOx, β-CD tagged GOx, PPO tagged biotin and β-CD functionalized gold nanoparticles were available in the laboratory.

Synthesis of β-CD-GOX

Mono-6-deoxy-6-amino-β-cyclodextrin (14.91 mg, 13.1×10^{-6} mol) and 1-ethyl-3-(3-dimethylamino-propyl)carbodiimid hydrochloride (EDC, 5.13 mg, 26.8 10^{-6} mol) were dispersed in phosphate buffer (0.1 $mol.L^{-1}$; pH = 6) using an ultrasound bath. To this solution, glucose oxidase (5.145 mg, 32.2×10^{-9} mol) was added. The reaction mixture was vigorously stirred for 24 h at 4 °C.

β-CD-GOX was purified by centrifugation using a 30000 MWCO concentrator with PES membrane at 6000 G maintained at 4 °C.

The obtained β-CD-GOX in phosphate buffer (0.1 $mol.L^{-1}$; pH = 7) solution was quantified using UV spectroscopy. After ten-times dilution of the solution obtained after purification, the 280 nm-band intensity of the solution was 0.306 corresponding to a concentration of β-CD GOX of 1.83 $mg.mL^{-1}$ (yield: 36 %). Stock solutions of β-CD-GOX (0.5 $mg.mL^{-1}$) were prepared with phosphate buffer (0.1 $mol.L^{-1}$; pH = 7) and stored at -20 °C as aliquots (25 µL) until needed.

Synthesis of B-GOX

Glucose oxidase (5.307 mg, 33.2×10^{-9} mol) was biotinylated with sulfo-NHS-LC- biotin (67 µL of 10^{-2} $mol.L^{-1}$ solution, 675.4×10^{-9} mol) in 5 mL phosphate buffer (0.1 $mol.L^{-1}$; pH = 6) during 2 h at 4 °C.

B-GOX was purified by centrifugation using a 30000 MWCO concentrator with PES membrane at 6000 G maintained at 4 °C.

The obtained B-GOX in phosphate buffer solution was quantified using UV spectroscopy. After ten-times dilution of the solution obtained after purification, the 280 nm-band intensity of the solution was 0.359 corresponding to a concentration of B-GOX of 2.15 $mg.mL^{-1}$ (yield: 41 %). Stock solutions of B-GOX (0.5 $mg.mL^{-1}$) were prepared with phosphate buffer (0.1 $mol.L^{-1}$; pH = 7) and stored at -20 °C as aliquots (25 µL) until needed.

Synthesis of B-PPO

Polyphenol oxidase (5.0 mg, 39.1×10^{-9} mol) was biotinylated with sulfo-NHS-LC- biotin (78 µL of 10^{-2} $mol.L^{-1}$ solution, 780×10^{-9} mol) in 5 mL phosphate buffer (0.1 $mol.L^{-1}$; pH = 6) during 2 h at 4 °C.

B-PPO was purified by centrifugation using a 30000 MWCO concentrator with PES membrane at 6000 G maintained at 4 °C.

The obtained B-PPO in phosphate buffer solution was quantified using UV spectroscopy. After three-times dilution of the solution obtained after purification, the 280 nm-band intensity of the solution was 0.374 corresponding to a concentration of B-PPO of 0.723 $mg.mL^{-1}$ (yield: 51 %). Stock solutions of B-PPO (0.3 $mg.mL^{-1}$) were prepared with phosphate buffer (0.1 $mol.L^{-1}$; pH = 7) and stored at -20 °C as aliquots (25 µL) until needed.

(b) DNA

The DNA sequences are the following: Capture probe with 10T spacer: 5' Biotin TTTTTTTTTT CA GGT CGC CCC TTC GCC GCC 3'. Complementary ssDNA: 5' Biotin GGC GGC GAA GGG GCG ACC TG- 3'

(c) Antibody-Antigen

Cholera toxin B subunit-biotin labeled (lyophilized powder, biotin content 1.2 $mol.mol^{-1}$ protein), peroxidase labeled IgG anti-rabbit antibody (from goat, protein content 0.8 $mg.mL^{-1}$, affinity isolated antibody), anti-cholera toxin (from rabbit, protein content 48 $mg.mL^{-1}$, purified toxin from *Vibriocholerae*), biotin monoclonal anti-rabbit IgG -γ –chain specific (from

mouse, protein content 4.2 mg.mL^{-1}), polyoxyethylene-sorbitanmonolaurate (Tween® 20), and bovine serum albumin (BSA) were purchased from Sigma.

IV.1.3 Nanomaterials

HiPCO® Single walled carbon nanotubes (purified, < 15 wt.% Fe impurities) were purchased from Unidym, Sunnyvale, CA and multi walled carbon nanotubes (95 + % C purity) from Nanocyl. Magnetic nanoparticles (Standard Carboxyl-Adembeads 0211 (100 nm) and master beads Carboxylic Acid 0215 (500 nm)) from Ademtech. Magnetic microparticles (Dynabeads M-270 carboxylic acid (2.4 µm)) were purchased from Invitrogen and carboxylated latex nanoparticles (100 nm) from Sigma.

IV.1.4 Reagents

TBAP (tetra-n-butyl ammonium perchlorate), acetonitrile, mono-, and dibasic phosphates were purchased from Sigma-Aldrich. Glucose, hydroquinone (1,4-dihydroxy-benzene), hydrogen peroxide solution (30 wt. % in H_2O), monobasic and dibasic phosphates (K_2HPO_4, KH_2PO_4), PBS tablets (pH 7.4, 10 mmol.L^{-1}) and 1-Methyl-2-pyrrolidone (NMP) were purchased from Sigma. $CuCl_2$ and $AgNO_3$ were purchased from Prolabo. Lithium perchlorate ($LiClO_4$) was obtained from Fluka. SSPE buffer (20x buffer is 3.0 mmol.L^{-1} NaCl, 0.2 mmol.L^{-1} NaH_2PO_4, and 0.02 mmol.L^{-1} EDTA at pH 7.4) was purchased from Invitrogen (Carlsbad, CA, U.S.A.).

All chemicals were obtained commercially and used as received unless it is mentioned. Stock solutions of glucose were allowed to mutarotate at room temperature for 24 h before use, and were kept refrigerated.

IV.2 Apparatus

IV.2.1 Electrochemical measurements

All electrochemical measurements (cyclic voltammetry and electropolymerization) were carried out in a conventional three-electrode cell with an Autolab potentiostat 100 (Eco Chemie, Utrecht, The Netherlands) using GPES software. An Ag/Ag^+ ($AgNO_3$ (10 mmol.L^{-1}) in CH_3CN + 0.1 mol.L^{-1} $LiClO_4$) and SCE or Ag/AgCl electrodes were used as a reference electrode

in acetonitrile electrolyte and aqueous solutions, respectively and a Pt wire, placed in separate compartment containing organic electrolyte served as counter electrode. The working electrodes were platinum or glassy carbon disks (2-5 mm diameter) and polished with 2 µm diamond paste (MECAPREX Press PM) before its modification.

Electrochemical measurements for CNT forest in **Chapter-8** were performed in a plate material evaluating Teflon cell with a conventional three-electrode configuration.

The amperometric measurements were performed with a Tacussel PRG-DL potentiostat (Tacussel, France) connected to a computer with E-recorder interface and controlled by the Echart software (eDAQ, Australia).

Electropolymerizations in **Chapter-4** were performed, in a conventional three-electrode cell, containing 0.1 $mol.L^{-1}$ $LiClO_4$ in acetonitrile as electrolyte solution with EZstat PRO 100 (NuVant Systems, Inc. Crown Point, Indiana) using EZware software. An Ag/Ag^+ ($AgNO_3$ (10 $mmol.L^{-1}$) in CH_3CN) electrode was used as a reference electrode and a Pt wire, placed in separate compartment containing organic electrolyte served as counter electrode.

IV.2.2 SPR measurements

SPRi detection of biomolecular binding interactions was performed using the SPRi Lab þapparatus equipped with an 800 nm LED source, CCD camera, and a flow cell (GenOptics, France), placed in a Memmert Peltier-cooled incubator (Rose Scientific, Canada) for temperature control.

SPR measurments in **Chpater-7** were performed with Springle, Autolab SPR systems.

Gold slides

Gold slides for SPRi were provided by Amir Foudeh of Prof. Tabrizian's group in Canada. The Gold-coated slides were cleaned with UV/ozone for 20 min, rinsed thoroughly with MQ water, and treated with piranha solution for another 5 min. After rinsing with MQ water, the slides were dried under a stream of nitrogen.

For Autolab springle SPR, NSF 15 gold disks were purchased from KE instrument BV, Netherlands and used as received.

IV.2.3 Microscopy measurements

Fluorescence microscopy images were recorded with an OLYMPUS BX61 microscope where Au-microelectrode array wafers provided by the Biosensors and Biocatalysis Group of the University of Leeds (U.K.) were used for the experiments.

FEG-SEM images were recorded using ULTRA 55 FESEM based on the GEMENI FESEM column with beam booster (Nanotechnology Systems Division, Carl Zeiss NTS GmbH, Germany) and tungsten gun.

The surface profile of graphene-modified gold was studied using Keyence VK-X200K scanning laser microscope.

IV.2.4 Spectroscopy measurements

ESI mass spectra were recorded with a Bruker APEX-Qe ESI FT-ICR mass spectrometer.

^{1}H NMR spectra were recorded at 300 MHz. All shifts for ^{1}H spectra were referenced to the residual solvent peak and are reported in ppm. The ^{1}H NMR spectra were recorded with D2O solutions of β-CD, biotin, and its mixtures of 1:0.2, 1:0.4, 1:0.6, 1:0.8, 1:1, and 1:1.2 ratio, respectively. Proton–proton NOE spectra were recorded at 500 MHz.

FTIR spectra were recorded using a Nicolet 'Magna 550' spectrometer using ATR (Attenuated Total Reflexion).

Raman spectra were recorded using a Dilor XY spectrometers equipped with a multichannel CCD detector. An Ar^{+} laser was used for excitation at 514.5 nm.

List of abbreviations

A: Adenine

Ag /Ag$^+$: Reference electrode in an organic solution solution [Ag^+] = [NO_3^-] = 10 mmol.L^{-1} .

Ag/AgCl: Reference electrode in an aqueous solution

Anti-CT: Anti-Cholera toxin

ATR: Attenuated Total Reflexion

Au: Gold

AuNPs: Gold nanoparticles

a.u : Arbitrary unit

β –CD: β-cyclodextrin

C: Cytosine

CH_3CN: Acetonitrile

CD_3OD: Deuterated methanol

CNTs: Carbon nanotubes

D_2O: Deuterium oxide

DMF: Dimethylformamide

DMSO: Dimethyl sulfoxide

DNA: Deoxyribonucleic acid

ssDNA: Single-stranded deoxyribonucleic acid

dsDNA: Double-stranded deoxyribonucleic acid

EC: Enzyme commission number

ELISA: Enzyme-linked immunosorbent assay

ESI MS: Electrospray ionisation mass spectroscopy

F: Faraday constant (1 Faraday = 96 485.3415 C)

FAD: Flavin adenine dinucleotide

FE-SEM: Field emission scanning electron microscope

FTIR: Fourier transform infrared

G: Guanine

GOx: Glucose oxidase

GOx-B: Biotin modified glucose oxidase

GOx-CD: β-cyclodextrin modified glucose oxidase

HPLC: High-performance liquid chromatography

HRP: Horseradish peroxidase

IgG: Immunoglobulin G

J_{max}: Maximum current density (saturation current)

K_a: Association constant

K_M: Michaelis-Menten constant

K_M^{app}: Apparent Michaelis-Menten constant

kDa: kiloDalton

Lac: Laccase

$LiClO_4$: Lithium perchlorate.

Mg^{2+}/Ni^{2+}/Cu^{2+}: Magnesium/Nickel/Copper cations

MWCNT: Multi-walled carbon naotubes

NMP: N-Methyl-2-pyrrolidone

NMR: Nuclear magnetic resonance

NOE: Nuclear Overhauser effect

NTA: Nitrilotriacetic acid

PBS: Phosphate buffer saline

pH: Power of hydrogen

PMMA: Poly(methyl methacrylate)

PPO: Polyphenol oxidase

PPO-B: Biotin modified polyphenol oxidase

Pt: Platinum

Q: Charge.

SCE: Saturated calomel electrode (reference electrode in aqueous solution)

SiO_2: Silicon dioxide or silica

SPR: Surface plasmon resonance

SPRi: Surface plasmon resonance imaging

SWCNT: Single-walled carbon nanotube

T: Thymine

Ta: Tanatalum

TBAP: Tetrabutylammonium perchlorate.

v **:** Scan rate

λ **:** Wavelength

Ø : Diameter

IUPAC names for organic compounds

Pyrene-$(AQ)_2$: 1-[bis (2anthraquinonyl)- aminomethyl] pyrene

Pyrrole biotin: biotin-11-pyrrol-1-yl-undecyl ester

Pyrene biotin: 4-pyren-1-yl butyl 5-(2-oxo-1,3,3a,4,6,6a-hexahydrothieno[3,4-d]imidazol-4-yl) pentanoate.

Pyrene β –CD: mono-6-(2-pyrenebutylamino)-6-deoxy-β-cyclodextrin

Pyrrole-NTA: 2-[bis(carboxymethyl)amino]-5-(11-pyrrol-1-ylundecanoylamino)pentanoic acid.

Pyrene-NTA: 2-[bis(carboxymethyl)amino]-6-(4-pyren-1-ylbutanoylamino)hexanoic acid.

Publications and Presentations

Publications:

1. Meenakshi Singh, Michael Holzinger, Maryam Tabrizian, Sinéad Winters, Serge Cosnier and Georg S. Duesberg. Monolayer graphene as an efficient double-faced scotch tape for sensitivity enhancement of surface plasmon resonance immunosensors. (Submitted)

2. Meenakshi Singh, Michael Holzinger, Maryam Tabrizian and Serge Cosnier. Layer-by-layer scaffold formation using magnetic attraction between HiPCO® single-walled carbon nanotubes and magnetic nanoparticles: application for high performance immunosensors. Carbon (2015), pp 731-738.

3. Meenakshi Singh, Michael Holzinger, Maryam Tabrizian and Serge Cosnier (2014). Nanotubes and nanoparticles based 3D scaffolds for the construction of high performance Biosensors. MRS Proceedings, 1700.

4. Singh, Meenakshi, *et al.* "3D-nanostructured scaffold electrodes based on single-walled carbon nanotubes and nanodiamonds for high performance biosensors." Carbon 61 (2013): 349-356.

5. Holzinger, Michael, Meenakshi Singh, and Serge Cosnier. "Biotin– β-Cyclodextrin: A New Host–Guest System for the Immobilization of Biomolecules." Langmuir 28.34 (2012): 12569-12574.

Presentations:

1. M. Singh, M.Holzinger, M. Tabrizian, S. Cosnier, " Design of bio-interface with enhanced sensitivity and specificity for Lab-on-a-chip devices", Journée Printemps SCF Rhone-Alpes, June 13, 2013, Grenoble, France. (Poster Presentation)

2. M. Singh, M.Holzinger, M. Tabrizian, S. Cosnier, " Design of bio-interface with enhanced sensitivity and specificity for Lab-on-a-chip devices", Journées DCP de Grenoble- du coté Nano, August 28-30, 2013, Autrans, France. (Poster Presentation)

3. M. Singh, M.Holzinger, M. Tabrizian, S. Cosnier, " 3D - Nanostructuring of electrodes using different nanotubes scaffolds for the application in biosensors and bio-fuel cells", ChemOnTubes, March 30 - April 3, 2014, Riva del Garda, Italy. (Oral Presentation)

4. M. Singh, M.Holzinger, M. Tabrizian, S. Cosnier, " 3D - Nanostructuring of electrodes using different nanotubes scaffolds for the application in biosensors and bio-fuel cells", MRS Spring Meeting and Exhibit, April 21-25, 2014, San Francisco, USA. (Poster Presentation)